

University of Nebraska - Lincoln

DigitalCommons@University of Nebraska - Lincoln

---

Mechanical (and Materials) Engineering --  
Dissertations, Theses, and Student Research

Mechanical & Materials Engineering, Department  
of

---

8-2017

# Electrical Characterization of Irradiated Semiconducting Amorphous Hydrogenated Boron Carbide

George Glen Peterson

University of Nebraska-Lincoln, gpeterson5@unl.edu

Follow this and additional works at: <http://digitalcommons.unl.edu/mechengdiss>



Part of the [Electronic Devices and Semiconductor Manufacturing Commons](#), [Engineering Physics Commons](#), [Nuclear Engineering Commons](#), and the [Semiconductor and Optical Materials Commons](#)

---

Peterson, George Glen, "Electrical Characterization of Irradiated Semiconducting Amorphous Hydrogenated Boron Carbide" (2017). *Mechanical (and Materials) Engineering -- Dissertations, Theses, and Student Research*. 124.  
<http://digitalcommons.unl.edu/mechengdiss/124>

This Article is brought to you for free and open access by the Mechanical & Materials Engineering, Department of at DigitalCommons@University of Nebraska - Lincoln. It has been accepted for inclusion in Mechanical (and Materials) Engineering -- Dissertations, Theses, and Student Research by an authorized administrator of DigitalCommons@University of Nebraska - Lincoln.

Electrical Characterization of Irradiated Semiconducting Amorphous  
Hydrogenated Boron Carbide

By

George Glenn Peterson

A DISSERTATION

Presented to the Faculty of

The Graduate College at the University of Nebraska

In Partial Fulfillment of Requirements

For the Degree of Doctor of Philosophy

Major: Engineering

(Materials Engineering)

Under the Supervision of Professor Michael Nastasi

Lincoln, Nebraska

August, 2017

Electrical Characterization of Irradiated Semiconducting Amorphous Hydrogenated  
Boron Carbide

George Glenn Peterson, Ph.D.

University of Nebraska, 2017

Adviser: Michael Nastasi

Semiconducting amorphous partially dehydrogenated boron carbide has been explored as a neutron voltaic for operation in radiation harsh environments, such as on deep space satellites/probes. A neutron voltaic device could also be used as a solid state neutron radiation detector to provide immediate alerts for radiation workers/students, as opposed to the passive dosimetry badges utilized today. Understanding how the irradiation environment effects the electrical properties of semiconducting amorphous partially dehydrogenated boron carbide is important to predicting the stability of these devices in operation. p-n heterojunction diodes were formed from the synthesis of semiconducting amorphous partially dehydrogenated boron carbide on silicon substrates through the use of plasma enhanced chemical vapor deposition (PECVD). Many forms of structural and electrical measurements and analysis have been performed on the p-n heterojunction devices as a function of both He<sup>+</sup> ion and neutron irradiation including: transmission electron microscopy (TEM), selected area electron diffraction (SAED), current *versus* voltage  $I(V)$ , capacitance *versus* voltage  $C(V)$ , conductance *versus* frequency  $G(f)$ , and charge carrier lifetime ( $\tau$ ). In stark contrast to nearly all other electronic devices, the electrical performance of these p-n heterojunction diodes *improved* with irradiation. This is most likely the result of bond defect passivation and resolution of degraded icosahedral based carborane structures (icosahedral molecules missing a B, C, or H atom(s)).

I would like to dedicate this work to Angela, Virginia Rose, Alexia, Caden, and Braelen, all of whom made many sacrifices (big and small) to support me in this adventure and exploration of knowledge.

## Acknowledgements

I have been incredibly fortunate to have Professor Michael Nastasi as my Ph.D. advisor. His knowledge, guidance, and patience have been instrumental in my development as a researcher. His ability to tease out the important aspects of multiple measurements or analyses and tie them together sets a wonderful standard for me to aspire to as I move forward. When something off topic began to catch my interest, he has a wonderful way of re-directing me where I need to go.

I would like to thank Peter Dowben for his guidance through both my undergraduate and graduate education. Attempting to sum up the extent of the impact Peter has had on my academic life and experience in a few sentences is utterly insufficient. And so, I will instead simply say thank you.

I would like to thank Charles Rice, Alyssa Mock, Tino Hofmann, Rafal Korlacki, Derek Sekora, and Chad Briley of Professor Mathias Schubert's group. Our discussions were always helpful for me. And their support in learning about ellipsometry was a powerful tool in my work. I would like to thank Elena Echeverria for our many discussions and collaborative efforts in this field, and her instruction in helping me begin to learn the art that is XPS.

I would like to thank my committee members: Professors Michael Nastasi, Jeffrey Shield, Jinsong Huang, and Hui Li for their support, time, and valuable knowledge and input regarding my research.

I would like to acknowledge S. Ducharme of the Department of Physics and Astronomy at the University of Nebraska – Lincoln for allowing the use of his laboratory's impedance analyzer. I would like to acknowledge S. Adenwalla of the Department of Physics and Astronomy at the University of Nebraska – Lincoln for

allowing the use of her laboratory's neutron generator which is in part funded by the Office of Research and Economic Development (ORED).

The research in this dissertation was supported by the Office of Research and Economic Development at the University of Nebraska-Lincoln, the Defense Threat Reduction Agency (Grant No. HDTRA1-14-1-0041), the National Aeronautics and Space Administration through Grant No. 13-EPSCoR-0012, and the Office of Naval Research (Contracts #FA4600-12-D-9000-0045 and #FA4600-12-D-9000-00567). The research in this dissertation was performed in part in the Nebraska Nanoscale Facility: National Nanotechnology Coordinated Infrastructure and the Nebraska Center for Materials and Nanoscience, which are supported by the National Science Foundation under Award ECCS: 1542182, and the Nebraska Research Initiative. In part in the Center for Nano-hybrid Functional Materials (NSFEPS-1004094), supported in part by funds from the National Science Foundation (CAREER to AKP, CBET-1254415). In part at the Center for Integrated Nanotechnologies, an Office of Science User Facility operated for the U.S. Department of Energy (DOE) Office of Science. Los Alamos National Laboratory, an affirmative action equal opportunity employer, is operated by Los Alamos National Security, LLC, for the National Nuclear Security Administration of the U.S. Department of Energy under contract DE-AC52-06NA25396.

## Acronyms/Abbreviations

$a\text{-B}_{10}\text{C}_{2+x}\text{H}_y$	Semiconducting amorphous partially dehydrogenated boron carbide film
a-C	Amorphous carbon
a-Si	Amorphous silicon
a-Si:H	Hydrogenated amorphous silicon
A	Area of the metal contact
AFM	Atomic force microscopy
BJT	Bipolar heterojunction transistor
BNCT	Boron neutron capture therapy
$C$	Capacitance
C1	First Parallel capacitance component: interpreted as $a\text{-B}_{10}\text{C}_{2+x}\text{H}_y$ dielectric film
C2	Second Parallel capacitance component: interpreted as depletion region between irradiated Si/virgin Si interface
CINT	Center for Integrated Nanotechnologies
$C_D$	Diffusion capacitance
$C_{eq}$	Equivalent capacitance
$C_J$	Junction capacitance
CNT	Carbon nano-tubes
$C_p$	Equivalent parallel circuit capacitance
c-Si	Crystalline silicon
$C(V)$	Capacitance measured as a function of applied voltage
CVD	Chemical vapor deposition
$D$	Dissipation factor
$d$	Interplanar distance
d.c.	Direct current
DLC	Diamond like carbon
$D_N$	Electron diffusion coefficient
$D_P$	Hole diffusion coefficient

DPA	Displacements per atom
$E_C$	Conduction energy level
$\Delta E_C$	Conduction band discontinuity
$E_F$	Fermi energy level – at thermodynamic equilibrium this energy level would have a 50 % probability of being occupied by an electron at any given time
$E_g$	Energy band gap – $E_V - E_C$
$E_i$	Intrinsic energy level
ERD	Elastic recoil detection
$E_T$	Trap energy level
$E_V$	Valence energy level
$\Delta E_V$	Valence band discontinuity
$F$	Structure factor
$f$	Small signal perturbation frequency
FTIR	Fourier transform infrared
$G$	Conductance
$G$	Diffusion conductance
$G_m$	Measured conductance
$G_0$	Low frequency differential diode conductance
HOMO	Highest occupied molecular orbital
HRTEM	High resolution transmission electron microscopy
$I$	Intensity of a diffracted x-ray beam
$I_{Diff}$	Diffusion current
$I_0$	Dark current, or saturation current
$I_{R-G}$	Current due to charge recombination or charge generation
$I(V)$	Current measured as a function of applied voltage
$j$	Imaginary number – $\sqrt{-1}$
$J_v$	Reverse bias leakage current density
$L$	Film length
LANL	Los Alamos National Laboratory
$L_N$	Electron diffusion length

$L_p$	Hole diffusion length
LUMO	Lowest unoccupied molecular orbital
$m$	Profile parameter in a graded p-n junction
$m_{neutron}$	Mass of a neutron
MS	Metal semiconductor interface
$m_{Si}$	Mass of a silicon atom
$n$	Integer multiple in the Bragg equation
$n$	Ideality factor in the ideal diode equation
$n^+$	n side of a p-n junction is heavily doped compared to the p side
$N_A$	Doping concentration of acceptors in a p-type film
$N_B$	Carrier concentration ( $N_A$ or $N_D$ ) of the lightly doped side of a p-n homojunction diode
$N_D$	Doping concentration of acceptors in an n-type film
$n_i$	Intrinsic carrier concentration
$N_n$	Neutron fluence
$N_t$	Trap concentration
$N_T$	Number of transmitted neutrons
NVID	Neutron voltaic identification tag
OPV	Organic photovoltaic
$p^+$	p side of a p-n junction is heavily doped compared to the n side
PECVD	Plasma enhanced chemical vapor deposition
$P_y$	Pyridine
$q$	Elementary charge
$R$	Resistance
R1	First Parallel junction resistance: interpreted as a-B <sub>10</sub> C <sub>2+x</sub> H <sub>y</sub> /Si and/or a-B <sub>10</sub> C <sub>2+x</sub> H <sub>y</sub> /Cr interface(s)
R2	Second Parallel junction resistance component: interpreted as silicon p-n homojunction near ion end of range
R3	Series resistance of device including quasi-neutral region of Si substrate, contact resistance of anode & external circuitry
RBS	Rutherford back scattering
RFID	Radio frequency identification tag

$R_S$	Series resistance
SAED	Selected area electron diffraction
SEM	Scanning electron microscopy
SIMS	Secondary ion mass spectroscopy
SRIM	Stopping and range of ions in matter
$t$	Film thickness
$T$	Device temperature
TEM	Transmission electron microscopy
$V_2$	Di-vacancy state
$V_A$	Applied voltage
$V_{bi}$	Built-in voltage
virgin	non-irradiated sample
$V_J$	Junction voltage
$W$	Depletion width
XPS	X-ray photoelectron spectroscopy
XRD	X-ray diffraction
XRR	X-ray reflectivity
$Y$	Complex admittance
$Y_D$	Diffusion admittance
$Z$	Equivalent complex impedance
$Z$	Atomic number
$\epsilon_0$	Permittivity of free space – $8.854 \times 10^{-12}$ F m <sup>-1</sup>
$\epsilon_1$	Dielectric constant of semiconductor 1
$\epsilon_2$	Dielectric constant of semiconductor 2
$\theta$	Scattering angle
$\lambda$	Incident wavelength
$\mu_p$	Hole mobility
$\rho$	Resistivity
$\sigma$	Capture cross section (hole capture as well as neutron capture)
$\tau_n$	Electron lifetime

$\tau_p$	Hole lifetime
$\Phi$	Work function – minimum amount of thermodynamic work needed to remove an electron from a solid to a point in the vacuum just outside of the solid surface
$\chi$	Electron affinity – the change in energy of a neutral atom when an electron is added to the atom to form a negative ion
$\varphi_{b1}$	Built-in potential of Semiconductor 1
$\varphi_{b2}$	Built-in potential of Semiconductor 2
$\varphi_{bi}$	Device built-in potential
$\omega$	Angular frequency ( $\omega = 2\pi f$ )

## Table of Contents

Chapter 1	Introduction .....	1
1.1	References .....	6
Chapter 2	Experimental Details of Film Synthesis, Device Fabrication, and Characterization .....	12
2.1	Plasma Enhanced Chemical Vapor Deposition .....	12
2.2	Metallization .....	15
2.3	Transmission Electron Microscopy (TEM) .....	19
2.4	Secondary Ion Mass Spectroscopy (SIMS) .....	24
2.5	Elastic Recoil Detection (ERD) .....	26
2.6	Current <i>versus</i> Voltage Measurements .....	28
2.7	Capacitance <i>versus</i> Voltage Measurements .....	35
2.8	References .....	39
Chapter 3	Improved p-n Heterojunction Device Performance Induced by Irradiation in Amorphous Boron Carbide Films .....	41
3.1	Introduction .....	41
3.2	Theory and Experiment .....	43
3.3	Results .....	45
3.4	Discussion .....	50
3.5	Conclusions .....	55
3.6	References .....	56
Chapter 4	Charge Carrier Lifetime .....	65
4.1	Introduction .....	65
4.2	Experimental Details .....	66
4.3	Results and Discussion .....	67
A	Heterojunction Capacitance vs Voltage .....	67
B	The Drift Carrier Lifetimes .....	75
4.4	Summary and Conclusions .....	79
4.5	References .....	81
Chapter 5	Conductance <i>versus</i> Frequency Measurements .....	86
5.1	Introduction .....	86
5.2	Experimental Details .....	88
5.3	Results .....	88
5.4	Discussion .....	92
5.5	Conclusions .....	99

5.6	References.....	101
Chapter 6	Improved p-n Heterojunction Performance After Neutron Irradiation ...	105
6.1	Introduction.....	105
6.2	Experimental Details.....	106
6.3	Results.....	107
6.4	Discussion.....	117
6.5	Conclusions.....	124
6.6	References.....	126
Chapter 7	Summary and Conclusions .....	133
7.1	Appendix A.....	136
7.2	Appendix B .....	137
7.3	Appendix C .....	137
7.4	References.....	140

## List of Figures

<b>Fig. 1.1</b> Picture of highly enriched uranium for use in scientific experiments [19].....	2
<b>Fig. 1.2</b> RFID tag available from Shenzhen Chuangxinjia RFID tag corporation .....	2
<b>Fig. 1.3</b> Cartoon illustrating the neutron capture fragmentation process with boron atoms [23] .....	3
<b>Fig. 1.4</b> Measured current pulses through a boron carbide homojunction demonstrating that neutron capture and current pulse generation occurs in the presence of neutrons [5] .....	4
<b>Fig. 1.5</b> Schottky Barrier Diode irradiation to $3.4 \times 10^{-6}$ DPA. Flux of $2.2 \times 10^9$ neutrons per $\text{cm}^2 \text{ s}$ [31] .....	5
<b>Fig. 2.1</b> Schematic of PECVD chamber labeling critical components: left image is the exterior of the chamber, right image is the interior of the chamber .....	13
<b>Fig. 2.2</b> Model of icosahedral closo-carboranes in three molecular configurations: (a) 1,2-Dicarbododecaborane, $\text{B}_{10}\text{C}_2\text{H}_{12}$ , (o-carborane), (b) 1,7-Dicarbododecaborane, $\text{B}_{10}\text{C}_2\text{H}_{12}$ , (m-carborane), (c) 1,12-Dicarbododecaborane, $\text{B}_{10}\text{C}_2\text{H}_{12}$ , (p-carborane)	14
<b>Fig. 2.3</b> Schematic of a d.c. magnetron sputtering process in a sputter down configuration [7] .....	16
<b>Fig. 2.4</b> Energy band diagrams for ideal MS contacts between a metal and an n-type semiconductor: $\Phi_M > \Phi_S$ system (a) an instant after contact formation and (b) under equilibrium conditions; $\Phi_M < \Phi_S$ system (c) an instant after contact formation and (d) under equilibrium conditions .....	17
<b>Fig. 2.5</b> 1 cm $\times$ 1 cm sample showing (a) the top of a sample with 4 circular Au contacts each 1 mm in diameter and (b) the bottom of a sample with 2 rectangular Cr/Au contacts each 4 mm $\times$ 8 mm .....	18
<b>Fig. 2.6</b> Schematic representation of a transmission electron microscope where a) has an aperture that blocks diffracted electrons and transfers transmitted electrons down the microscope (focal plane) and b) has the selected area aperture inserted at the back focal plane, and transfers the diffracted electrons down the microscope [11].....	20
<b>Fig. 2.7</b> (a) Structure of a spinel ( $\text{AB}_2\text{O}_4$ ) unit cell.....	22
<b>Fig. 2.8</b> The experimental SAED pattern, overlaid by the calculated SAED pattern, and experimental XRD pattern of polycrystalline Al in the top right quadrant .....	23
<b>Fig. 2.9</b> Selected Area Electron Diffraction (SAED) pattern obtained from silica superstructures showing amorphous halos [13].....	23
<b>Fig. 2.10</b> Schematic of the SIMS irradiating ion and resulting collision cascade [15]24	
<b>Fig. 2.11</b> SIMS chemical profile of AlN/IDT/AlN/Sapphire heterostructure [17].....	25
<b>Fig. 2.12</b> SIMS depth profile showing elemental atomic percentage as a function of film depth for amorphous semiconducting partially dehydrogenated boron carbide on Si .....	26

<b>Fig. 2.13</b> Experimental geometry for forward recoil spectrometry experiments to determine depth profiles of $^1\text{H}$ and $^2\text{H}$ in solids [18].....	27
<b>Fig. 2.14</b> Ellastic Recoil Detection data of incident 40 MeV Ni ions upon amorphous semiconducting partially dehydrogenated boron carbide on Si.....	28
<b>Fig. 2.15</b> p-n junction diode energy band diagram, carrier distribution, and carrier activity close to the depletion region at equilibrium ( $V_A=0$ ).....	29
<b>Fig. 2.16</b> Linear plot of the measured I-V characteristics derived from a commercially available Si pn junction diode at room temperature .....	31
<b>Fig. 2.17</b> p-n junction diode energy band diagram, carrier distribution, and carrier activity close to the depletion region under forward bias ( $V_A > 0$ ) .....	32
<b>Fig. 2.18</b> p-n junction diode energy band diagram, carrier distribution, and carrier activity close to the depletion region under reverse bias ( $V_A < 0$ ).....	32
<b>Fig. 2.19</b> Capacitance versus Voltage curve (left axis) and $1/C^2$ versus Voltage (right axis) data obtained from a commercial silicon epitaxial planar diode (purchased from Vishay Semiconductors) taken at 100 kHz.....	38
<b>Fig. 3.1</b> The SRIM simulation of energy deposition in a- $\text{B}_{10}\text{C}_{2+x}\text{H}_y$ -Si device separated into its ionization (electronic stopping) and recoil (elastic collisions) components per ion .....	44
<b>Fig. 3.2</b> The current vs voltage curves for boron carbide to silicon heterojunction diodes, following different levels of irradiation. ....	46
<b>Fig. 3.3</b> The ratio of the derivative of forward bias current with respect to voltage by the derivative of reverse bias current with respect to voltage derived from the I(V) data taken between 0.75 and 1.00 applied volts .....	47
<b>Fig. 3.4</b> The HRTEM image of a- $\text{B}_{10}\text{C}_{2+x}\text{H}_y$ film-Si(001) interface after irradiation (0.6 dpa equivalent) and shows that the Si substrate remains crystalline near the interface and the a- $\text{B}_{10}\text{C}_{2+x}\text{H}_y$ film – Si(001) junction interface remains abrupt .....	48
<b>Fig. 3.5</b> The TEM image of an a- $\text{B}_{10}\text{C}_{2+x}\text{H}_y$ to Si heterojunction after irradiation equivalent to 0.6 dpa in the boron carbide film .....	50
<b>Fig. 3.6</b> The reverse bias leakage current (-0.5 volts) versus irradiation level.....	53
<b>Fig. 4.1</b> The current <i>versus</i> voltage curves for PECVD synthesized p-n heterojunction diodes synthesized from ortho-carborane on silicon comparing the undoped (a- $\text{B}_{10}\text{C}_{2+x}\text{H}_y/\text{Si}$ ) device to a pyridine/ortho-carborane composite (3:1 ratio) film (a- $\text{B}_{10}\text{C}_{2+x}\text{H}_y:\text{Py}/\text{Si}$ ) .....	68
<b>Fig. 4.2</b> I(V) curves comparing a- $\text{B}_{10}\text{C}_{2+x}\text{H}_y/\text{Si}$ heterojunction devices based on (a) ortho-carborane (undoped), (b) ortho-carborane (doped with benzene), (c) meta-carborane (undoped), (d) meta-carborane (doped with benzene).....	69

- Fig. 4.3** Low frequency conductance of the PECVD synthesized pyridine/ortho-carborane composite film on silicon device (pyridine doped) and PECVD ortho-carborane film on silicon device (undoped) heterojunctions calculated from the I(V) data of Fig. 4.1 ..... 71
- Fig. 4.4** The capacitance *versus* voltage curves of (a) the ortho-carborane boron carbide films, without pyridine, on silicon ( $B_{10}C_{2+x}H_y/Si$ ) and (b) the co-deposited pyridine and ortho-carborane boron carbide films on silicon,  $B_{10}C_{2+x}H_y:Py/Si$ , as a function of frequency, are compared ..... 73
- Fig. 4.5** C(V) curves comparing a- $B_{10}C_{2+x}H_y/Si$  heterojunction devices as a function of applied perturbation frequency ..... 75
- Fig. 4.6** Model of diffusion capacitance overlaid on C(V) data at 10 kHz: undoped data (**solid black line**) and pyridine doped data (**solid red line**) ..... 76
- Fig. 4.7** Modeled diffusion capacitance ( $C_D$ ) ( $\square$ ) overlaid on C(V) data measured (solid lines) at 10 kHz for (a) ortho-carborane co-deposited with benzene, and (b) meta-carborane co-deposited with benzene ..... 77
- Fig. 5.1** Circuit model used in analysis. R1 and C1 represent the resistance and capacitance of the a- $B_{10}C_{2+x}:H_y$ , R2 and C2 represent the resistance and capacitance of the silicon, and R3 represents series resistance ..... 88
- Fig. 5.2** Logarithmic Conductance vs. Frequency curve of a- $B_{10}C_{2+x}:H_y$  on Si heterojunctions ..... 92
- Fig. 6.1** Cartoon of neutron capture by a  $^{10}B$  isotope resulting in fragmentation into a  $^7Li$  and  $He^+$  ions with kinetic energy resulting in translation away from the capture site (not to scale) ..... 108
- Fig. 6.2** The current versus voltage curves of a boron carbide to silicon heterojunction diode following neutron irradiation times of 0, 10, 20, and 40 hours of exposure .... 112
- Fig. 6.3** (Left axis) The ratio of the derivative of forward bias current with respect to voltage by the derivative of reverse bias current with respect to voltage derived from I(V) data taken between 0.75 and 1.00 applied volts ..... 114
- Fig. 6.4** Capacitance *versus* Voltage C(V) curves taken at 100 kHz of a- $B_{10}C_{2+x}H_y/Si$  p-n heterojunction device after 0, 10, 20, and 40 hours of neutron irradiation ..... 115
- Fig. 6.5** The HRTEM image and SAED pattern of (a) the a- $B_{10}C_{2+x}H_y$  film – Si (001) interface after 40 hours of neutron irradiation and shows that the Si substrate remains crystalline near the interface and the a- $B_{10}C_{2+x}H_y$  film – Si (001) junction interface remains abrupt and the a- $B_{10}C_{2+x}H_y$  film remains amorphous ..... 118
- Fig. 6.6**  $1/C^2$  versus voltage relationship is plotted to allow for the extrapolation of the device built-in potential ( $V_{bi}$ ) and acceptor carrier concentration ( $N_A$ ) ..... 120
- Fig. 6.7** a- $B_{10}C_{2+x}H_y$  film carrier concentration as a function of neutron exposure as calculated by Equation 6-11 and fitted to the data in Fig. 6.6 ..... 122

**Fig. 6.8** The thermal equilibrium energy-band diagram of two semiconductors of opposite type and different energy band gaps ( $E_g$ ), i.e. a p-n heterojunction [44].  $\varphi_{b1}$  and  $\varphi_{b2}$  represent the built-in potential in semiconductor 1 and 2 respectively ..... 123

**Fig. 6.9** The extrapolated device built-in potential of the p-n heterojunction as a function of neutron exposure taken from Fig. 6.6 and shown as black triangles ( $\blacktriangle$ )..... 124

**Fig. 7.1** Plot of the relative dielectric function *versus* wavelength ..... 139

## Chapter 1 Introduction

Currently there are two main foci in the study of boron carbides in the semiconductor industry. The first is as a real time solid-state neutron radiation detector [1–9] that can immediately alert radiation workers to exposure. The second is as a neutron voltaic for current generation [10–13] in radiation harsh environments with a moderate to high flux of neutrons. Both applications operate off of the same concept; that is, creating an electric field and depletion region in a semiconductor through the synthesis of a p-n junction or Schottky barrier. The electric field serves to separate electron hole pairs generated from irradiating neutrons, and the depletion region allows the separated charge carriers to be swept toward contacts with minimal recombination. If electrons reach the cathode or holes reach the anode current is generated.

In addition to the semiconductor industry, within the medical industry, there is a vast amount of research into icosahedral based boron carbides as it relates to Boron Neutron Capture Therapy [14–17] (BNCT) as a form of radio immunotherapy. Although the application is vastly different from that of neutron detection and neutron voltaics, much of the materials characterization (i.e. structural and chemical) has significant overlap. The research of BNCT in the area of materials characterization has been useful in this research project, and cited where applicable.

Currently, in the United States there are 7100 nuclear warheads, 87.6 tonnes Pu (weapons grade), 599 tonnes highly enriched U of various sizes (example shown in Fig. 1.1), and 625 tonnes Pu (most in the form of spent fuel rods) [18]. Tracking this inventory of fissile material is quite challenging. One of the proposed methods for tracking is through the use of radio frequency identification (RFID) tags such as the commercially available tag shown in Fig. 1.2. RFID tags such as the one pictured in

Fig. 1.2 have a memory chip in the center, and are ringed by an antenna. The memory chip stores a text file, and when a hand held chip reader is brought in close proximity to the tag, the hand held reader emits a radio frequency. That radio frequency interacts with the antenna to generate a current, allowing the chip to transmit the stored text to the reader.



*Fig. 1.1: Picture of highly enriched uranium for use in scientific experiments [19].*



*Fig. 1.2: RFID tag available from Shenzhen Chuangxinjia RFID tag corporation.*

By affixing an RFID tag on each specimen, spent fuel rod, and warhead with unique text or identification number, inventorying what belongs where becomes much easier.

There are a couple of issues with this concept. The first is that it is not real-time; i.e., it requires an active reading. If an inventory is taken every quarter, what happens if radioactive material goes missing in the months between readings? What if instead we could use the neutrons that are naturally being emitted from the fissile materials to keep a real-time inventory of the nuclear stockpile that sends a signal immediately when a piece of the inventory is removed from its storage location? This then is no longer an RFID tag, but a neutron voltaic identification (NVID) tag.

How would such a device operate? There are only a handful of elements that interact with neutrons in a meaningful way. Boron (specifically  $^{10}\text{B}$ ) is one of the elements that has a moderate cross section for thermal neutron capture ( $0.305 \pm 0.016$  barns) [20,21].  $^{10}\text{B}$  neutron capture leads to the loss of boron and creation of daughter fragments with significant kinetic energy [2,8,22]. This is described by the equations below, and illustrated in Fig. 1.3:

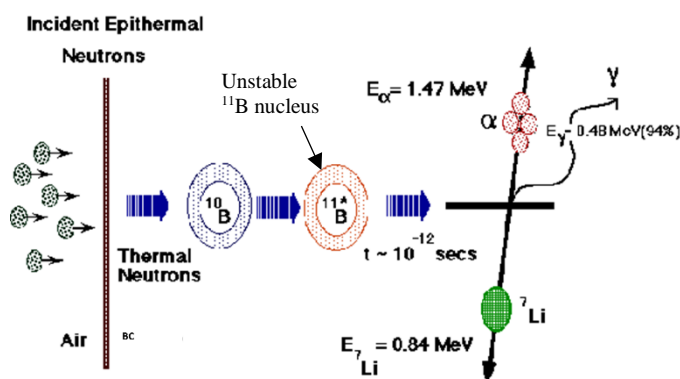
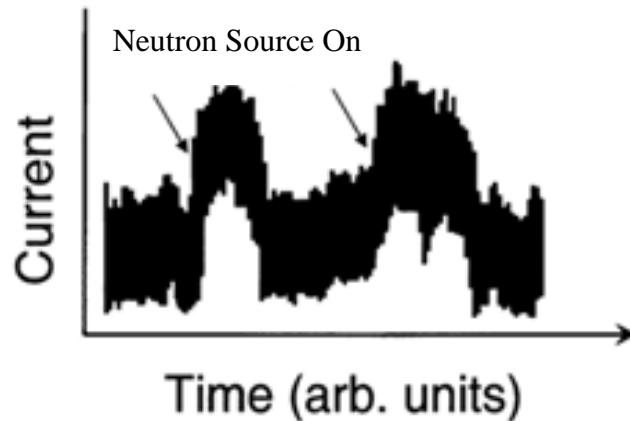


Fig. 1.3: Cartoon illustrating the neutron capture fragmentation process with boron atoms, after [23]

Following the capture/fragmentation process, the  ${}^7\text{Li}$  and  ${}^4\text{He}$  ions deposit energy as they traverse the device in the form of electronic excitation (ionizing energy) or elastic collisions (recoil energy) [24]. This energy deposition creates electron-hole pairs in the ion tracks, and the electric field created across the p-n junction separates the charges, generating a current pulse as Fig. 1.4 demonstrates [5].



*Fig. 1.4: Measured current pulses through a boron carbide homojunction demonstrating that neutron capture and current pulse generation occurs in the presence of neutrons, after [5].*

The polytypes of boron rich icosahedra, such as boron carbide, boron nitride, and boron phosphide are of particular interest because of their apparent ability to heal neutron [25], electron [13,26], and alpha ( $\text{He}^+$ ) [27] radiation. This radiation hard aspect is extremely important for devices expected to function in radiation harsh environments, such as attached to fissile materials, reactor chambers and deep space.

Currently, boron carbide based electrical devices suffer from several limitations. These materials have limits in current rectification efficiency leading to a constant power drain due to high defect concentrations [28] and low carrier mobilities [29]. Although exceptionally high mobilities have been sometimes claimed [30], such claims have not been attributed to plasma-enhanced chemical vapor deposited (PECVD) semiconducting boron carbide.

The purpose of this dissertation is to determine the electrical properties of semiconducting amorphous partially dehydrogenated boron carbide, and further to determine how those electrical properties change with irradiation. The forms of irradiation studied will reflect the forms of radiation to which electrical devices put into service are likely to be subjected: neutron irradiation (primary) and ion irradiation (secondary—resultant from capture/fragmentation process).

Nearly every traditional electrical device suffers degradation in electrical performance under irradiation [31–33]. This is demonstrated in Fig. 1.5 through irradiation of a diamond-Aluminum Schottky Barrier Diode with neutrons at a flux of  $2.2 \times 10^9$  neutrons/cm<sup>2</sup> s [31]. With a very small amount of damage,  $3.4 \times 10^{-6}$  displacements per atom (DPA), the device displays immediate device degradation.

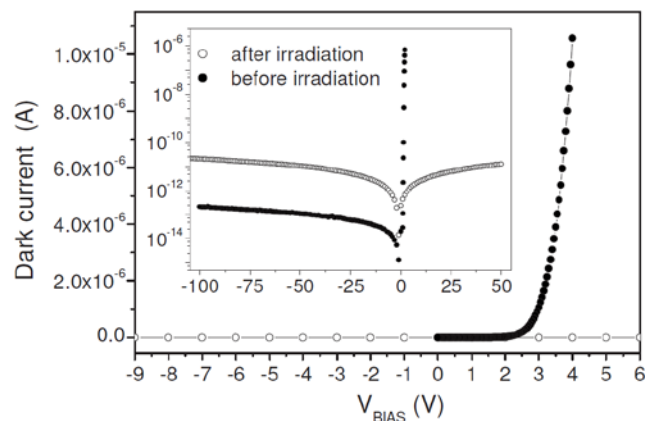


Fig. 1.5: Schottky Barrier Diode irradiation to  $3.4 \times 10^{-6}$  DPA. Flux of  $2.2 \times 10^9$  neutrons per cm<sup>2</sup> s. Reprinted from [31], with the permission of AIP Publishing.

The cause of device degradation in Fig. 1.5 is the transformation of diamond to regions of amorphous carbon (a-C). This causes changes in the band structure, killing rectification properties, and increasing the dark current. The diamond-Al Schottky barrier structure above has been proposed as a radiation based battery [34]. The problem becomes that a device, in addition to having the property of neutron sensitivity, must also be radiation hard.

## 1.1 References

- [1] A.N. Caruso, P.A. Dowben, S. Balkir, N. Schemm, K. Osberg, R.W. Fairchild, O.B. Flores, S. Balaz, A.D. Harken, B.W. Robertson, J.I. Brand, The all boron carbide diode neutron detector: Comparison with theory, *Mater. Sci. Eng. B.* 135 (2006) 129–133. doi:10.1016/j.mseb.2006.08.049.
- [2] A.N. Caruso, The physics of solid-state neutron detector materials and geometries, *J. Phys. Condens. Matter.* 22 (2010) 443201. doi:10.1088/0953-8984/22/44/443201.
- [3] C. Höglund, K. Zeitelhack, P. Kudejova, J. Jensen, G. Greczynski, J. Lu, L. Hultman, J. Birch, R. Hall-Wilton, Stability of  $^{10}\text{B}_4\text{C}$  thin films under neutron radiation, *Radiat. Phys. Chem.* 113 (2015) 14–19. doi:10.1016/j.radphyschem.2015.04.006.
- [4] K. Osberg, N. Schemm, S. Balkir, J.I. Brand, S. Hallbeck, P.A. Dowben, A hand-held neutron detection sensor system, in: Peter Dowben Publ., 2006: p. 4 pp. doi:10.1109/ISCAS.2006.1692801.
- [5] K. Osberg, N. Schemm, S. Balkir, J.I. Brand, M.S. Hallbeck, P.A. Dowben, M.W. Hoffman, A Handheld Neutron-Detection Sensor System Utilizing a New Class of Boron Carbide Diode, *IEEE Sens. J.* 6 (2006) 1531–1538. doi:10.1109/JSEN.2006.883905.
- [6] N. Hong, L. Crow, S. Adenwalla, Time-of-flight neutron detection using PECVD grown boron carbide diode detector, *Nucl. Instrum. Methods Phys. Res. Sect. Accel. Spectrometers Detect. Assoc. Equip.* 708 (2013) 19–23. doi:10.1016/j.nima.2012.12.105.

- [7] N. Hong, *An Exploration of Neutron Detection in Semiconducting Boron Carbide*, University of Nebraska - Lincoln, 2012.  
<http://digitalcommons.unl.edu/physicsdiss/20>.
- [8] N. Hong, J. Mullins, K. Foreman, S. Adenwalla, Boron carbide based solid state neutron detectors: the effects of bias and time constant on detection efficiency, *J. Phys. Appl. Phys.* 43 (2010) 275101. doi:10.1088/0022-3727/43/27/275101.
- [9] E. Echeverría, R. James, U. Chiluwal, F.L. Pasquale, J.A.C. Santana, R. Gapfizi, J.-D. Tae, M.S. Driver, A. Enders, J.A. Kelber, P.A. Dowben, Novel semiconducting boron carbide/pyridine polymers for neutron detection at zero bias, *Appl. Phys. A.* 118 (2014) 113–118. doi:10.1007/s00339-014-8778-4.
- [10] E. Echeverria, B. Dong, G. Peterson, J.P. Silva, E.R. Wilson, M.S. Driver, Y.-S. Jun, G.D. Stucky, S. Knight, T. Hofmann, Z.-K. Han, N. Shao, Y. Gao, W.-N. Mei, M. Nastasi, P.A. Dowben, J.A. Kelber, Semiconducting boron carbides with better charge extraction through the addition of pyridine moieties, *J. Phys. Appl. Phys.* 49 (2016) 355302–355312. doi:10.1088/0022-3727/49/35/355302.
- [11] E. Echeverría, R. James, F.L. Pasquale, J.A. Colón Santana, M.S. Driver, A. Enders, J.A. Kelber, P.A. Dowben, Neutron Detection Signatures at Zero Bias in Novel Semiconducting Boron Carbide/Pyridine Polymers, in: *Symp. DDWW – Mater. Radiat. Eff. Adv. Nucl. Technol.*, 2015. doi:10.1557/opl.2015.352.
- [12] A.N. Caruso, R.B. Billa, S. Balaz, J.I. Brand, P.A. Dowben, The heteroisomeric diode, *J. Phys. Condens. Matter.* 16 (2004) L139–L146. doi:10.1088/0953-8984/16/10/L04.
- [13] D. Emin, Unusual properties of icosahedral boron-rich solids, *J. Solid State Chem.* 179 (2006) 2791–2798. doi:10.1016/j.jssc.2006.01.014.

- [14] K.J. Riley, P.J. Binns, S.J. Ali, O.K. Harling, The design, construction and performance of a variable collimator for epithermal neutron capture therapy beams, *Phys. Med. Biol.* 49 (2004) 2015–2028.
- [15] M.W. Mortensen, O. Björkdahl, P.G. Sørensen, T. Hansen, M.R. Jensen, H.J.G. Gundersen, T. Bjørnholm, Functionalization and cellular uptake of boron carbide nanoparticles. The first step toward T cell-guided boron neutron capture therapy, *Bioconjug. Chem.* 17 (2006) 284–290. doi:10.1021/bc050206v.
- [16] M.W. Mortensen, P.G. Sørensen, O. Björkdahl, M.R. Jensen, H.J.G. Gundersen, T. Bjørnholm, Preparation and characterization of Boron carbide nanoparticles for use as a novel agent in T cell-guided boron neutron capture therapy, *Appl. Radiat. Isot. Data Instrum. Methods Use Agric. Ind. Med.* 64 (2006) 315–324. doi:10.1016/j.apradiso.2005.08.003.
- [17] J. Ghassoun, N. Senhou, The evaluation of neutron and gamma ray dose equivalent distributions in patients and the effectiveness of shield materials for high energy photons radiotherapy facilities, *Appl. Radiat. Isot. Data Instrum. Methods Use Agric. Ind. Med.* 70 (2012) 620–624. doi:10.1016/j.apradiso.2011.12.041.
- [18] International Panel on Fissile Materials: United States, *Int. Panel Fissile Mater.* (n.d.). [http://fissilematerials.org/countries/united\\_states.html](http://fissilematerials.org/countries/united_states.html) (accessed December 7, 2016).
- [19] How fissile material falls through the cracks, *Bull. At. Sci.* (2014). <http://thebulletin.org/how-fissile-material-falls-through-cracks7296> (accessed December 7, 2016).
- [20] R.B. Billa, *Optical Properties of Semiconducting Boron Carbide for Neutron Detection Applications*, University of Nebraska - Lincoln, 2009.

- [21] S. Mughabghab, Atlas of Neutron Resonances: Resonance Parameters and Thermal Cross Sections. Z=1-100, 5th ed., Elsevier Science, 2006.
- [22] G.F. Knoll, Radiation Detection and Measurement, 3rd ed., Wiley, New York, 2000.
- [23] R. Howell, Neutron Capture by Boron, n.d.  
<http://web.mit.edu/nrl/www/bnct/info/description/description.html>.
- [24] M. Nastasi, J.W. Mayer, Ion Implantation and Synthesis of Materials, Springer, 2006.  
<http://www.springer.com/physics/particle+and+nuclear+physics/book/978-3-540-23674-0> (accessed February 5, 2015).
- [25] D. Simeone, C. Mallet, P. Dubuisson, G. Baldinozzi, C. Gervais, J. Maquet, Study of boron carbide evolution under neutron irradiation by Raman spectroscopy, *J. Nucl. Mater.* 277 (2000) 1–10. doi:10.1016/S0022-3115(99)00149-X.
- [26] T. Stoto, N. Housseau, L. Zuppiroli, B. Kryger, Swelling and microcracking of boron carbide subjected to fast neutron irradiations, *J. Appl. Phys.* 68 (1990) 3198–3206. doi:10.1063/1.346370.
- [27] G. Peterson, Q. Su, Y. Wang, P.A. Dowben, M. Nastasi, Improved p–n heterojunction device performance induced by irradiation in amorphous boron carbide films, *Mater. Sci. Eng. B.* 202 (2015) 25–30.  
doi:10.1016/j.mseb.2015.09.002.
- [28] M.M. Abdul-Gader, U.A. Al-Binni, A.A. Ahmad, M.A. Al-Basha, N.J. Ianno, Low-field current transport mechanisms in rf magnetron sputter deposited boron carbide (B<sub>5</sub>C)/p-type crystalline silicon junctions in the dark, *Int. J. Electron.* 88 (2001) 873–901.

- [29] B.J. Nordell, C.L. Keck, T.D. Nguyen, A.N. Caruso, S.S. Purohit, W.A. Lanford, D. Dutta, D. Gidley, P. Henry, S.W. King, M.M. Paquette, Tuning the properties of a complex disordered material: Full factorial investigation of PECVD-grown amorphous hydrogenated boron carbide, *Mater. Chem. Phys.* 173 (2016) 268–284. doi:10.1016/j.matchemphys.2016.02.013.
- [30] H. Werheit, V. Filipov, U. Kuhlmann, U. Schwarz, M. Armbrüster, M. Antadze, Isotopic phonon effects in  $\beta$ -rhombohedral boron—non-statistical isotope distribution, *J. Phys. Condens. Matter.* 24 (2012) 175401. doi:10.1088/0953-8984/24/17/175401.
- [31] S. Almaviva, M. Angelone, M. Marinelli, E. Milani, M. Pillon, G. Prestopino, A. Tucciarone, C. Verona, G. Verona-Rinati, Characterization of damage induced by heavy neutron irradiation on multilayered  $^6\text{LiF}$ -single crystal chemical vapor deposition diamond detectors, *J. Appl. Phys.* 106 (2009) 73501. doi:10.1063/1.3224869.
- [32] M. Caussanel, A. Canals, S.K. Dixit, M.J. Beck, A.D. Touboul, R.D. Schrimpf, D.M. Fleetwood, S.T. Pantelides, Doping-Type Dependence of Damage in Silicon Diodes Exposed to X-Ray, Proton, and  $\text{He}^+$  Irradiations, *IEEE Trans. Nucl. Sci.* 54 (2007) 1925–1930. doi:10.1109/TNS.2007.909021.
- [33] H. Ohyama, K. Hayama, T. Hakata, E. Simoen, C. Claeys, J. Poortmans, M. Caymax, Y. Takami, H. Sunaga, Impact of high energy particle irradiation on the electrical performance of  $\text{Si}_{1-x}\text{Ge}_x$  epitaxial diodes, *J. Mater. Sci. Mater. Electron.* 10 (1999) 335–337.

- [34] T. Scott, “Diamond-age” of power generation as nuclear batteries developed, Univ. Bristol News. (2016).  
<http://www.bristol.ac.uk/news/2016/november/diamond-power.html> (accessed December 14, 2016).

## Chapter 2 Experimental Details of Film Synthesis, Device Fabrication, and Characterization

### 2.1 Plasma Enhanced Chemical Vapor Deposition

Plasma Enhanced Chemical Vapor Deposition (PECVD) is a technique that uses electric fields to assist in film synthesis. The technique is very similar to Chemical Vapor Deposition (CVD) in that a volatile precursor is given enough energy to react, decompose, or condense on a substrate. However, CVD synthesis is typically a high temperature process. The plasma enhancement of the CVD process utilizes the electric field created by a plasma between electrodes to drive the ionized atoms of the plasma gas toward a substrate. The combination of the electric field and the kinetic energy of the ionized gas allow for the precursor material to become reactive or decompose, and allows for film synthesis at lower temperatures. For example, the CVD temperature of boron carbide is 1000 C [1], while the PECVD temperature of boron carbide is between 250 - 450 C [2–4].

The PECVD process for boron carbide synthesis is really a 2-part process: 1) Interaction between the precursor molecule and the ionized plasma gas, and 2) Ion bombardment at the substrate surface. A schematic of the PECVD system is shown below in Fig. 2.1 with major components labeled. To start with, a plasma is established in an Argon environment. The creation of the plasma is accomplished through the use of a 2-inch 13.56 MHz radio frequency (RF), water cooled, sputter gun (with the magnets removed) powered by an Advanced Energy® RFX 600 two-stage power generator using a Fetpower™ modular power amplifier and accompanying ATX 600 matching network. The sputter gun is labeled as the “Driven Electrode” in Fig. 2.1. The substrate rests on the substrate heater, which also serves as

the grounded electrode. While parameters can vary, these experiments utilized a 200 mTorr  $\text{Ar}^+$  environment in a vacuum chamber with a base pressure below  $5 \times 10^{-7}$  Torr.

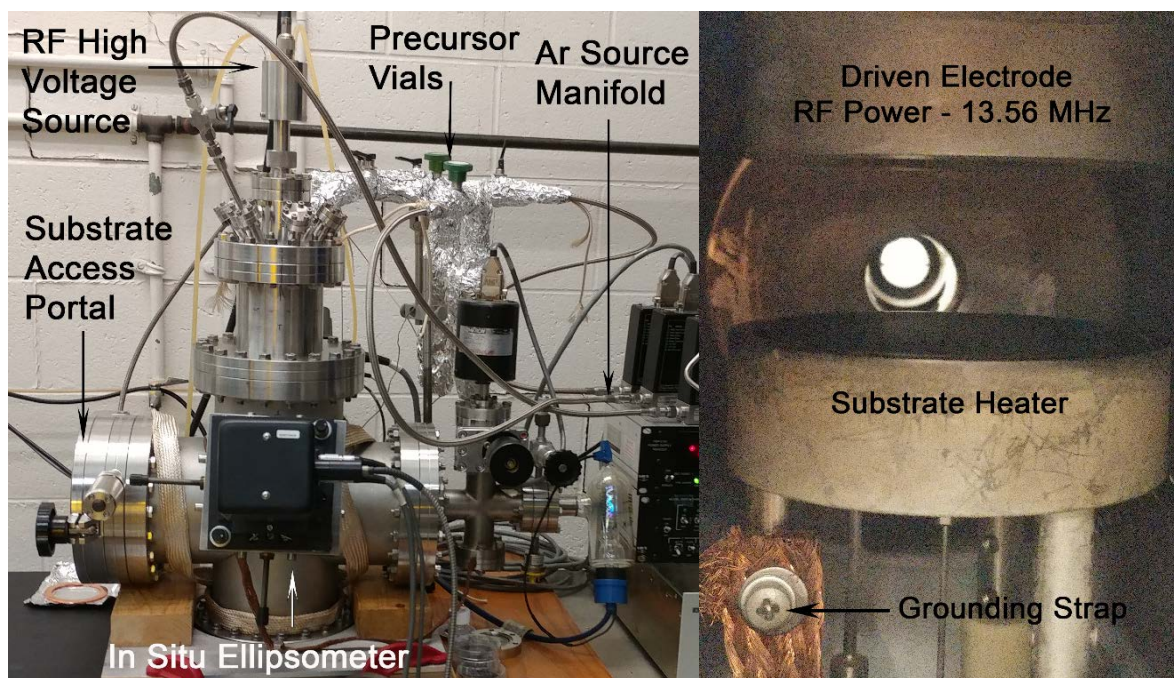


*Fig. 2.1: Schematic of PECVD chamber labeling critical components: left image is the exterior of the chamber, right image is the interior of the chamber.*

Once an  $\text{Ar}^+$  plasma is established, a precursor of 1,2 dicarbadodecaborane, i.e. 1,2- $\text{B}_{10}\text{C}_2\text{H}_{12}$  (o-carborane) is introduced to the plasma. o-carborane is a molecule organized in an icosahedral geometry, shown in Fig. 2.2, along with the other two *closo*-carborane molecular configurations.

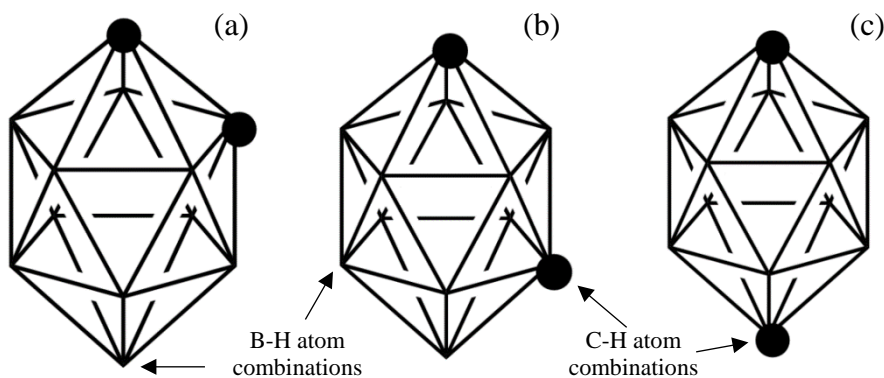


Fig. 2.2: Model of icosahedral closo-carboranes in three molecular configurations: (a) 1,2-Dicarbadoecaborane,  $B_{10}C_2H_{12}$ , (*o*-carborane), (b) 1,7-Dicarbadoecaborane,  $B_{10}C_2H_{12}$ , (*m*-carborane), (c) 1,12-Dicarbadoecaborane,  $B_{10}C_2H_{12}$ , (*p*-carborane). Modeled after images by Sigma-Aldrich. The two dark circles represent C atoms, the other ten intersections are occupied by a B atom. All 12 atoms (C and B) have a bonded H atom normal to the plane.

The first part of film synthesis is the interaction of the molecule with the ionized  $Ar^+$  atoms. The molecules are fractured by collisions with the  $Ar^+$  atoms creating a “soup” of intact molecules, degraded molecules (o-carborane molecules missing a B, C, or H atom), and molecules in an anion or di-anion state. This soup of molecular states, being formed inside of the electric field between the two electrodes of the plasma, accelerates the ions toward the grounding electrode, where the substrate is located. The second part of film synthesis is the  $Ar^+$  ion bombardment once the o-carborane molecular soup has deposited on the substrate. The electric field accelerates the  $Ar^+$  ion toward the grounding electrode, and causes bombardment which acts like an atomic shot peen hammer forcing the molecules closer together, as well as causing large amounts of energy deposition resulting in extremely localized increases in temperature, resulting in film synthesis.

For the scope of this research, device fabrication begins with an n-type (P doped) silicon substrate. During the research process, the substrate resistivity was changed from 1-10  $\Omega \times \text{cm}$  to 65-120  $\Omega \times \text{cm}$ . The purpose of the change was to shorten the depletion width within the a- $B_{10}C_{2+x}H_y$  film. Substrate preparation consisted of successive 5 minute sonication baths in acetone, methanol, and, de-ionized, filtered

water. This is followed by a 5 wt% hydrofluoric acid (HF) bath to remove the native oxide layer and provide hydrogen termination [5]. A 30 minute  $\text{Ar}^+$  plasma etch was performed prior to film deposition according to the procedures outlined by Hong [2] for film synthesis with annealing of  $\text{a-B}_{10}\text{C}_{2+x}\text{H}_y$ . This study employed the deposition parameters outlined by Hong, but did not post-anneal. The purpose of the  $\text{Ar}^+$  plasma etch is to remove any advantageous carbon or water from the Si substrate.

The  $\text{a-B}_{10}\text{C}_{2+x}\text{H}_y$  films are then grown via PECVD by introducing the source molecule (o-carborane) to the established plasma used for the  $\text{Ar}^+$  plasma etch. The growth environment was 200 mTorr  $\text{Ar}^+$ , with a substrate temperature of 350 °C, and a power density of  $6.479 \times 10^{-3} \text{ W/cm}^2$ . Boron carbide films grown under these conditions were determined to be amorphous by high-resolution transmission electron microscopy (HRTEM) and electron diffraction [6] (shown in chapter 3).

## 2.2 Metallization

In order to perform electrical characterization, metal electrodes must be deposited as part of device creation. Over the course of this work, two systems were utilized for metallization. The first is a 1 inch d.c. AJA International Inc. magnetron sputter source attached to a 10-inch inner diameter UHV stainless steel spherical reactor chamber with a base pressure below  $1 \times 10^{-7}$  Torr. This system was utilized to deposit Au and Cr (~300 nm each). Au was sputtered at 20 W, and Cr was sputtered at 30 W. Both metals were sputtered in an  $\text{Ar}^+$  plasma at a pressure of 5 mTorr. The second system utilized was a “Hex Deposition System” purchased from Mantis Deposition Inc. It is capable of magnetron sputtering, e-beam evaporation, and thermal evaporation. The 2-inch magnetron sputtering source was utilized to deposit Al (~500 nm).

Direct Current (d.c.) sputtering is a thin film physical vapor deposition technique where a target material, the material to be used for coating, is bombarded with ionized gas molecules with sufficient energy to displace clusters of atoms “sputtering” them off of the target. These ballistically vaporized clusters of atoms are ejected hemispherically outward to condense on the substrate to be coated as well as chamber walls. To minimize the deposition on chamber walls, and increase directionality of film deposition, chimneys are sometimes installed. Fig 2.3 shows a schematic of the d.c. magnetron sputtering process including the magnetic and electric fields.

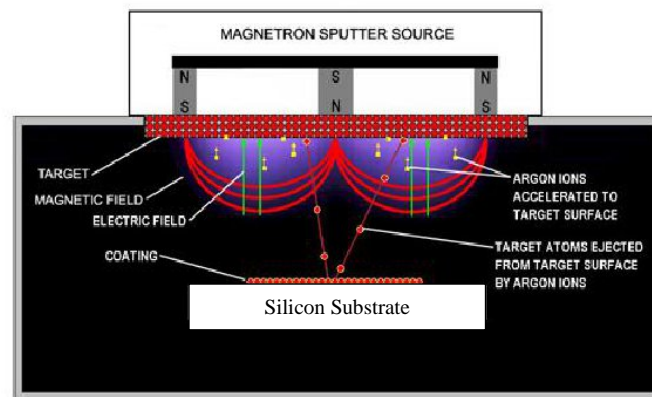


Fig. 2.3: Schematic of a d.c. magnetron sputtering process in a sputter down configuration. After [7].

When selecting a metal to create the connecting electrode, the workfunction ( $\Phi$ ) of the metal must be taken into account. Ideally, the metal to semiconductor contact will form an ohmic contact, and not interfere or modify the electrical measurements to be performed in characterizing the electrical device. The workfunction of a semiconductor has two distinct parts, the electron affinity ( $\chi$ ), and the energy difference between the conduction band energy level ( $E_C$ ) and the Fermi-Energy level ( $E_F$ ).

Equation 2-1

$$\Phi_S = \chi + (E_C - E_F)$$

It should be noted that  $\Phi_M$  (workfunction of the metal) and  $\chi$  are material constants and remain unaffected by the contacting process. After the contacting of the metal and the semiconductor, the electrons will begin to transfer from the material with the lower workfunction to the material with the higher workfunction. The material that loses electrons will become less n-type, the material that gains electrons will become more n-type. This will be reflected in the appropriate band bending at the metal-semiconductor interface. Fig. 2.4 shows what such band bending looks like for an n-type semiconductor, such as the n-type Si used as a substrate in device design.

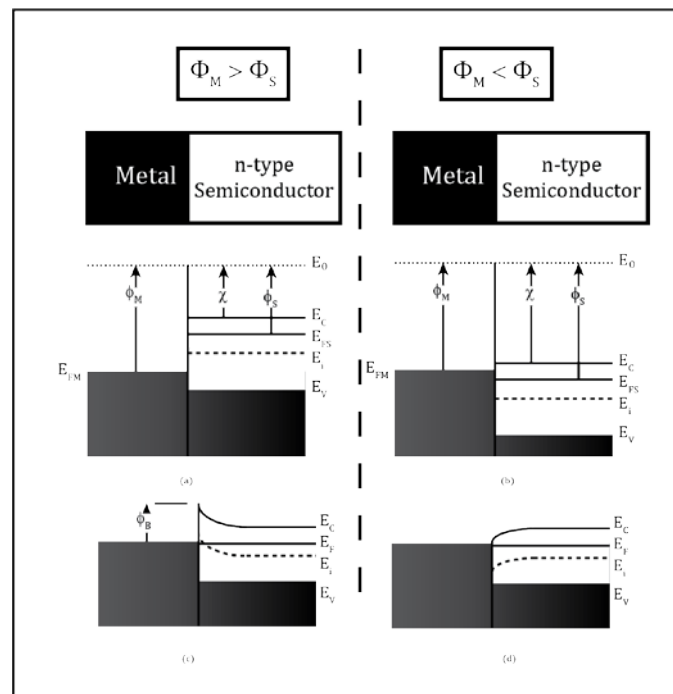


Fig. 2.4: Energy band diagrams for ideal MS contacts between a metal and an n-type semiconductor:  $\Phi_M > \Phi_S$  system (a) an instant after contact formation and (b) under equilibrium conditions;  $\Phi_M < \Phi_S$  system (c) an instant after contact formation and (d) under equilibrium conditions. Reproduced from [8].

Table 2.1 presents the metal-semiconductor (MS) selection rule indicating whether the MS contact formed will result in a Rectifying contact or Ohmic contact [8].

Table 2-1: Electrical Nature of Ideal MS Contacts

	n-type Semiconductor	p-type Semiconductor
$\Phi_M > \Phi_S$	Rectifying	Ohmic
$\Phi_M < \Phi_S$	Ohmic	Rectifying

It has been shown that PECVD synthesized semiconducting boron carbide films utilizing 1,7-Dicarbadoecaborane,  $B_{10}C_2H_{12}$ , (m-carborane), as the source molecule tend to produce n-type films[9]. It has recently been shown that said films make an Ohmic contact with Au ( $\Phi_M = 5.1$ ) [10]. It remains an open focus of research to determine which metals form Ohmic contacts with PECVD synthesized boron carbide with o-carborane as the source molecule.

For this research, a set of shadow masks were utilized with the d.c. magnetron sputtering systems for the deposition of the top and bottom contacts. The top shadow mask had 4 circles drilled (2 mm diameter) through stainless steel sheeting. The bottom shadow mask was created by an acid etching process (Photo Etch Technology) that created a set of 4 mm by 8 mm rectangles designed to overlap the circles of the top shadow mask. All 6 metal contacts then had a copper wire affixed by silver paint. Images of the top and bottom metallization are shown below in Fig. 2.5.

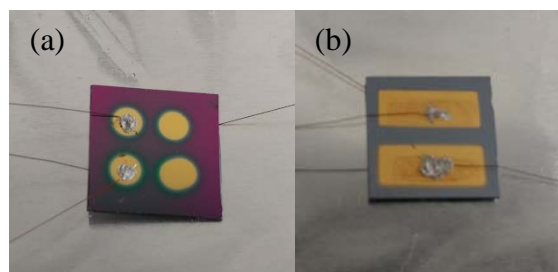


Fig. 2.5: 1 cm×1 cm sample showing (a) the top of a sample with 4 circular Cr/Au contacts each 2 mm in diameter and (b) the bottom of a sample with 2 rectangular Cr/Au contacts each 4 mm×8 mm. The bottom contacts are designed to overlap the circular contacts to provide a perpendicular flow of charges.

### 2.3 Transmission Electron Microscopy (TEM)

Transmission electron microscopy (TEM) is a technique where electrons are passed through a thin sample. Depending on how the electrons interact with the sample, diffracting off of the crystal structure, transmission through the sample, or scattering off of the sample, an image is formed. TEM images shown in this work were obtained in bright field mode, where the greater the transmission of electrons through the material, the greater the intensity, and the brighter that region of the image will appear. Thicker regions, regions with higher concentrations of scattering centers, and regions with elements of higher atomic number ( $Z$ ) will appear darker.

High Resolution Transmission Electron Microscopy (HRTEM) provides images with resolutions in the range of 0.25 nm (according to FEI's specifications), allowing for the examination of the atomic structure of a sample. In this configuration, the microscope is capable of looking at stacks of atoms with the stacks appearing either light or dark depending on whether the microscope is slightly under-focused or slightly over-focused.

Selected area electron diffraction (SAED) uses an aperture to examine the crystal structure of a specific area of the sample. The aperture is a thin strip of metal with a small hole in it. Placing the aperture in the electron beam path has the effect of blocking all electrons except for those that traverse through the small hole. By moving the location of the hole, the user may examine specific locations of the sample. In the diffraction configuration, the microscope detects electrons that have been diffracted off the lattice planes. Only electrons interacting with the sample lattice planes at specific angles will meet the Bragg condition for diffraction:

*Equation 2-2*

$$2d \sin(\theta) = n\lambda$$

Where  $d$  is the interplanar distance,  $\theta$  is the scattering angle,  $\lambda$  is the incident wavelength, and  $n$  is an integer multiple. These specific angles converge as spots representing the crystal lattice in reciprocal space. This is very similar to x-ray diffraction patterns, except that SAED allows for the examination of an area of the sample as small as several nanometers in length. Fig 2.6 a) shows the schematic of a transmission electron microscope without the SAED aperture inserted yielding a bright-field image, and b) with the SAED aperture inserted providing the diffraction pattern of the sample.

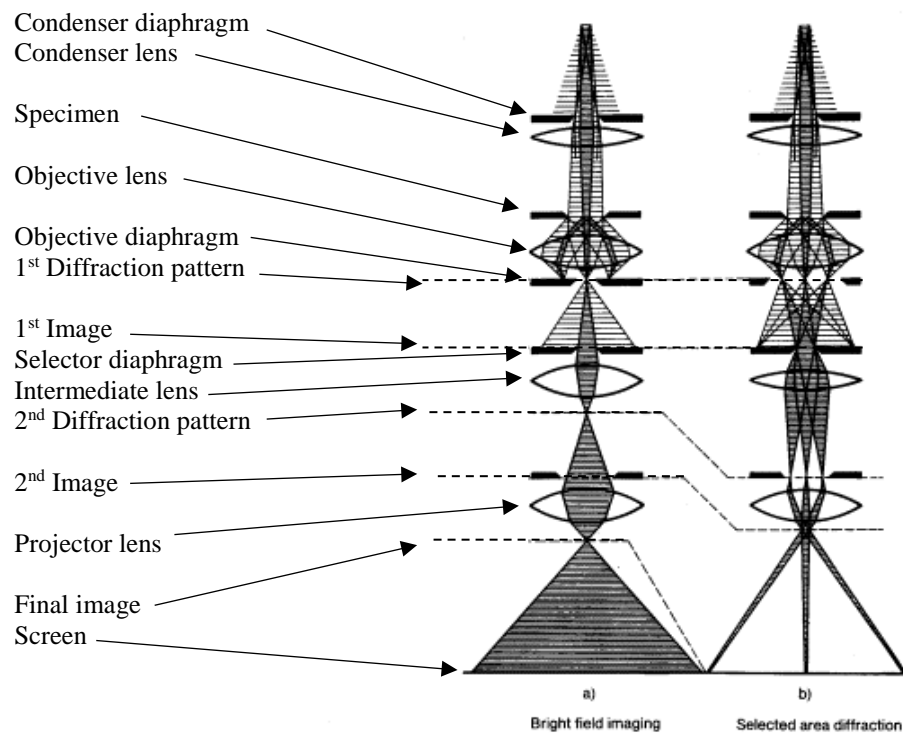


*Fig. 2.6: Schematic representation of a transmission electron microscope where a) has an aperture that blocks diffracted electrons and transfers transmitted electrons down the microscope (focal plane) and b) has the selected area aperture inserted at the back focal plane, and transfers the diffracted electrons down the microscope, after [11].*

The analysis of SAED patterns can reveal many important qualities and characteristics of the material being studied. The intensity ( $I$ ) of the diffracted beam is proportional to the square of the structure factor ( $F$ ) of the material.

*Equation 2-3*

$$I \propto |F|^2$$

The structure factor is a mathematical function describing the amplitude and phase of a wave diffracted from a crystal lattice plane characterized by Miller indices (h k l):

*Equation 2-4*

$$F = \sum_{i=1}^n f_i e^{-2\pi i(hu_i + kv_i + lw_i)}$$

where  $(u_i \ v_i \ w_i)$  are the unit cell coordinates of the atoms (i.e. for body centered cubic  $(u_1 \ v_1 \ w_1)$  are the set  $\left\{(0 \ 0 \ 0), \left(\frac{1}{2} \ \frac{1}{2} \ \frac{1}{2}\right)\right\}$ ),  $f_i$  is the atomic scattering factor, and  $n$  is the number of constituent atom structures in the sample. Making use of the mathematical identities:

*Equation 2-5*

$$e^{n\pi i} = 1 \text{ if } n \text{ is even}$$

$$e^{n\pi i} = -1 \text{ if } n \text{ is odd}$$

It is then possible to calculate which planes are forbidden, or allowed, in the diffraction pattern. Using body centered cubic as an example, for  $h + k + l = \text{odd} \rightarrow F = 0$ , and those sets of crystallographic planes  $\{1 \ 0 \ 0\}, \{1 \ 1 \ 1\}, \{2 \ 1 \ 0\} \dots$  will be absent from the SAED pattern.

Fig. 2.7 provides an example of an image and diffraction pattern of a highly organized crystal system. The data is taken from  $\text{Zn}_2\text{SnO}_4$  nanowires formed in a rhombohedral crystal structure. Fig 2.7 (a) shows that the unit cell is complex, but the inset of (d) demonstrates that the SAED pattern provides useful crystallographic information.

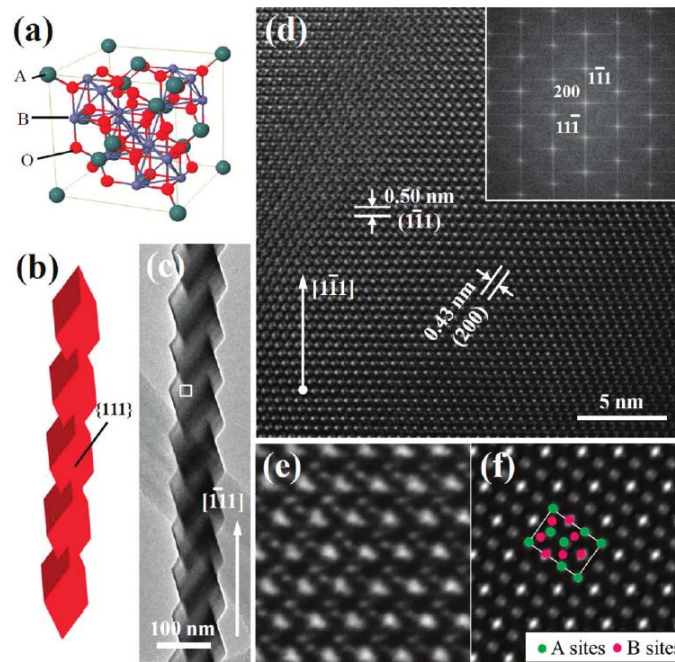
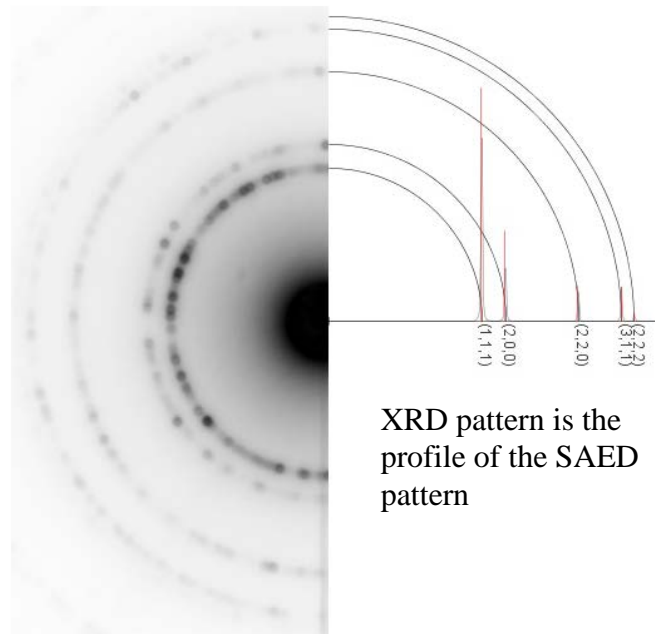


Fig. 2.7: (a) Structure of a spinel ( $AB_2O_4$ ) unit cell. (b) Schematic of a  $Zn_2SnO_4$  nanowire formed by periodic rhombohedral crystals that are enclosed by  $\{111\}$  equivalent facets. (c) TEM image of a  $Zn_2SnO_4$  nanowire. (d) HRTEM image of the boxed area in (c). Inset is the FFT (SAED equivalent) image that shows the nanowire's  $[111]$  growth direction. (e) Enlarged HRTEM image and (f) corresponding NCEMSS simulation result. Reprinted with permission from [12]. Copyright (2012) American Chemical Society.

When the sample is not as highly organized as in Fig. 2.7, but instead has many crystalline parts that are randomly oriented with respect to each other, that is considered polycrystalline. In polycrystalline samples, the Bragg condition and structure factor calculations do not change, but many orientations of the same diffraction pattern will be displayed simultaneously. If enough of these random orientation diffraction patterns display simultaneously, they become diffraction rings instead of diffraction spots, as illustrated in Fig. 2.8. The data displayed in Fig. 2.8 is obtained from a polycrystalline Al sample, both SAED and x-ray diffraction (XRD) data is displayed. Experimental SAED data is displayed on the left half. Calculated polycrystalline SAED are displayed as solid rings on the right half, and are overlaid with XRD data as red lines labeled with crystallographic planes. An important note is that the profile of the SAED pattern becomes the intensity of the XRD measurement.



*Fig. 2.8: The experimental SAED pattern, overlaid by the calculated SAED pattern, and experimental XRD pattern of polycrystalline Al in the top right quadrant.*

As samples become even less organized, losing or lacking long-range order (becoming amorphous), the peaks of the XRD pattern begin to broaden. Since the profile of the SAED pattern is the XRD pattern, this means that the rings of the SAED pattern are no longer sharp as in Fig. 2.8, but also broaden, becoming what is termed amorphous halos. This is shown in Fig. 2.9.



*Fig. 2.9: Selected Area Electron Diffraction (SAED) pattern obtained from silica superstructures showing amorphous halos. Reprinted with permission from [13].*

A very thorough description of these and other more complicated analytical techniques may be obtained by reading *Transmission Electron Microscopy: a textbook for materials science* by David B. Williams and C. Barry Carter [11].

All cross-section TEM samples in this work were prepared from semiconducting amorphous partially dehydrogenated boron carbide films using standard gluing, mechanical grinding and polishing procedures, followed by a low energy (3.7 keV) ion milling. Images were acquired with an FEI Tecnai Osiris (S)TEM electron microscope.

## 2.4 Secondary Ion Mass Spectroscopy (SIMS)

Secondary ion mass spectroscopy (SIMS) is a destructive analysis technique that examines the mass spectroscopy of ionized particles that have been emitted from a material following irradiation from an energetic primary ion beam [14]. Fig. 2.10 shows that this is fundamentally a sputtering process.

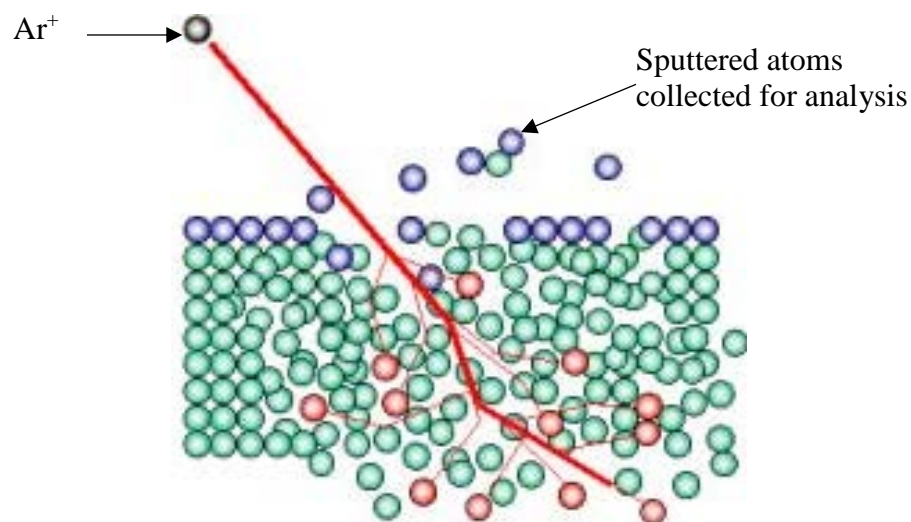


*Fig. 2.10: Schematic of the SIMS irradiating ion and resulting collision cascade, after [15]. The sputtered ionized particles, secondary ions, are collected and analyzed.*

When the energetic primary ion beam, typically Ar, Xe, or Cs, impacts the sample surface, energy is transferred from the irradiating ion to the sample material. Generally, this transfer of energy provides kinetic energy to the target lattice and results in ion implantation of the primary beam ions (though occasionally they are back scattered depending on mass and irradiating angle). The transfer of kinetic energy results in the ejection low energy electrons, auger electrons, photons, x-rays,

neutral particles, excited clusters, and ionized particles [16]. These ejected ionized particles are termed secondary ionized particles since they did not originate in the primary ion beam. Of the ejected material, the mass spectrometers are only capable of detecting the ionized particles. The detector, there are many versions [14], ion current generated by the secondary ion particles is described by:

Equation 2-6

$$I_m = I_p \times Y_m \times \alpha \times \theta_m \times \eta$$

Where  $y_m$  is the secondary ion current of species  $m$ ,  $I_p$  is the primary ion flux,  $Y_m$  is the sputter yield,  $\alpha$  is the ionization probability,  $\theta_m$  is the fractional concentration of species  $m$  in the surface layer and  $\eta$  is the transmission of the analysis system. It is important to note that  $Y_m$  is the total yield, neutral and ionic, per primary impact. Fig. 2.11 provides an example of what the data from a SIMS measurement provides.

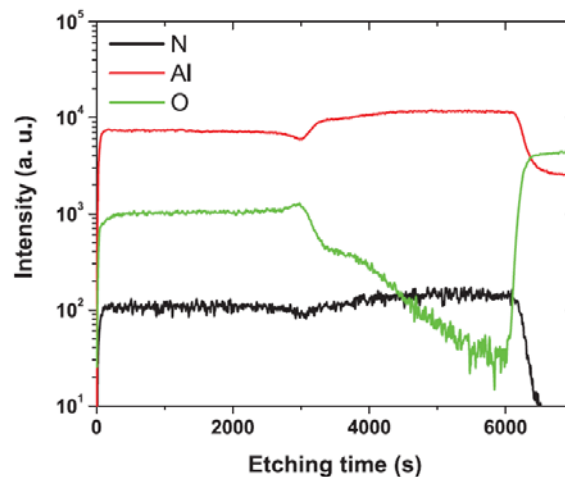


Fig. 2.11: SIMS chemical profile of AlN/IDT/AlN/Sapphire heterostructure. Reprinted with permission from [17], copyright (2016), IEEE.

If the sample atomic concentration, sputter rate, and sample thickness are known quantities, usually through the use of a standard, then further analysis is possible providing a chemical composition *versus* film depth profile as shown in Fig. 2.12. For this research, EAG, Inc. performed SIMS measurement and analysis. A standard

obtained by elastic recoil detection was provided to EAG, Inc. allowing for the depth profile analysis shown in Fig. 2.12.

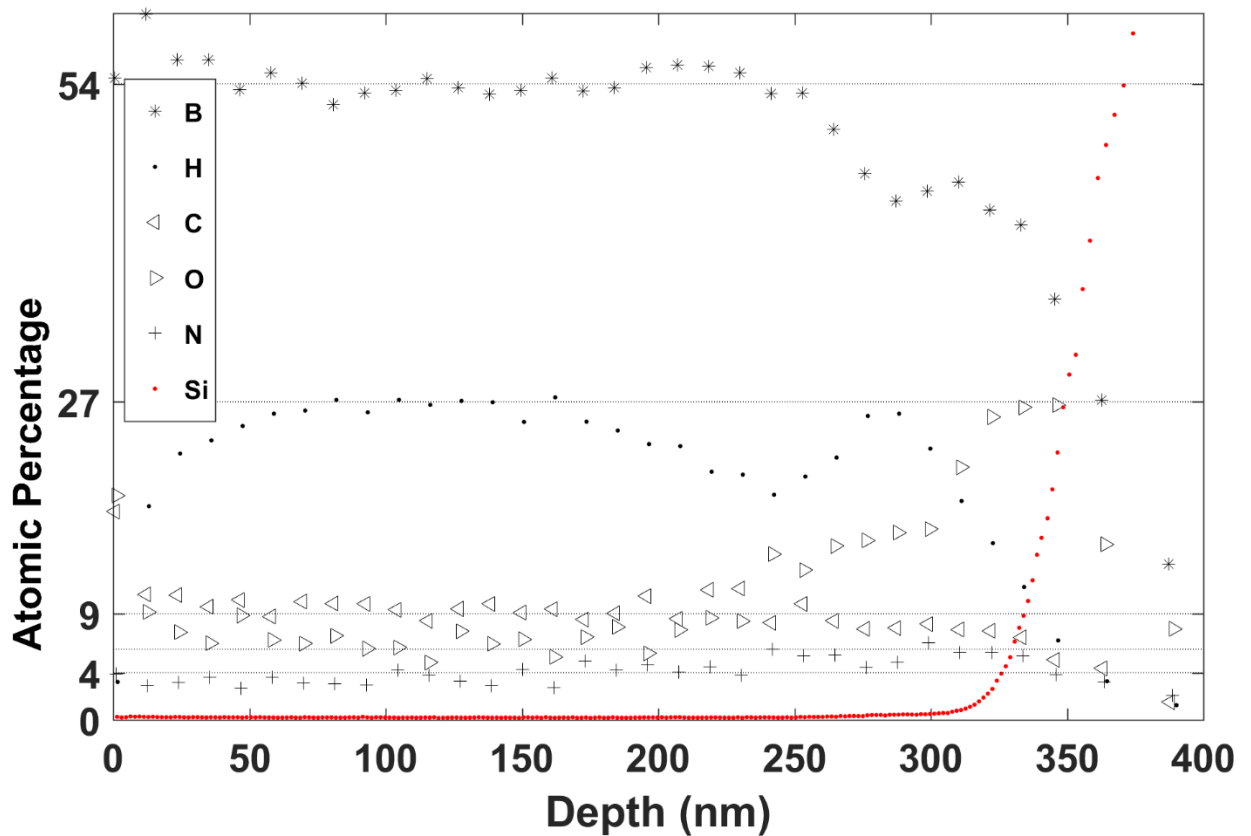


Fig. 2.12: SIMS depth profile showing elemental atomic percentage as a function of film depth for amorphous semiconducting partially dehydrogenated boron carbide on Si. The mean film composition is taken as 54 at% B, 27 at% H, 9 at% C, 6 at% O, 4 at% N.

## 2.5 Elastic Recoil Detection (ERD)

Elastic recoil detection (ERD) is a form of forward recoil spectroscopy. This form of spectroscopy uses an incident particle with a mass equal to or larger than that of the target atoms. The incident energy is then primarily transferred to the lighter target atoms in a recoil collision as described by:

Equation 2-7

$$\frac{E_2}{E_0} = \frac{4M_1M_2}{(M_1 + M_2)^2} \cos^2(\theta)$$

Where  $E_0$  is the monoenergetic incident ion energy,  $M_1$  is the mass of the incident ion,  $M_2$  is the mass of the target atom, and  $\emptyset$  is the recoil angle. The experimental geometry is shown in Fig. 2.13.

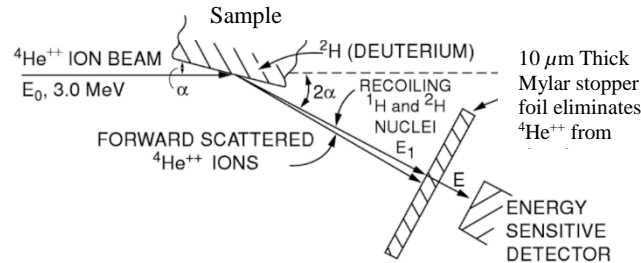


Fig. 2.13: Experimental geometry for forward recoil spectrometry experiments to determine depth profiles of  $^1\text{H}$  and  $^2\text{H}$  in solids, after [18].

The depth profiles are determined by the energy loss of the incident ion along the inward path and the energy loss of the recoil ion(s) along the outward path. By setting the incident beam to an angle  $\alpha$ , and the detector to an angle  $2\alpha$ , the path length is the same for both the penetrating ion and the forward recoil (outward) ion. From Equation 2-8, a target recoil ion originating at the surface will have an energy  $E_2 = K'E_0$ , where  $K'$  denotes the recoil kinematic factor, and is experimentally obtained for specific angles using standards. Recoils obtained at the back surface (of sample thickness  $t$ ) will have an energy:

Equation 2-8

$$E_2(t) = K'E_0 - K'\Delta E_{ion} - \Delta E_{recoil}$$

Where  $\Delta E_{ion}$  is the energy loss of the penetrating ion along the inward path, and  $\Delta E_{recoil}$  is the energy loss of the recoil ion along the outward path:

Equation 2-9

$$\Delta E_{ion} = \left. \frac{dE}{dx} \right|_{ion} \frac{t}{\sin(\alpha)}$$

$$\Delta E_{recoil} = \left. \frac{dE}{dx} \right|_{recoil} \frac{t}{\sin(\alpha)}$$

Where  $dE/dx|_{ion}$ , the stopping power of the target on the penetrating ion, is evaluated at  $E_0$  and  $dE/dx|_{recoil}$ , the stopping power of the target on the recoil ion, is evaluated at  $E_2$  [18]. Fig. 2.14 plots data obtained using 40 MeV Ni ions incident on amorphous semiconducting partially dehydrogenated boron carbide on Si. The data is plotted in atoms/cm<sup>2</sup>. By dividing the data by the atomic concentration of the sample, a more familiar depth profile may be obtained (i.e. cm). The data of Fig. 2.14 was used as the standard in the SIMS analysis shown in Fig. 2.12.

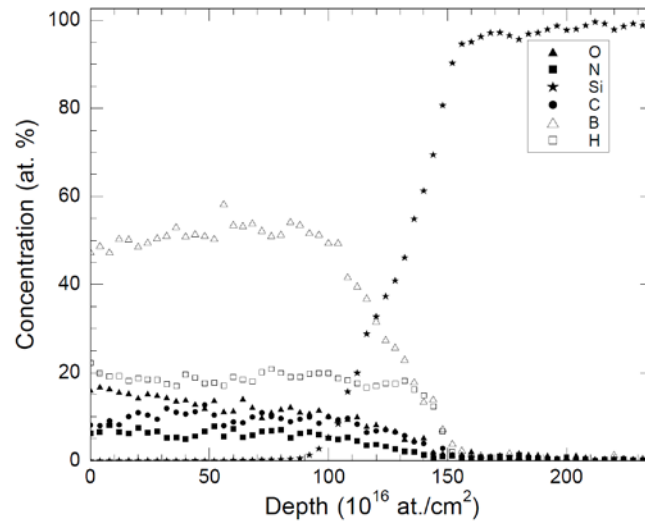


Fig. 2.14: Elastic Recoil Detection data of incident 40 MeV Ni ions upon amorphous semiconducting partially dehydrogenated boron carbide on Si.

## 2.6 Current versus Voltage Measurements

In order to characterize an electrical device using a current *versus* voltage  $I(V)$  measurement, one must first have a base understanding of the device being measured. Although the electrical response of a p-n junction diode and a metal-semiconductor (Schottky barrier) device appear similar, they are fundamentally different devices. A p-n junction diode is a minority carrier based device and a Schottky barrier device is a majority carrier based device. As such, the governing equations of  $I(V)$  for each are

vastly different. An examination of the band structure of a p-n junction diode based device will provide better context of what is being measured.

Let us consider the simplified case of a homojunction, a junction created from the same base material though doped to have differing carrier concentrations. An example of this would be a silicon junction with the n side of the junction being silicon doped with phosphorous (providing a donor electron), and the p side of the junction being silicon doped with boron (providing an acceptor site). Let  $\bullet$  represent an electron, and  $\circ$  represent a hole. Further, let  $E_C$  be the conduction band,  $E_F$  be the Fermi Energy level,  $E_V$  be the valence band, and  $E_i$  be the intrinsic energy level. Then Fig. 2.15 crudely illustrates the equilibrium energy band diagram ( $V_A = 0$ ).

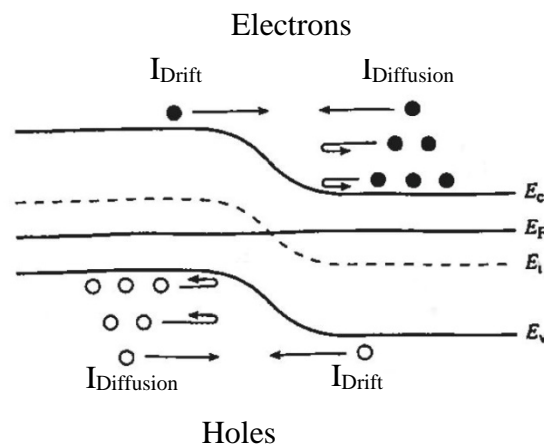


Fig. 2.15: p-n junction diode energy band diagram, carrier distribution, and carrier activity close to the depletion region at equilibrium ( $V_A=0$ ). Notice that the diffusion current and drift current cancel each other out. After figure from [8].

In this condition, most of the carriers do not have sufficient energy to overcome the potential barrier, and so are turned back by the electric field created within the depletion region. However, there are some high-energy electrons in the n side quasi-neutral region with sufficient energy to overcome the potential barrier and cross to the p side. Similarly, there are some high-energy holes in the p side quasi-neutral region with sufficient energy to overcome the potential barrier and cross to the n side. These

processes are the diffusion of charge carriers from high concentration regions to low concentration regions. This is defined as the diffusion current.

Electrons in the p side, though low in concentration, are not restricted in any way from crossing to the n side of the junction, nor are holes in the n side restricted. The electric field therefore sweeps away any charge carriers that randomly wander, or drift, into the depletion region. This is defined as the drift current. However, this p to n electron drift **exactly** matches the n to p electron diffusion current under equilibrium conditions, and so cancels each other out. Similarly, the n to p hole drift current **exactly** matches the p to n hole diffusion current, also cancelling each other out. Thus, according to the ideal diode equation (Equation 2-10 shown below), at  $V_A = 0$ , the current equals 0.

Equation 2-10

$$I = I_0 \left( e^{(qV_A/nkT)} - 1 \right)$$

Equation 2-11

$$I_0 = qA \left( \frac{D_N}{L_N} \frac{n_i^2}{N_A} + \frac{D_P}{L_P} \frac{n_i^2}{N_D} \right)$$

Where  $q$  is the elemental charge,  $V_A$  is the applied voltage,  $n$  is the ideality factor (1 for ideal),  $k$  is the Boltzmann constant,  $T$  is the device temperature (in °K),  $A$  is the area of the metal contact,  $D_N$  is the electron diffusion coefficient,  $L_N$  is the electron diffusion length,  $n_i$  is the intrinsic carrier concentration,  $N_A$  is the acceptor carrier concentration,  $D_P$  is the hole diffusion coefficient,  $L_P$  is the hole diffusion length, and  $N_D$  is the electron carrier concentration.  $I_0$  is also known as the dark current, or the saturation current. A current *versus* voltage plot of a diode that follows the ideal diode equation behavior, until breakdown is reached near -37 volts, is shown in Fig. 2.16.

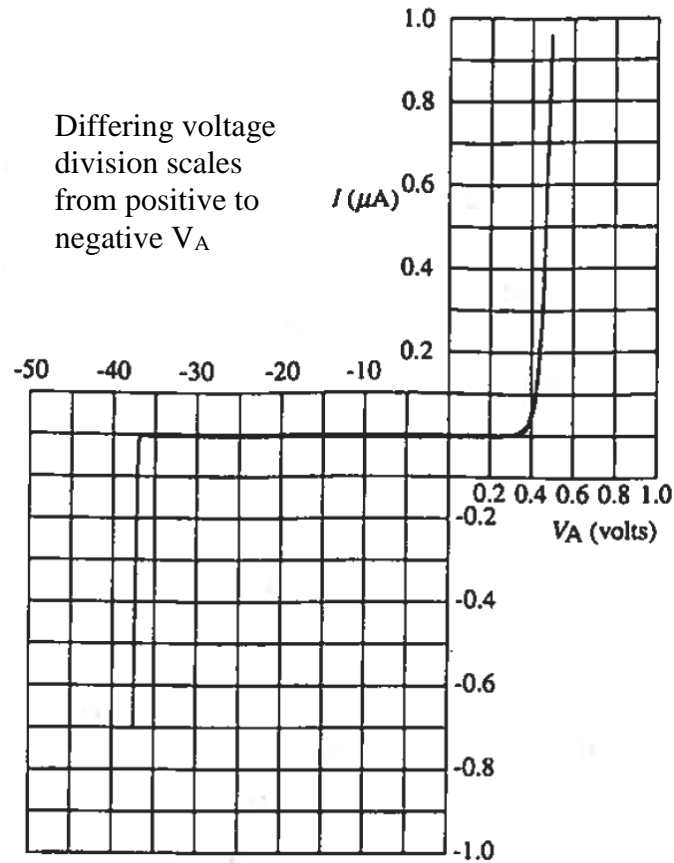


Fig. 2.16: Linear plot of the measured  $I(V)$  characteristics derived from a commercially available Si p-n junction diode at room temperature. The plot permits a course evaluation of the diode characteristic. Note the change in voltage scale in going from forward to reverse bias. After figure from [8].

When the p-n junction diode is forward biased ( $V_A > 0$ ), as defined by the positive voltage contacted to the p side, if one assumes the resistive voltage drop across the quasi-neutral regions are minimal, the applied voltage must be applied across the depletion region. This externally applied voltage lowers the potential barrier on the n side in relation to the p side, as shown in Fig. 2.17. From Equation 2-10 we see that as the barrier is lowered an exponentially increased number of charge carriers have enough energy to overcome the potential barrier, resulting in an exponential increase in the current flow.

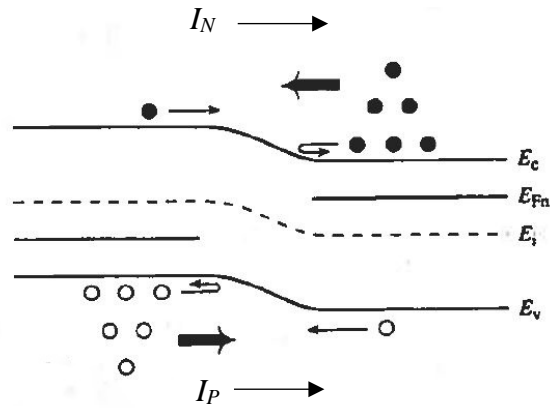


Fig. 2.17: p-n junction diode energy band diagram, carrier distribution, and carrier activity close to the depletion region under forward bias ( $V_A > 0$ ). Notice that the diffusion current is now significantly greater than the drift current. After figure from [8].

Naturally, when the applied bias is reversed ( $V_A < 0$ ), the voltage has the opposite effect i.e. an increase in the potential barrier. This is shown in Fig. 2.18. In this configuration, the only contribution to current in the ideal case is due to the drift current. For a more detailed discussion on this topic, many text books and online resources provide the electrostatics and derivations of the diffusion equations for p-n junction diodes [8,19].

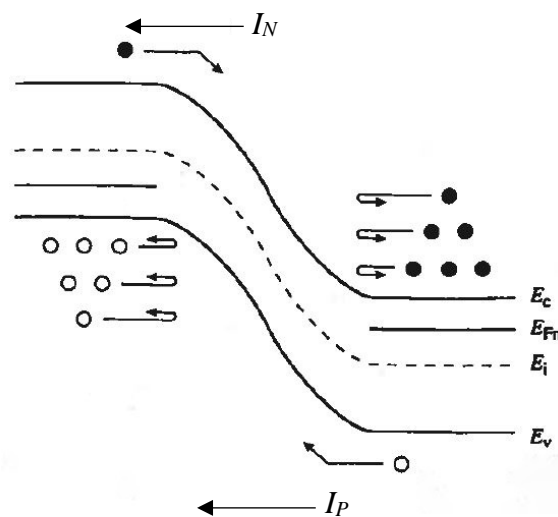


Fig. 2.18: p-n junction diode energy band diagram, carrier distribution, and carrier activity close to the depletion region under reverse bias ( $V_A < 0$ ). Notice that the drift current is the only contribution to current flow. After figure from [8]

The above discussion assumes an ideal diode. In working with a real device, one must also account for series resistance. The quasi-neutral regions of the n and p material have an inherent resistance that is determined by the doping and geometry of the regions. Further, there can be a contact or junction resistance between the material and metallization contacts, the wires between the p-n junction diode and the measurement equipment, and the power supply itself. To account for the series resistance ( $R_S$ ), one replaces  $V_A$  in Equation 2-10 with  $V_J$  where:

Equation 2-12

$$V_J = V_A - IR_S$$

resulting in:

Equation 2-13

$$I = I_0 \left( e^{(q(V_A - IR_S)/nkT)} - 1 \right) \quad V_A \rightarrow V_{bi}$$

where  $V_{bi}$  is the built in voltage of the p-n junction diode. Equation (2-13) is a transcendental equation that cannot be solved for  $I$  as a function of  $V_A$ . However, if  $R_S$  is known, one can assume a set of  $V_J$  values (for example a set of voltages provided by a power supply), and then compute  $V_A$  using Equation (2-13).  $V_A$  may then be plotted *versus* the measured current values obtained for an accurate plot that corrects for the effects of series resistance.

When comparing real data to the theory of the ideal diode equation provided in either Equation 2-10 or Equation 2-13, a measured current is found to be much greater than that predicted in the small forward bias, and the entire reverse bias regions. In the small forward bias region, this excess current is due to thermally excited charge carriers that result in recombination-generation current ( $I_{R-G}$ ) in the depletion region of the p-n junction diode. Reverse biasing reduces the carrier concentration in the depletion region below the equilibrium values. In order to go

back to a neutral state, charge carriers are thermally generated or injected into the region in an attempt to return to equilibrium, leading to a contribution to the current in excess of that predicted. Forward biasing increases the charge concentration of the depletion region above the equilibrium values. The increased concentration in both electrons and holes in the depletion region gives rise to recombination as an electron encounters a hole. As such, the current through a p-n junction diode under forward bias (positive voltage) is comprised of two components: a diffusion current ( $I_{Diff}$ ) and a recombination-generation current ( $I_{R-G}$ ). The combined forward and reverse bias current is then described by:

Equation 2-14

$$I_{Diff} = qA \left( \frac{D_N}{L_N} \frac{n_i^2}{N_A} + \frac{D_P}{L_P} \frac{n_i^2}{N_D} \right) \left( e^{(qV_A/kT)} - 1 \right)$$

Equation 2-15

$$I_{R-G} = \frac{qAn_i}{2\tau_0} W \frac{\left( e^{(qV_A/kT)} - 1 \right)}{\left( 1 + \frac{V_{bi} - V_A}{kT/q} \frac{\sqrt{\tau_n \tau_p}}{2\tau_0} e^{(qV_A/kT)} \right)}$$

Equation 2-16

$$W = \left[ \frac{2\epsilon_1 \epsilon_0}{q} \left( \frac{N_A + N_D}{N_A N_D} \right) (V_{bi} - V_A) \right]^{1/2}$$

Equation 2-17

$$\tau_0 \equiv \frac{1}{2} \left( \tau_p e^{(E_T - E_i)/kT} + \tau_n e^{(E_i - E_T)/kT} \right)$$

Equation 2-18

$$I = I_{Diff} + I_{R-G}$$

Where  $W$  is the depletion width,  $\epsilon_1$  is the dielectric constant,  $\epsilon_0$  is the permittivity of free space,  $N_A$  is the acceptor concentration in the p side,  $N_D$  is the donor

concentration in the n side,  $\tau_n$  is the electron lifetime,  $\tau_p$  is the hole lifetime,  $E_T$  is the trap energy level, and  $E_i$  is the Fermi level energy of an intrinsic semiconductor.

The previous discussion is all based on the concept of a homojunction p-n junction diode. This discussion is all valid for the situation that the electron affinity and band gap (or HOMO-LUMO gap (Highest Occupied Molecular Orbital – Lowest Unoccupied Molecular Orbital)) are roughly equivalent. Any deviation in either the n or p region, and the situation becomes much more involved. The best source for discussion is usually found within the context of a bipolar heterojunction transistor (BJT) [8,20]

For this research, all  $I(V)$  measurements were obtained using a Keithley 2411B SourceMeter to deliver a dc voltage, a Keithley 6485 PicoAmmeter to measure the resulting current, and a HP 3478A Multimeter to measure the voltage across the device under test.

## 2.7 Capacitance versus Voltage Measurements

The junction region of a p-n junction diode contains both capacitive ( $C$ ) and conductive ( $G$ ) components. In order to probe these components, a sinusoidal perturbation voltage is superimposed over a d.c. voltage giving rise to an a.c. current in response. The diode response in general exhibits an admittance ( $Y$ ) taking the form:

*Equation 2-19*

$$Y = G + j\omega C$$

Where  $j = \sqrt{-1}$  and  $\omega$  is the angular frequency ( $\omega = 2\pi f$ ), and  $f$  is the small signal perturbation frequency. Similar to the  $I(V)$  measurement, both the capacitance and conductance are also functions of the d.c. voltage.

It is convenient to begin by examining the reverse biased admittance because the conductance in reverse bias is small in a good diode. The result is that  $Y \cong j\omega C$ .

In addition, the reverse bias capacitance is the result of majority carrier oscillations inside the p-n junction diode. It is key to keep the small signal perturbation voltage on the order of a few tens of millivolts or less. The depletion width changes with applied bias. In reverse bias, the depletion width is getting larger. A small perturbation voltage ensures that the changes in depletion width at the d.c. voltage point (steady state depletion width) is small. Remember, there can be no capacitance without the change in charge. It is this change in charge at the edge of the depletion region, resultant from the d.c. voltage, that gives rise to the reverse bias capacitance, and which is defined as the junction capacitance ( $C_J$ ).

*Equation 2-20*

$$C_J = \frac{\epsilon_1 \epsilon_0 A}{\left[ \frac{(m+2)\epsilon_1 \epsilon_0}{qN_B} (V_{bi} - V_A) \right]^{1/(m+2)}}$$

Where  $m$  is the profile parameter ( $m = 1$  for linearly graded,  $m = 0$  for step,  $m = -1$  for hyper-abrupt junctions), and  $N_B$  is the carrier concentration ( $N_A$  or  $N_D$ ) of the side with the smaller carrier concentration (lightly doped side).

It is of particular interest that  $C_J$  is frequency independent. Physically, it does not matter how rapidly the depletion width changes, just that there is a change in charge about the edge of the depletion width. If multiple measurements are taken and differing perturbation frequencies (i.e. 10 kHz, 100 kHz, 1 MHz) and the reverse bias capacitance values are not identical, there are multiple capacitive components present. These could include interface states, trap states, or defect density distributions within the diode.

The forward bias admittance is a combination of both the majority and minority carriers. The majority carriers in forward bias will continue to respond to the junction capacitance. In addition, there will be a significant contribution from the

minority carrier charge oscillation in response to the perturbation signal. However, the minority carrier response is not frequency independent. The supply and removal of minority carriers is not as rapid as that of the majority carriers because of the reduced concentration: they must travel farther to meet the supply and demand of the perturbation in attempting to maintain equilibrium. At angular frequencies approaching the inverse of the minority carrier lifetimes, the minority carrier charge oscillation starts to move in an out-of-phase spatial variation. This out-of-phase charge oscillation ceases to contribute to the capacitance of the diode, and instead contributes to the conductance. Forward biasing creates a diffusion current which causes a buildup of minority carriers in the quasineutral regions adjacent to the depletion region. This buildup of minority carriers due to the diffusion current results in the forward bias admittance being identified as the diffusion admittance:

*Equation 2-21*

$$Y_D = G_D + j\omega C_D$$

Where  $G_D$  and  $C_D$  are the diffusion conductance and diffusion capacitance respectively. Through the use of an impedance analyzer, the admittance of a diode may be measured. We see from Equation (2-21) that  $Y_D$  may be separated into the real and imaginary components,

*Equation 2-22*

$$G_D = \frac{G_0}{\sqrt{2}} \left( \sqrt{1 + \omega^2 \tau_p^2} + 1 \right)^{1/2} \rightarrow p^+ - n \text{ diode}$$

*Equation 2-23*

$$C_D = \frac{G_0}{\omega\sqrt{2}} \left( \sqrt{1 + \omega^2 \tau_p^2} - 1 \right)^{1/2} \rightarrow p^+ - n \text{ diode}$$

*Equation 2-24*

$$G_0 = \frac{dI}{dV_a}$$

Where  $G_0$  is the low frequency differential diode conductance, and  $p^+$  is a p-n junction diode with the p side having a carrier concentration significantly higher than the carrier concentration of the n side.  $G_0$  may be directly taken by numeric differentiation of measured  $I(V)$  data. Taking the majority and minority carriers in consideration together, the small signal response of a p-n junction diode has three parallel components: junction capacitance, diffusion capacitance, and diffusion conductance. Typical capacitance *versus* voltage data of a p-n homojunction diode (Vishay Semiconductors Inc.) is shown in Fig. 2.19. The left axis plots the capacitance in nF, and the right axis plots  $1/C^2$  which shows the small forward bias linear region. This region is often extrapolated to the applied bias intercept for an experimental determination of the device built-in potential.

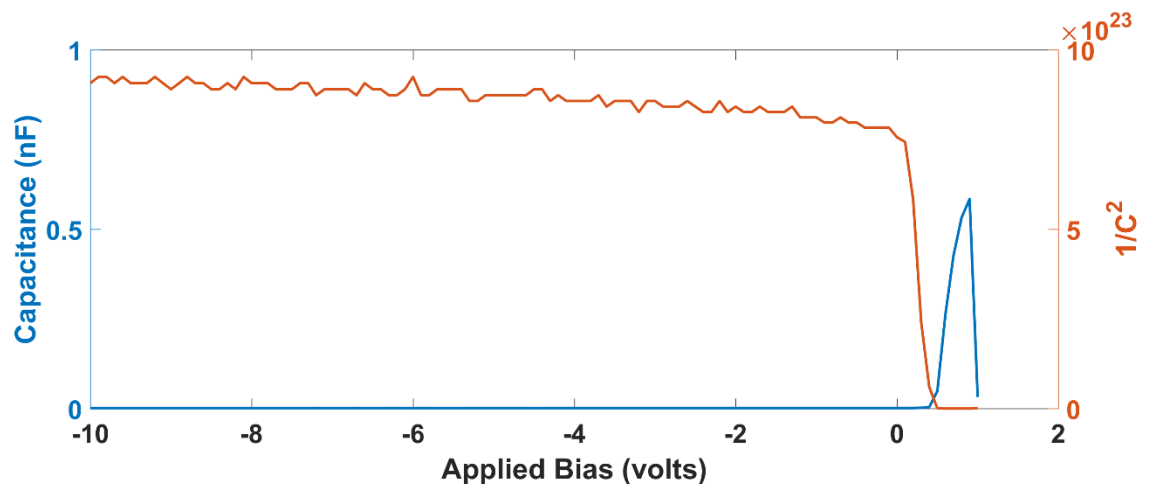


Fig. 2.19: Capacitance versus Voltage curve (left axis) and  $1/C^2$  versus Voltage (right axis) data obtained from a commercial silicon epitaxial planar diode (purchased from Vishay Semiconductors) taken at 100 kHz.

For this research, all  $C(V)$  measurements were obtained using an HP model 4192A impedance analyzer with an oscillation voltage set to 0.010 V in a 4-point parallel circuit.

## 2.8 References

- [1] C. Pallier, J.-M. Leyssale, L.A. Truflandier, A.T. Bui, P. Weisbecker, C. Gervais, H.E. Fischer, F. Sirotti, F. Teyssandier, G. Chollon, Structure of an Amorphous Boron Carbide Film: An Experimental and Computational Approach, *Chem. Mater.* 25 (2013) 2618–2629. doi:10.1021/cm400847t.
- [2] N. Hong, An Exploration of Neutron Detection in Semiconducting Boron Carbide, University of Nebraska - Lincoln, 2012. <http://digitalcommons.unl.edu/physicsdiss/20>.
- [3] R.B. Billa, Optical Properties of Semiconducting Boron Carbide for Neutron Detection Applications, University of Nebraska - Lincoln, 2009.
- [4] B.J. Nordell, C.L. Keck, T.D. Nguyen, A.N. Caruso, S.S. Purohit, W.A. Lanford, D. Dutta, D. Gidley, P. Henry, S.W. King, M.M. Paquette, Tuning the properties of a complex disordered material: Full factorial investigation of PECVD-grown amorphous hydrogenated boron carbide, *Mater. Chem. Phys.* 173 (2016) 268–284. doi:10.1016/j.matchemphys.2016.02.013.
- [5] G.W. Trucks, K. Raghavachari, G.S. Higashi, Y.J. Chabal, Mechanism of HF etching of silicon surfaces: A theoretical understanding of hydrogen passivation, *Phys. Rev. Lett.* 65 (1990) 504–507. doi:10.1103/PhysRevLett.65.504.
- [6] G. Peterson, Q. Su, Y. Wang, P.A. Dowben, M. Nastasi, Improved p–n heterojunction device performance induced by irradiation in amorphous boron carbide films, *Mater. Sci. Eng. B.* 202 (2015) 25–30. doi:10.1016/j.mseb.2015.09.002.
- [7] C. Lampert, Vacuum Deposition and Coating Options : Products Finishing, *Prod. Finish.* (2013). <http://www.pfonline.com/articles/vacuum-deposition-and-coating-options> (accessed March 14, 2017).
- [8] R.F. Pierret, *Semiconductor Device Fundamentals*, 2nd edition, Addison Wesley, Reading, Mass, 1996.
- [9] A.N. Caruso, R.B. Billa, S. Balaz, J.I. Brand, P.A. Dowben, The heteroisomeric diode, *J. Phys. Condens. Matter.* 16 (2004) L139–L146. doi:10.1088/0953-8984/16/10/L04.
- [10] E. Echeverría, B. Dong, A. Liu, E.R. Wilson, G. Peterson, M. Nastasi, P.A. Dowben, J.A. Kelber, Strong binding at the gold (Au) boron carbide interface, *Surf. Coat. Technol.* (2016). doi:10.1016/j.surfcoat.2016.08.081.
- [11] D.B. Williams, C.B. Carter, *The Transmission Electron Microscope*, in: *Transm. Electron Microsc.*, Springer US, Boston, MA, 2009: pp. 3–22. [http://link.springer.com/10.1007/978-0-387-76501-3\\_1](http://link.springer.com/10.1007/978-0-387-76501-3_1) (accessed December 14, 2016).
- [12] J. Chen, L. Lu, W. Wang, Zn<sub>2</sub>SnO<sub>4</sub> Nanowires as Photoanode for Dye-Sensitized Solar Cells and the Improvement on Open-Circuit Voltage, *J. Phys. Chem. C.* 116 (2012) 10841–10847. doi:10.1021/jp301770n.
- [13] R. Ramanathan, J.L. Campbell, S.K. Soni, S.K. Bhargava, V. Bansal, Cationic Amino Acids Specific Biomimetic Silicification in Ionic Liquid: A Quest to Understand the Formation of 3-D Structures in Diatoms, *PLoS ONE.* 6 (2011). doi:10.1371/journal.pone.0017707.
- [14] E. de Hoffman, V. Stroobant, *Mass Spectrometry Principles and Applications*, Third, Wiley, West Sussex, England, 2007.
- [15] SIMS: introduction to the technique and to the CAMECA SIMS product line, (n.d.). <http://www.cameca.com/instruments-for-research/sims.aspx> (accessed March 15, 2017).

- [16] U. Oran, Surface Chemical Characterization of Plasma-Chemically Deposited Polymer Films, Freien Universitat Berlin, 2005. [http://www.diss.fu-berlin.de/diss/servlets/MCRFileNodeServlet/FUDISS\\_derivate\\_000000001802/](http://www.diss.fu-berlin.de/diss/servlets/MCRFileNodeServlet/FUDISS_derivate_000000001802/) (accessed December 14, 2016).
- [17] O. Legrani, T. Aubert, O. Elmazria, A. Bartasyte, P. Nicolay, A. Talbi, P. Boulet, J. Ghanbaja, D. Mangin, AlN/IDT/AlN/Sapphire SAW Heterostructure for High-Temperature Applications, *IEEE Trans. Ultrason. Ferroelectr. Freq. Control.* 63 (2016) 898–906. doi:10.1109/TUFFC.2016.2547188.
- [18] T.L. Alford, L.C. Feldman, J.W. Mayer, *Fundamentals of Nanoscale Film Analysis*, 2010. <http://www.springer.com/us/book/9780387292601> (accessed March 15, 2017).
- [19] S.M. Sze, K.K. Ng, *Physics of semiconductor devices*, 3rd ed., John Wiley & Sons, Inc., 2006. <http://dx.doi.org/10.1002/9780470068328.ch2>.
- [20] S.S. Li, Bipolar Junction Transistors, in: S.S. Li (Ed.), *Semicond. Phys. Electron.*, Springer New York, 2006: pp. 513–566. [http://link.springer.com/chapter/10.1007/0-387-37766-2\\_14](http://link.springer.com/chapter/10.1007/0-387-37766-2_14) (accessed October 16, 2015).

## **Chapter 3 Improved p-n Heterojunction Device Performance Induced by Irradiation in Amorphous Boron Carbide Films**

### **3.1 Introduction**

This chapter of my dissertation was published in *Materials Science and Engineering: B* in December of 2015 (DOI: 10.1016/j.mseb.2015.09.002), and is reprinted with permission from Elsevier, Copyright (2015). There have been a few minor edits for continuity within this dissertation, such as moving much of the experimental section of the manuscript to Chapter 2 of this dissertation. All TEM sample preparation and measurements were performed by Qing Su of the Nebraska Center for Energy Sciences Research at the University of Nebraska – Lincoln. Qing Su also created Fig. 3.5 overlaying the Vacancy profile and Helium Concentration on the TEM image. Irradiation was performed by Yongqiang Wang with the Materials Science and Technology Division of Los Alamos National Laboratory.

Icosahedral semiconducting boron rich materials have been investigated as a neutron detection medium for decades [1–12]. These materials include icosahedral based boron carbide [13–17], icosahedral based boron nitride [18,19] and icosahedral based boron phosphide [20,21]. What makes them particularly advantageous is their ability to heal neutron [13], electron [17,20], and alpha [22] radiation damage. Although, damage to the cross-linking chains within the unit cell and volumetric swelling from helium bubble formation is known [14–16] with extensive neutron irradiation. As noted in Chapter 1, the  $^{10}\text{B}$  neutron capture process leads to the loss of boron and creation of daughter fragments, including alpha particles with significant kinetic energy. This secondary irradiation as a result of the capture process heightens the importance of starting with a radiation hard material. When the goal is current generation through solid state neutron voltaics, or solid state neutron detection,

maintaining device efficiency with irradiation exposure makes the device much more effective and expands the application possibilities. As noted in Chapter 1, traditional electrical devices such as Schottky barrier diodes [23], and p-n junction diodes [24,25] experience immediate device degradation in radiation harsh environments.

Although there have been many studies of irradiation in boron carbides, none had explored the properties of an electrical device. Most studies were of hot-pressed/sintered or sputtered material. Previous studies are encompassed by Transmission Electron Microscopy (TEM) [26–29], Scanning Electron Microscopy (SEM) [27,30,31], Atomic Force Microscopy (AFM) [32], Raman Spectroscopy [13,28,30,32], Fourier Transform Infrared (FTIR) [29,32], depth profiling (Elastic Recoil Detection Spectroscopy (ERDS)/Rutherford Back Scattering (RBS)) [27,31], X-Ray Reflectivity (XRR) [31], X-Ray Diffraction (XRD) [27,29,31], Secondary Ion Mass Spectroscopy (SIMS) [31], and X-Ray Photoelectron Spectroscopy (XPS) [27,29,31]. There has been a study on the structural properties and radiation hardness of boron carbide when enhanced with Carbon Nano-Tubes (CNT) [28], and there have been numerous studies of medical applications such as Boron Neutron Capture Therapy (BNCT) [29,33]. The BNCT studies examined the physical and chemical properties of nanoparticles, examined the modification of nanoparticles to find T cells through Fluorescence microscopy, and examined neutron radiation shielding [34,35].

Of the studies performed on semiconducting icosahedral based boron carbide that show something other than degradation, there are two important notes. First, the irradiation is electron radiation [20,21] meaning that the incident particle does not produce dense cascades of damage. Electron radiation produces discrete displacements, not cascades. The probability of cascade damage increases with the incident ion mass. Second, the damage/degradation occurs, and then is annealed out

[13]. The vast majority of device designs (voltaics, detectors, scintillators, transistors, etc.) are based on an ordered crystal lattice system that has been modified (such as by interstitial/substitutional doping) to minimize the radiation damage of the device [36]. Even so, the devices still experience immediate degradation, though at differing rates.

### 3.2 Theory and Experiment

The p-n junction diode device explored in this chapter was synthesized following the procedures outlined in Chapter 2 using a substrate of resistivity 1-10  $\Omega \times \text{cm}$ . Following device creation, irradiation was completed at the Center for Integrated Nanotechnologies (CINT), within Los Alamos National Laboratory (LANL) using a 200 kV Danfysik implanter. 200 keV  $\text{He}^+$  ions were implanted to a fluence of  $6.5 \times 10^{16}$  ions/ $\text{cm}^2$ . Air-cooling was applied to ensure that the sample temperature remained below 40 °C during irradiation. One-half of each diode was covered with aluminum foil to maintain a portion of the sample in the virgin state for comparison. Following irradiation, the samples were returned for electrical characterization as outlined in Chapter 2.5.

When an ion enters a material, there are two main means of energy deposition. The first is due to electronic stopping (ionization). In this form of energy deposition, the incident ion represents a sudden perturbation to the system resulting in a transfer of energy from the projectile to the electrons of the target material [37]. The second form of energy deposition is due to energy transfer through the elastic collisions (recoil) between the projectile ion and the atoms of the target material. An ion range of approximately 1400 nm was projected for 200 keV  $\text{He}^+$  ions through application of the *Monte Carlo* SRIM simulation (stopping and range of ions in matter code) [38]. One aliquot fluence above (i.e. of  $6.5 \times 10^{16}$  ions/ $\text{cm}^2$ ) was calculated to result in 0.1 displacements per atom (dpa) in the (a- $\text{B}_{10}\text{C}_{2+x}:\text{H}_y$ ) films studied, as determined from

the SRIM calculated damage events (full cascade mode) and assuming a film atomic density of  $5.0 \times 10^{22}$  atoms/cm<sup>3</sup>. The He<sup>+</sup> ion irradiated fluence to dose (dpa) relationship is linear: 2 times the above fluence yields 0.2 dpa in dose, 5 times the above fluency yields 0.5 dpa in dose, etc.

Fig. 3.1 shows the SRIM simulation of energy deposition in a diode comprised of 285 nm ( $a\text{-B}_{10}\text{C}_{2+x}\text{H}_y$ ) where x is approximately 0 and y is approximately 4 according to elastic recoil detection measurements, and semi-infinite silicon.

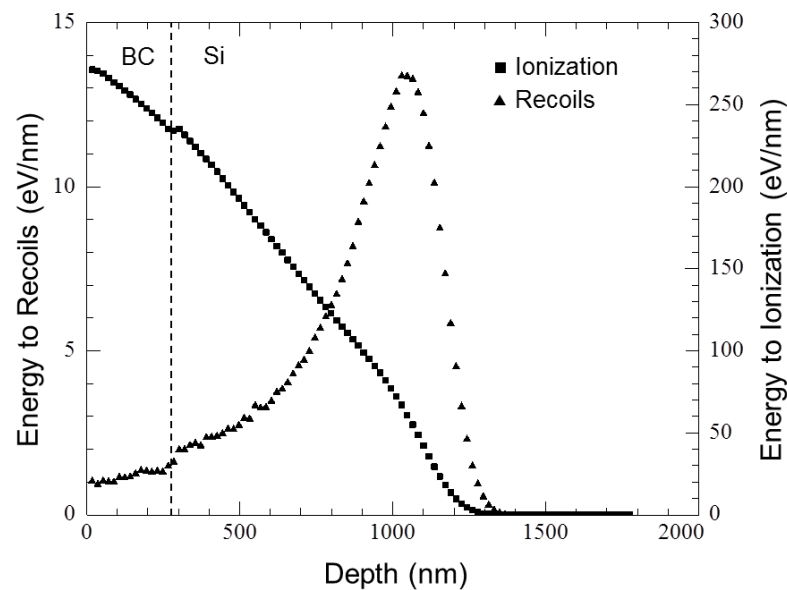


*Fig. 3.1: The SRIM simulation of energy deposition in  $a\text{-B}_{10}\text{C}_{2+x}\text{H}_y$ -Si device separated into its ionization (electronic stopping) and recoil (elastic collisions) components per ion. Please note the change in scale between Recoil and Ionization energy deposition. Ionization energy deposition is more than an order of magnitude greater than Recoil energy deposition, and is the dominant form of energy deposition in the  $a\text{-B}_{10}\text{C}_{2+x}\text{H}_y$  portion of the device.*

This simulation indicates that the energy transferred to the  $a\text{-B}_{10}\text{C}_{2+x}\text{H}_y$  film is dominated by the ionization process, and that within the Si substrate, energy deposition is a function of depth. Note the change in scale of Fig 3.1. The energy deposition due to electronic stopping (Ionization) is more than an order of magnitude greater than that due to elastic collisions (Recoil), ranging from 0 to 280 eV/nm compared to 0 to 14 eV/nm. However, recoils have a higher correlation to

displacement damage. Calculations indicate that a fluence sufficient to create 0.1 dpa in the  $a\text{-B}_{10}\text{C}_{2+x}\text{H}_y$  creates 5.4 dpa at the ion end of range in Si [37].

### 3.3 Results

Current *versus* Voltage  $I(V)$  curves are used as a “Figure of Merit” for traditional p-n junction devices: a measure of how well a device performs. In this research, it is also valid as a Figure of Merit to characterize the device as a neutron voltaic because the current produced by a device from neutron radiation is a function of the charge separation capabilities of the junction. Following neutron capture by a  $^{10}\text{B}$  atom, and fragmentation into the  $^7\text{Li}$  atom and alpha particle ( $\text{He}^+$ ), they create electron-hole pairs as they traverse the film. The ability of the device to separate the pairs to create both an electron current and a hole current will determine how effective the device will operate as a neutron voltaic. Caruso *et al.* showed that when a device cannot effectively separate the charges the device becomes a less effective neutron voltaic (shown in the pulse height spectra) [8].

Fig. 3.2 plots the current *versus* voltage  $I(V)$  curves for selected  $a\text{-B}_{10}\text{C}_{2+x}\text{H}_y/\text{Si}$  p-n heterojunction diodes as a function of irradiation. The solid black triangles ( $\blacktriangle$ ) show the  $I(V)$  response for the virgin  $a\text{-B}_{10}\text{C}_{2+x}\text{H}_y/\text{Si}$  p-n heterojunction diode. Initial  $\text{He}^+$  ion irradiation, equivalent to 0.1 dpa ( $\blacksquare$ ) results in a sharp decrease in the magnitude of the reverse bias current as well as some decrease in the forward bias current. Further  $\text{He}^+$  ion irradiation, to the equivalent of 0.2 dpa ( $\star$ ), results in an additional decrease of forward bias current. Irradiation to the equivalent of 0.5 dpa ( $\bullet$ ) results in a sharp *increase* in the current density surpassing that of the virgin heterojunction diode  $I(V)$  curve under both forward and reverse bias. Further significant increases in the heterojunction diode reverse bias current density is observed with irradiation to the equivalent of 0.8 dpa ( $\triangle$ ).

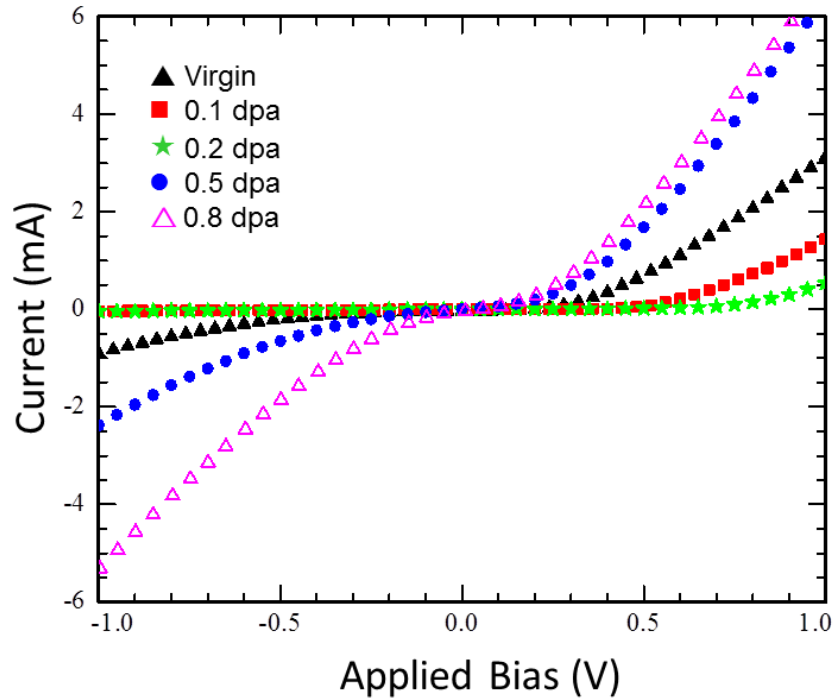


Fig. 3.2: The current versus voltage curves for boron carbide to silicon heterojunction diodes, following different levels of irradiation.

To better quantify any improvements in device performance, as well as device degradation, the differential diode conductance Equation 2-24 (also called the low frequency diode conductance) as a ratio of forward bias to reverse bias [39] in the range from 0.75 to 1.00 V.

Equation 3-1

$$G_d = \frac{dI/dV|_F}{dI/dV|_R}$$

This has been plotted in Figure 3.3. A good figure of merit for a p-n junction is a small leakage current, i.e. very low magnitude reverse bias current density compared to a significant forward bias current density, resulting in a large ratio of differential current with bias. Larger leakage currents resulting in a lower ratio, are indicative of device degradation. The error bars in Fig. 3.3 represent the standard deviation from the mean of the ratio calculated for each level of irradiation.

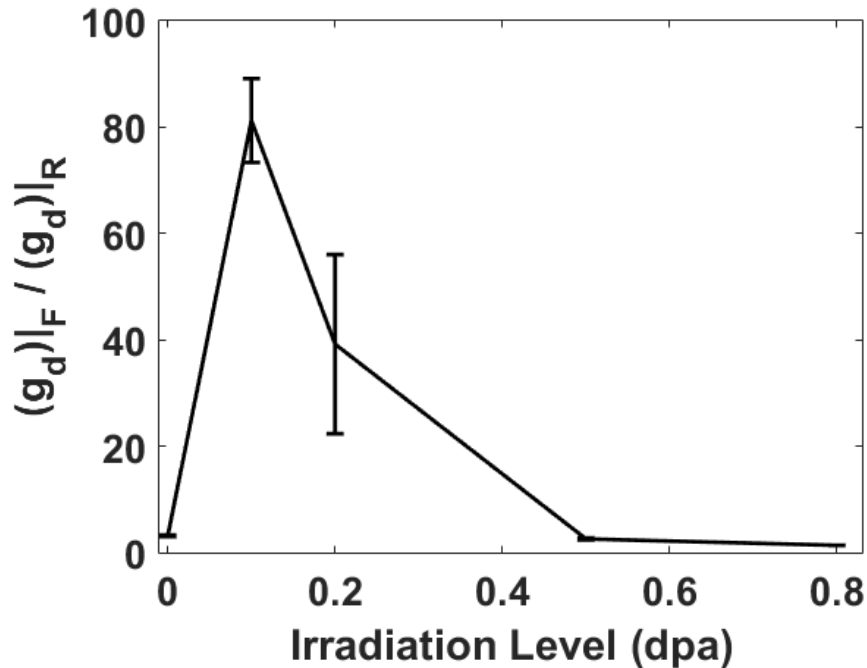
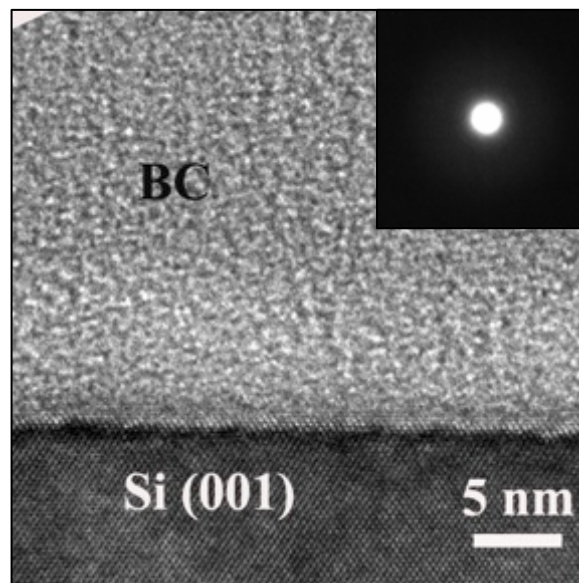


Fig. 3.3: The ratio of the derivative of forward bias current with respect to voltage by the derivative of reverse bias current with respect to voltage derived from the  $I(V)$  data taken between 0.75 and 1.00 applied volts. The higher the ratio, the better the heterojunction diode performance (Figure of Merit). The error bars are the standard deviation of the calculated mean values.

Significant improvement in device performance is seen in the samples with the equivalent of 0.1 and 0.2 dpa. Further irradiation to the equivalent of 0.5 dpa results in degradation of the heterojunction diode Figure of Merit to levels near what was seen for the virgin a-B<sub>10</sub>C<sub>2+x</sub>H<sub>y</sub> to silicon heterojunction diode. With irradiation to the equivalent of 0.8 dpa, the heterostructure begins to resemble a bad resistor.

Transmission electron microscopy (TEM), including high resolution (HRTEM), images were taken to examine the structural changes within the device in an attempt to further understand the source of the changes in the electrical properties of the device. Cross-sectional TEM samples were prepared from the virgin, 0.2 dpa, 0.4 dpa, and 0.6 dpa equivalent He<sup>+</sup> ion irradiated a-B<sub>10</sub>C<sub>2+x</sub>H<sub>y</sub> to silicon heterojunction specimens. All cross-section TEM samples were prepared from a-B<sub>10</sub>C<sub>2+x</sub>H<sub>y</sub> films using standard gluing, mechanical grinding and polishing procedures, followed by a low energy (3.7 keV) ion milling. Images were acquired

with an FEI Tecnai Osiris (S)TEM electron microscope. Fig. 3.4 shows the HRTEM image of the  $a\text{-B}_{10}\text{C}_{2+x}\text{H}_y/\text{Si}$  interface after  $\text{He}^+$  ion irradiation equivalent to 0.6 dpa, with an inset of the selected area electron diffraction (SAED) pattern of the  $a\text{-B}_{10}\text{C}_{2+x}\text{H}_y$  film. The image and SAED clearly show that the  $a\text{-B}_{10}\text{C}_{2+x}\text{H}_y$  film remains amorphous, and just as clearly shows that the Si near the interface remains crystalline. However, it should be noted that this image would not indicate the presence or absence of point defects in the Si. Fig. 3.4 does show that the metallurgical junction (the physical interface between the p-type material and n-type material) remains abrupt and well defined. Fig. 3.4 indicates that changes in device performance may not be dictated by structural changes in the  $a\text{-B}_{10}\text{C}_{2+x}\text{H}_y$  films or at the p-n heterojunction interface, rather damage to the silicon, not the boron carbide, is implicated as the cause of device degradation.



*Fig. 3.4: The HRTEM image of  $a\text{-B}_{10}\text{C}_{2+x}\text{H}_y$  film-Si(001) interface after irradiation (0.6 dpa equivalent) and shows that the Si substrate remains crystalline near the interface and the  $a\text{-B}_{10}\text{C}_{2+x}\text{H}_y$  film – Si(001) junction interface remains abrupt. The insert is a selected area electron diffraction pattern (SAED) of the boron carbide film, showing the boron carbide remains amorphous.*

The TEM cross-section image of the  $a\text{-B}_{10}\text{C}_{2+x}\text{H}_y$  film and the silicon substrate, to a significant depth, is shown in Fig. 3.5. The image shows the device, after irradiation equivalent to 0.6 dpa in the boron carbide film, from the outer edge of

the  $a\text{-B}_{10}\text{C}_{2+x}\text{H}_y$  film to the undamaged quasi-neutral silicon region. Overlaid on the image of Fig. 3.5 is the void distribution (solid red line), and the helium concentration as determined by SRIM. The irradiated Si has three discernable regions. Region (a) is the area near the interface with  $a\text{-B}_{10}\text{C}_{2+x}\text{H}_y$  film. Near the junction, the Si appears to remain crystalline, and point defects remain isolated from each other. Region (b) exhibits signatures of point defect agglomeration: these are the dark areas adjacent to bright(er) areas in this TEM image. The larger dark areas are attributed to a large concentration of vacancies, while the bright area is attributed to self-interstitials [40]. The vertically oriented white striations, or platelets, of region (c) are indicative of He bubbles. To the right of region (c) is the undamaged bulk Si. The black lines represent bend contours, most likely the result of the TEM sample preparation, although sample swelling due to helium deposition is not unknown [14–17]. Stress/strain fields from such swelling could also yield similar TEM features. Fig. 3.5 clearly shows a direct correlation between the void distribution profile and the damage to the Si substrate, as well as a direct correlation between He bubbles of region (c) and the peak of the He distribution profile. Such helium bubble formation is not seen in boron carbides until extremely high fluences are reached corresponding to more than 1 dpa [14–17], well outside the range of this work. The point defect agglomeration and He bubbles also give a visual indication that di-vacancy states ( $V_2$ ) formed by the combination of vacancies created in close proximity to each other, and other vacancy complexes, are the result of the structural change in the Si substrate. Changes in the device behavior are not related to structural changes in the boron carbide film or at the p-n heterojunction interface. This becomes important in our following discussion of heterojunction leakage currents under reverse bias.

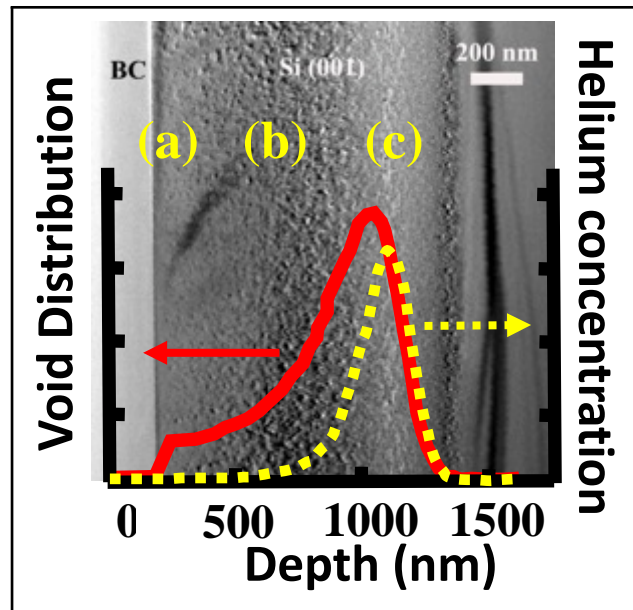


Fig. 3.5: The TEM image of an  $a\text{-B}_{10}\text{C}_{2+x}\text{H}_y$  to Si heterojunction after irradiation equivalent to 0.6 dpa in the boron carbide film. The red line represents vacancies introduced into the silicon, and the dashed yellow line represents the helium concentration in the silicon substrate. Region (a) is a crystalline region near the metallurgical junction. Region (b) displays signatures of point defect agglomeration. Region (c) is the ion end of range with the highest concentration of He deposition. To the right of (c) is undamaged Si.

### 3.4 Discussion

The improvement seen for  $a\text{-B}_{10}\text{C}_{2+x}\text{H}_y$  to silicon heterojunction diode devices, with small amounts of irradiation is very likely occurring in an environment where competing phenomena are in play. We propose that the improvements seen here are a combination of the electronic stopping energy deposited in the  $a\text{-B}_{10}\text{C}_{2+x}\text{H}_y$  film by the alpha particle, breaking strained bonds which reform in lower energy states, or resolving distorted icosahedron cages resultant from mono-anion or di-anion states [41]. Both events may reduce the number of defects in the film, although a direct confirmation for this has not been ascertained from work reported here and remains an open speculation until definitely resolved in future work.

According to Gill *et al.* [42], the reverse bias leakage current density ( $J_v$ ) arises from a carrier emission/generation process. Any capture reactions are minimized due to the reduction in the carrier concentration under reverse bias. The

rate of generation ( $G$ ) is proportional to the trap concentration ( $N_t$ ) and electron and hole capture cross-sections ( $\sigma$ ).

Equation 3-2

$$J_v = e G$$

Equation 3-3

$$G = \frac{N_t \sigma v n_i}{2 \cosh(\beta)}$$

Equation 3-4

$$\beta = \frac{E_t - E_i}{kT}$$

Where  $v$  is the thermal carrier velocity,  $n_i$  is the intrinsic carrier concentration,  $E_t$  is the trap energy level,  $E_i$  is the intrinsic Fermi level,  $k$  is the Boltzmann Constant, and  $T$  is temperature.

As mentioned above, Fig. 3.5 provides visual evidence that there should be an anisotropic distribution of trap energy states available for carrier generation as well as a distribution in the concentration of those states. This means that the total generation reverse bias leakage current density will be a summation of the components resultant from each discrete trap level.

Equation 3-5

$$G_{tot} = \sum G_i$$

The energy levels of di-vacancy states in Si devices have been reported by MacEvoy *et al.* [43] as  $E_c - 0.23$  eV,  $E_c - 0.42$  eV,  $E_v + 0.25$  eV. MacEvoy *et al.* [43] has also reported several other complexes created under neutron radiation. Such complexes within the host semiconductor could be important to the current density due to carrier generation in reverse bias, but will not be discussed in depth in this research. Instead, we note that one expects a proportionality of  $N_t$  to the reverse bias current density.

Furthermore, the introduction rate of  $N_t$  for a given discrete trap level is, in turn, proportional to the irradiation level.

Fig. 3.6 indicates that two major changes in the reverse bias leakage current of the a-B<sub>10</sub>C<sub>2+x</sub>H<sub>y</sub> to Si p-n heterojunctions occurs with increasing He<sup>+</sup> ion irradiation. Among these changes, surprisingly, the data suggests an initial reduction in the concentration of traps with discrete energy levels, especially with increasing He<sup>+</sup> ion irradiation near a fluence of 0.1 dpa equivalent irradiation level. Since the Si substrate is single crystal, the amorphous film is the most logical medium to account for the reduction in the concentration of traps with discrete energy levels. The reduction in trap concentration reduces the number of acceptors in the film, increases the effective carrier lifetime, with the experimental observation that the series resistance of the film decreases by over half (175 Ω to 62 Ω). Additionally, it is possible that the decrease in trap concentration for a discrete level(s) is such that the effective distribution of trap states is reduced: i.e. some  $G_i \rightarrow 0$ . The contribution to the current density of such a  $G_i$  is so small as to be completely dominated by the other discrete trap state components, noted in Equation 3-5. The reverse bias currents are seen to be  $\propto N_t \propto dpa$  only at large irradiation fluences. This shows that the trap concentrations likely decrease due to modification of the a-B<sub>10</sub>C<sub>2+x</sub>H<sub>y</sub> film via electronic energy deposition, and then increase due to damage accumulation in the Si by nuclear energy deposition.

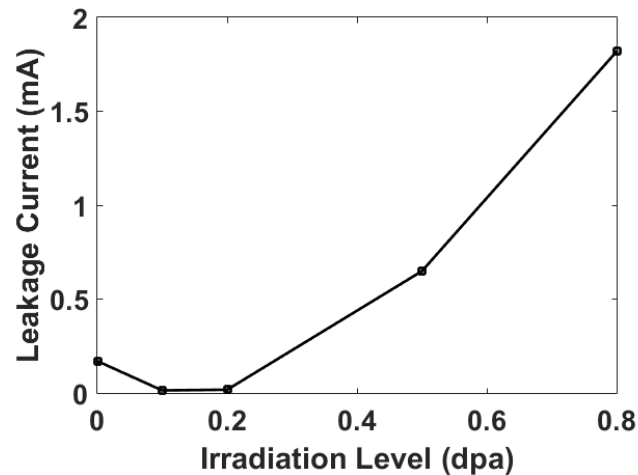


Fig. 3.6: The reverse bias leakage current (-0.5 volts) versus irradiation level.

For increasing  $\text{He}^+$  ion irradiation beyond a 0.1 dpa to 0.2 dpa equivalent, as calculated for the  $\text{a-B}_{10}\text{C}_{2+x}\text{H}_y$  film, the damage in the Si begins to degrade the device as fast as the changes in the  $\text{a-B}_{10}\text{C}_{2+x}\text{H}_y$  film improves it, and a decrease in device performance is indicated by Fig. 3.3. It is expected that the energy trap levels of the Si will be of different complexes and concentrations than the  $\text{a-B}_{10}\text{C}_{2+x}\text{H}_y$  films. This creates new, additional  $G_i$  components, increasing the generation current density, though at this point, the concentration of traps is still low enough to be dominated by other radiation induced discrete trap state components, as noted in Equation 3-5.

For irradiation equivalent to 0.5 dpa and 0.8 dpa, device behavior is dominated by the changes in the Si. It is well understood that radiation damage significantly reduces charge carrier lifetimes in silicon [20,44]. It is also known that bulk radiation damage has a significant effect on charge carrier concentration profiles in silicon [42,45–50], resulting in carrier inversion of n-type silicon to p-type silicon. For light particles (pions, protons, and neutrons), the inversion point occurs at a particle fluence between  $10^{13}$  and  $10^{14} \text{ cm}^{-2}$ . The initial particle fluence of this study is three orders of magnitude greater than this. If true, this will change the initial charge distribution of the device, creating an exponentially graded decrease in n-type carrier concentration

moving from the device interface to ion end of range, as well as creating scattering centers which reduce carrier lifetime. After which the carrier concentration returns to equilibrium levels in the undamaged area. The calculated edge of the depletion region in the virgin Si (with an applied bias of 0.4 volts) is 610 nm [51], just inside of the highest recoil damage region. As point defects accumulate in the Si, the depletion region extends outward exponentially, following the change in carrier concentration grading. While this cannot be confirmed from the data presented here, it is suspected that the n-type silicon near ion end of range type inverts between 0.2 dpa and 0.5 dpa, creating a graded homojunction that is now in series with the heterojunction. If accurate, this creates an electrostatically coupled p-p+ heterojunction / p+-n graded homojunction (grading referring to carrier concentration not metallurgical grading), with a large reverse bias generation current for the reasons discussed previously.

If the electronic energy deposition is breaking bonds, and allowing them to reform in a lower energy state, it is important to perform a cursory thermodynamic examination to determine if the energy deposition per atom is of sufficient magnitude to encourage this. The SRIM simulation of Fig. 3.1 predicts that the majority of the energy deposition in the  $a\text{-B}_{10}\text{C}_{2+x}\text{H}_y$  film will be electronic, and of a magnitude around 270 eV/nm per ion, or at a fluence of  $6.5 \times 10^{16}$  ions/cm<sup>2</sup> which is equivalent to 0.1 dpa, 3510 eV/atom in electronic energy deposition. According to Glockler [52] and Feng *et al.* [53], the B-B bonds within an icosahedron have an energy range of 1.3 to 2.6 eV/atom, and B-H bonds an energy range of 1.73 to 3.04 eV/atom. The heat of formation for ortho-carborane is -1.82 eV/atom [41]. Therefore, the electronic energy deposition, within the  $a\text{-B}_{10}\text{C}_{2+x}\text{H}_y$  film is more than enough, within the ion track and secondary ion tracks (delta-ray tracks) [54], to break bonds, and re-form them, reducing  $N_t$  of Equation 3-3 as discussed, and as demonstrated for isolated *closo-*

carborane icosahedra [53]. The bond energy of Si-Si is 2.25 eV/atom [55], so both electronic and recoil energy deposition in the Si have enough energy to create defects, and increase  $N_t$ , nearly right up to the end of the ion deposition range.

### 3.5 Conclusions

In conclusion, a-B<sub>10</sub>C<sub>2+x</sub>H<sub>y</sub> on Si p-n heterojunctions, synthesized utilizing PECVD, show a robust insensitivity to radiation damage. These heterojunction devices were irradiated with 200 keV He<sup>+</sup> ions to examine the effects of radiation on the electrical properties of the devices. For low doses of radiation, unlike most other solid state electrical devices, the heterojunction diode performance improved, as illustrated by the ratio of forward bias current to reverse bias or leakage current. A possible origin for the device performance, with modest irradiation, may be due to an initial passivation of defects in the a-B<sub>10</sub>C<sub>2+x</sub>H<sub>y</sub> films. Such defect passivation could result from electronic energy deposition, bond breakings and re-formation of the local bonds with a lower total free energy, possibly resolving distorted icosahedron anion states. As observed by SAED, this is not a re-crystallization process, but an easing of strain/stress fields.

With sufficient 200 keV He<sup>+</sup> ion irradiation of the a-B<sub>10</sub>C<sub>2+x</sub>H<sub>y</sub> to silicon heterojunction devices, we find significant device degradation. It is the fragility of the crystalline Si that causes device degradation and failure as opposed to any interaction of the He<sup>+</sup> with the a-B<sub>10</sub>C<sub>2+x</sub>H<sub>y</sub> films. Devices fabricated solely from boron carbide [2,6–8], might prove to be even more insensitive to irradiation, until sufficient helium accumulates to create voids and bubbles [14–16] (representing charge carrier barriers), or the damage is significant enough to destroy the interface junction, preventing charge separation.

### 3.6 References

- [1] A.N. Caruso, The physics of solid-state neutron detector materials and geometries, *J. Phys. Condens. Matter.* 22 (2010) 443201. doi:10.1088/0953-8984/22/44/443201.
- [2] A.N. Caruso, R.B. Billa, S. Balaz, J.I. Brand, P.A. Dowben, The heteroisomeric diode, *J. Phys. Condens. Matter.* 16 (2004) L139–L146. doi:10.1088/0953-8984/16/10/L04.
- [3] B.W. Robertson, S. Adenwalla, A. Harken, P. Welsch, J.I. Brand, P. Dowben, J.P. Claassen, A class of boron-rich solid-state neutron detectors, *Appl. Phys. Lett.* 80 (2002) 1344–3646.
- [4] B.W. Robertson, S. Adenwalla, A. Harken, P. Welsch, J.I. Brand, J.P. Claassen, N.M. Boag, P.A. Dowben, Semiconducting boron-rich neutron detectors, in: *Proc SPIE*, 2002: pp. 226–233. doi:10.1117/12.453923.
- [5] S. Adenwalla, R. Billa, J.I. Brand, E. Day, M.J. Diaz, A. Harken, A. McMullen-Gunn, R. Padmanabhan, B.W. Robertson, Semiconducting boron-rich neutron detectors, in: *Proc SPIE*, 2004: pp. 70–74. doi:10.1117/12.506646.
- [6] K. Osberg, N. Schemm, S. Balkir, J.I. Brand, S. Hallbeck, P.A. Dowben, A hand-held neutron detection sensor system, in: *Peter Dowben Publ.*, 2006: p. 4 pp. doi:10.1109/ISCAS.2006.1692801.
- [7] K. Osberg, N. Schemm, S. Balkir, J.I. Brand, M.S. Hallbeck, P.A. Dowben, M.W. Hoffman, A Handheld Neutron-Detection Sensor System Utilizing a New Class of Boron Carbide Diode, *IEEE Sens. J.* 6 (2006) 1531–1538. doi:10.1109/JSEN.2006.883905.

- [8] A.N. Caruso, P.A. Dowben, S. Balkir, N. Schemm, K. Osberg, R.W. Fairchild, O.B. Flores, S. Balaz, A.D. Harken, B.W. Robertson, J.I. Brand, The all boron carbide diode neutron detector: Comparison with theory, *Mater. Sci. Eng. B.* 135 (2006) 129–133. doi:10.1016/j.mseb.2006.08.049.
- [9] E. Day, M.J. Diaz, S. Adenwalla, Effect of bias on neutron detection in thin semiconducting boron carbide films, *J. Phys. Appl. Phys.* 39 (2006) 2920. doi:10.1088/0022-3727/39/14/007.
- [10] N. Hong, J. Mullins, K. Foreman, S. Adenwalla, Boron carbide based solid state neutron detectors: the effects of bias and time constant on detection efficiency, *J. Phys. Appl. Phys.* 43 (2010) 275101. doi:10.1088/0022-3727/43/27/275101.
- [11] N. Hong, L. Crow, S. Adenwalla, Time-of-flight neutron detection using PECVD grown boron carbide diode detector, *Nucl. Instrum. Methods Phys. Res. Sect. Accel. Spectrometers Detect. Assoc. Equip.* 708 (2013) 19–23. doi:10.1016/j.nima.2012.12.105.
- [12] E. Echeverría, R. James, U. Chiluwal, F.L. Pasquale, J.A.C. Santana, R. Gapfizi, J.-D. Tae, M.S. Driver, A. Enders, J.A. Kelber, P.A. Dowben, Novel semiconducting boron carbide/pyridine polymers for neutron detection at zero bias, *Appl. Phys. A.* 118 (2014) 113–118. doi:10.1007/s00339-014-8778-4.
- [13] D. Simeone, C. Mallet, P. Dubuisson, G. Baldinozzi, C. Gervais, J. Maquet, Study of boron carbide evolution under neutron irradiation by Raman spectroscopy, *J. Nucl. Mater.* 277 (2000) 1–10. doi:10.1016/S0022-3115(99)00149-X.
- [14] A. Jostsons, C.K.H. DuBose, G.L. Copeland, J.O. Stiegler, Defect structure of neutron irradiated boron carbide, *J. Nucl. Mater.* 49 (1973) 136–150. doi:10.1016/0022-3115(73)90003-2.

- [15] G.W. Hollenberg, B. Mastel, J.A. Basmajian, Effect of Irradiation Temperature on the Growth of Helium Bubbles in Boron Carbide, *J. Am. Ceram. Soc.* 63 (1980) 376–380. doi:10.1111/j.1151-2916.1980.tb10195.x.
- [16] G.W. Hollenberg, W.V. Cummings, Effect of Fast Neutron Irradiation on the Structure of Boron Carbide, *J. Am. Ceram. Soc.* 60 (1977) 520–525. doi:10.1111/j.1151-2916.1977.tb14097.x.
- [17] T. Stoto, N. Housseau, L. Zuppiroli, B. Kryger, Swelling and microcracking of boron carbide subjected to fast neutron irradiations, *J. Appl. Phys.* 68 (1990) 3198–3206. doi:10.1063/1.346370.
- [18] I. Caretti, I. Jiménez, Point defects in hexagonal BN, BC<sub>3</sub> and BC<sub>x</sub>N compounds studied by x-ray absorption near-edge structure, *J. Appl. Phys.* 110 (2011) 23511. doi:10.1063/1.3602996.
- [19] A. Enyashin, A. Ivanovskii, Structural, elastic, and electronic properties of icosahedral boron subcarbides (BC<sub>3</sub>, BC<sub>2</sub>), subnitride BN, and suboxide BO from data of SCC-DFTB calculations, *Phys. Solid State.* 53 (2011) 1569–1574. doi:10.1134/S1063783411080117.
- [20] D. Emin, Unusual properties of icosahedral boron-rich solids, *J. Solid State Chem.* 179 (2006) 2791–2798. doi:10.1016/j.jssc.2006.01.014.
- [21] M. Carrard, D. Emin, L. Zuppiroli, Defect clustering and self-healing of electron-irradiated boron-rich solids, *Phys. Rev. B.* 51 (1995) 11270–11274. doi:10.1103/PhysRevB.51.11270.
- [22] G. Peterson, Q. Su, Y. Wang, P.A. Dowben, M. Nastasi, Improved p–n heterojunction device performance induced by irradiation in amorphous boron carbide films, *Mater. Sci. Eng. B.* 202 (2015) 25–30. doi:10.1016/j.mseb.2015.09.002.

- [23] S. Almaziva, M. Angelone, M. Marinelli, E. Milani, M. Pillon, G. Prestopino, A. Tucciarone, C. Verona, G. Verona-Rinati, Characterization of damage induced by heavy neutron irradiation on multilayered  ${}^6\text{LiF}$ -single crystal chemical vapor deposition diamond detectors, *J. Appl. Phys.* 106 (2009) 73501.  
doi:10.1063/1.3224869.
- [24] M. Caussanel, A. Canals, S.K. Dixit, M.J. Beck, A.D. Touboul, R.D. Schrimpf, D.M. Fleetwood, S.T. Pantelides, Doping-Type Dependence of Damage in Silicon Diodes Exposed to X-Ray, Proton, and  $\text{He}^+$  Irradiations, *IEEE Trans. Nucl. Sci.* 54 (2007) 1925–1930. doi:10.1109/TNS.2007.909021.
- [25] H. Ohyama, K. Hayama, T. Hakata, E. Simoen, C. Claeys, J. Poortmans, M. Caymax, Y. Takami, H. Sunaga, Impact of high energy particle irradiation on the electrical performance of  $\text{Si}_{1-x}\text{Ge}_x$  epitaxial diodes, *J. Mater. Sci. Mater. Electron.* 10 (1999) 335–337.
- [26] T. Maruyama, M. Iwanami, S. Ohnuki, T. Suda, S. Watanabe, K. Ikezawa, Precipitation and Amorphization in Boron Carbide Irradiated by High Energy Helium Ions, in: M. Grossbeck, T. Allen, R. Lott, A. Kumar (Eds.), *Eff. Radiat. Mater. 21st Int. Symp.*, ASTM International, 100 Barr Harbor Drive, PO Box C700, West Conshohocken, PA 19428-2959, 2004: pp. 670-670–10.  
<http://www.astm.org/doiLink.cgi?STP11265S> (accessed July 30, 2015).
- [27] C. Höglund, K. Zeitelhack, P. Kudejova, J. Jensen, G. Greczynski, J. Lu, L. Hultman, J. Birch, R. Hall-Wilton, Stability of  $10\text{B}4\text{C}$  thin films under neutron radiation, *Radiat. Phys. Chem.* 113 (2015) 14–19.  
doi:10.1016/j.radphyschem.2015.04.006.

- [28] A. Aitkaliyeva, M.C. McCarthy, H.-K. Jeong, L. Shao, Irradiation studies on carbon nanotube-reinforced boron carbide, *Nucl. Instrum. Methods Phys. Res. Sect. B Beam Interact. Mater. At.* 272 (2012) 249–252.  
doi:10.1016/j.nimb.2011.01.076.
- [29] M.W. Mortensen, P.G. Sørensen, O. Björkdahl, M.R. Jensen, H.J.G. Gundersen, T. Bjørnholm, Preparation and characterization of Boron carbide nanoparticles for use as a novel agent in T cell-guided boron neutron capture therapy, *Appl. Radiat. Isot. Data Instrum. Methods Use Agric. Ind. Med.* 64 (2006) 315–324.  
doi:10.1016/j.apradiso.2005.08.003.
- [30] G. Victor, Y. Pison, N. Béreard, N. Toulhoat, N. Moncoffre, N. Djourelou, S. Miro, J. Baillet, N. Pradeilles, O. Rapaud, A. Maître, D. Gosset, Structural modifications induced by ion irradiation and temperature in boron carbide B<sub>4</sub>C, *Nucl. Instrum. Methods Phys. Res. Sect. B Beam Interact. Mater. At.* (n.d.).  
doi:10.1016/j.nimb.2015.07.082.
- [31] G. Nowak, M. Störmer, H.-W. Becker, C. Horstmann, R. Kampmann, D. Höche, M. Haese-Seiller, J.-F. Moulin, M. Pomm, C. Randau, U. Lorenz, R. Hall-Wilton, M. Müller, A. Schreyer, Boron carbide coatings for neutron detection probed by x-rays, ions, and neutrons to determine thin film quality, *J. Appl. Phys.* 117 (2015) 34901. doi:10.1063/1.4905716.
- [32] B. Todorović-Marković, I. Draganić, D. Vasiljević-Radović, N. Romčević, M. Romčević, M. Dramićanin, Z. Marković, Synthesis of amorphous boron carbide by single and multiple charged boron ions bombardment of fullerene thin films, *Appl. Surf. Sci.* 253 (2007) 4029–4035. doi:10.1016/j.apsusc.2006.08.035.

- [33] K.J. Riley, P.J. Binns, S.J. Ali, O.K. Harling, The design, construction and performance of a variable collimator for epithermal neutron capture therapy beams, *Phys. Med. Biol.* 49 (2004) 2015–2028.
- [34] R.G. Abrefah, R.B.M. Sogbadji, E. Ampomah-Amoako, S.A. Birikorang, H.C. Odoi, B.J.B. Nyarko, Design of boron carbide-shielded irradiation channel of the outer irradiation channel of the Ghana Research Reactor-1 using MCNP, *Appl. Radiat. Isot. Data Instrum. Methods Use Agric. Ind. Med.* 69 (2011) 85–89. doi:10.1016/j.apradiso.2010.06.024.
- [35] J. Ghassoun, N. Senhou, The evaluation of neutron and gamma ray dose equivalent distributions in patients and the effectiveness of shield materials for high energy photons radiotherapy facilities, *Appl. Radiat. Isot. Data Instrum. Methods Use Agric. Ind. Med.* 70 (2012) 620–624. doi:10.1016/j.apradiso.2011.12.041.
- [36] M. McPherson, T. Sloan, B.K. Jones, Suppression of irradiation effects in gold-doped silicon detectors, *J. Phys. Appl. Phys.* 30 (1997) 3028–3035. doi:10.1088/0022-3727/30/21/018.
- [37] M. Nastasi, J.W. Mayer, *Ion Implantation and Synthesis of Materials*, Springer, 2006. <http://www.springer.com/physics/particle+and+nuclear+physics/book/978-3-540-23674-0> (accessed February 5, 2015).
- [38] J.P. Biersack, L.G. Haggmark, A Monte Carlo computer program for the transport of energetic ions in amorphous targets, *Nucl. Instrum. Methods.* 174 (1980) 257–269. doi:10.1016/0029-554X(80)90440-1.
- [39] D.K. Schroder, *Semiconductor Material and Device Characterization*, 3rd ed., John Wiley & Sons, Inc., Hoboken, New Jersey, 2006.

- [40] N. Stoddard, G. Duscher, W. Windl, G. Rozgonyi, A new understanding of near-threshold damage for 200 keV irradiation in silicon, *J. Mater. Sci.* 40 (2005) 3639–3650. doi:10.1007/s10853-005-1059-z.
- [41] K. Hermansson, M. Wójcik, S. Sjöberg, *o*- , *m*- , and *p* -Carboranes and Their Anions: Ab Initio Calculations of Structures, Electron Affinities, and Acidities <sup>†</sup>, *Inorg. Chem.* 38 (1999) 6039–6048. doi:10.1021/ic9903811.
- [42] K. Gill, G. Hall, B. MacEvoy, Bulk damage effects in irradiated silicon detectors due to clustered divacancies, *J. Appl. Phys.* 82 (1997) 126–136. doi:10.1063/1.365790.
- [43] B.C. MacEvoy, G. Hall, K. Gill, Defect evolution in irradiated silicon detector material, *Nucl. Instrum. Methods Phys. Res. Sect. Accel. Spectrometers Detect. Assoc. Equip.* 374 (1996) 12–26. doi:10.1016/0168-9002(96)37410-X.
- [44] P. Hazdra, V. Komarnitsky, Local lifetime control in silicon power diode by ion irradiation: introduction and stability of shallow donors, *IET Circuits Devices Syst.* 1 (2007) 321. doi:10.1049/iet-cds:20070013.
- [45] K. Gill, G. Hall, S. Roe, S. Sotthibandhu, R. Wheadon, P. Giubellino, L. Ramello, Radiation damage by neutrons and protons to silicon detectors, *Nucl. Instrum. Methods Phys. Res. Sect. Accel. Spectrometers Detect. Assoc. Equip.* 322 (1992) 177–188. doi:10.1016/0168-9002(92)90027-2.
- [46] E. Fretwurst, H. Feick, M. Glaser, C. Gößling, E.H.M. Jeijne, A. Hess, Reverse annealing of the effective impurity concentration and long-term operational scenario for silicon detectors in future collider experiments, *Nucl. Instrum. Methods Phys. Res. Sect. Accel. Spectrometers Detect. Assoc. Equip.* (1994). doi:10.1016/0168-9002(94)91417-6.

- [47] D. Pitzl, N. Cartiglia, B. Hubbard, D. Hutchinson, J. Leslie, K. O'Shaughnessy, W. Rowe, H.F.-W. Sadrozinski, A. Seiden, E. Spencer, H.J. Ziock, P. Ferguson, K. Holzscheiter, W.F. Sommer, Type inversion in silicon detectors, *Nucl. Instrum. Methods Phys. Res. Sect. Accel. Spectrometers Detect. Assoc. Equip.* 311 (1992) 98–104. doi:10.1016/0168-9002(92)90854-W.
- [48] P.A. Aarnio, M. Huhtinen, M. Pimiä, K. Kaita, M. Laakso, A. Numminen, P. Ryytty, Damage observed in silicon diodes after low energy pion irradiation, *Nucl. Instrum. Methods Phys. Res. Sect. Accel. Spectrometers Detect. Assoc. Equip.* 360 (1995) 521–531. doi:10.1016/0168-9002(95)00008-9.
- [49] S.J. Bates, C. Furetta, M. Glaser, F. Lemeilleur, E. León-Florián, C. Gößling, B. Kaiser, A. Rolf, R. Wunstorf, H. Feick, E. Fretwurst, G. Lindström, M. Moll, G. Taylor, A. Chilingarov, Pion-induced damage in silicon detectors, *Nucl. Instrum. Methods Phys. Res. Sect. Accel. Spectrometers Detect. Assoc. Equip.* 379 (1996) 116–123. doi:10.1016/0168-9002(96)00538-4.
- [50] K. Riechmann, K.T. Knöpfle, V.M. Pugatch, Pion and proton induced radiation damage to silicon detectors, *Nucl. Instrum. Methods Phys. Res. Sect. Accel. Spectrometers Detect. Assoc. Equip.* 377 (1996) 276–283. doi:10.1016/0168-9002(95)01408-X.
- [51] R.F. Pierret, *Semiconductor Device Fundamentals*, 2nd edition, Addison Wesley, Reading, Mass, 1996.
- [52] G. Glockler, Bond energies and bond distances of boron hydrides, *Trans Faraday Soc.* 59 (1963) 1080–1085.

- [53] D. Feng, J. Liu, A.P. Hitchcock, A.L.D. Kilcoyne, T. Tyliczszak, N.F. Riehs, E. Rühl, J.D. Bozek, D. McIlroy, P.A. Dowben, Photofragmentation of closo-Carboranes Part 1: Energetics of Decomposition, *J. Phys. Chem. A.* 112 (2008) 3311–3318. doi:10.1021/jp711019q.
- [54] T.A. Tombrello, Distribution of damage along an MeV ion Track, *Nucl. Instrum. Methods Phys. Res. B.* 83 (1993) 508–512.
- [55] R.F. Stewart, M.A. Whitehead, G. Donnay, The ionicity of the Si-O bond in low-quartz, *Am. Mineral.* 65 (1980) 324–326.

## Chapter 4 Charge Carrier Lifetime

### 4.1 Introduction

This chapter is a combination of the papers *Semiconducting boron carbides with better charge extraction through the addition of pyridine moieties* published in the Journal of Physics D: Applied Physics in September 2016 (DOI: 10.1088/0022-3727/49/35/355302), reprinted with permission, copyright (2016) IOP Publishing Ltd. and *Increased drift carrier lifetime in semiconducting boron carbides deposited by plasma enhanced chemical vapor deposition from carboranes and benzene* published in the Journal of Vacuum Science & Technology A: Vacuum, Surfaces, and Films in December 2016 (DOI: 10.1116/1.4973338), reprinted with permission, Copyright (2016), American Vacuum Society. They have been combined and modified to highlight my contributions to the papers, and exclude much of the work that was performed by others. The p-n heterojunction devices with the aromatic additions of pyridine and benzene were synthesized under the supervision of Jeffrey Kelber, and work performed by Bin Dong and Joseph Silva of the Department of Chemistry at the University of North Texas. For those samples, metallization was performed by Elena Echeverria, and electrical measurements ( $I(V)$  and  $C(V)$ ) were performed by Ethiyal Wilson both of the Department of Physics and Astronomy at the University of Nebraska – Lincoln.

Although there are many advantages to working with the boron-rich icosahedral semiconductors, as discussed at the beginning of chapter 3, there are a number of disadvantages as well. The main causes for poor neutron detection performance includes an insufficiently thick depletion region within the device, the need for a thicker device to come closer to neutron opacity [2], and the need for better charge

collection while maintaining low reverse bias leakage currents. Limits in current rectification efficiency result in a constant power drain through the device due to high defect concentrations [3] and low carrier mobilities [4]. Although exceptionally high mobilities have been sometimes claimed [5], such claims have not been attributed to PECVD deposited semiconducting boron carbide. With the interconnection between mobility and lifetime, this chapter examines the effects of changes in charge carrier lifetime on device performance. This examination is accomplished through the combination of data from the current *versus* voltage measurements outlined in chapter 3 and capacitance *versus* voltage measurements.

While PECVD boron carbides synthesized from ortho-carborane are generally p-type, PECVD semiconducting boron carbide synthesized from meta-carborane is unusual in that it is an n-type semiconductor material [6–8]. An examination of the charge carrier lifetime of material synthesized from both ortho-carborane and meta-carborane has been performed. Further, after an initial study indicated that the addition of pyridine ( $C_5H_5N$ ), an aromatic linking chain, substantially enhanced charge carrier lifetime [9] of material synthesized from ortho-carborane, the study was expanded to include benzene ( $C_6H_6$ ), another aromatic, as well.

## 4.2 Experimental Details

Device synthesis for research in this set of experiments follows the same path as that outlined in Chapter 3.2 with the exception of silicon substrate selection. As meta-carborane forms an n-type semiconductor material, a p-type silicon substrate was required for the formation of a p-n junction based device. Additionally, in an attempt to shorten the depletion region of the boron carbide film a more resistive silicon was chosen ( $100 \Omega \times \text{cm}$ ) to reduce the carrier concentration that must be accounted for in the boron carbide film to achieve equilibrium. The process for

PECVD synthesized  $a\text{-B}_{10}\text{C}_{2+x}\text{H}_y$  films on silicon wafers creating a p-n heterojunction have been described in previous work [9,1,10,11]. The ortho-carborane based material with and without benzene were grown on n-type silicon ( $100\ \Omega\times\text{cm}$ ) while the meta-carborane based material, with and without benzene, were grown on p-type silicon ( $100\ \Omega\times\text{cm}$ ).

1.89 mm diameter gold (Au) contacts were deposited by thermal evaporation to allow for electrical measurements as described in Chapters 2.5 and 2.6. As a check of the lifetime measurements here, the carrier lifetime in a commercial silicon epitaxial planar diode (Vishay Semiconductors) was ascertained from the  $I(V)$  and  $C(V)$  measurements. The estimated hole carrier lifetime of  $2\times 10^{-8}$  s corresponds to a donor density of about  $2\times 10^{19}\ \text{cm}^{-3}$  and this is in agreement with the specifications from supplier, Desert Silicon.

### 4.3 Results and Discussion

#### A. Heterojunction Capacitance vs Voltage

The charge carrier lifetimes can be extracted from the p-n junction diode utilizing the current versus voltage  $I(V)$  and capacitance  $C(V)$  curves using some modest assumptions. Such data is readily obtained given the robust facility for fabrication of successful PECVD semiconducting hydrogenated boron carbide composite films [10,12–17]. The  $I(V)$  curves for p-n heterojunction diodes synthesized via PECVD utilizing ortho-carborane as the source molecule of the films both with and without the addition of pyridine moieties, i.e. ( $\text{B}_{10}\text{C}_{2+x}\text{H}_y\text{:Py/Si}$ ;  $\text{B}_{10}\text{C}_{2+x}\text{H}_y\text{:Si}$ ), are shown in Fig. 4.1 (voltage sweeping from positive to negative).

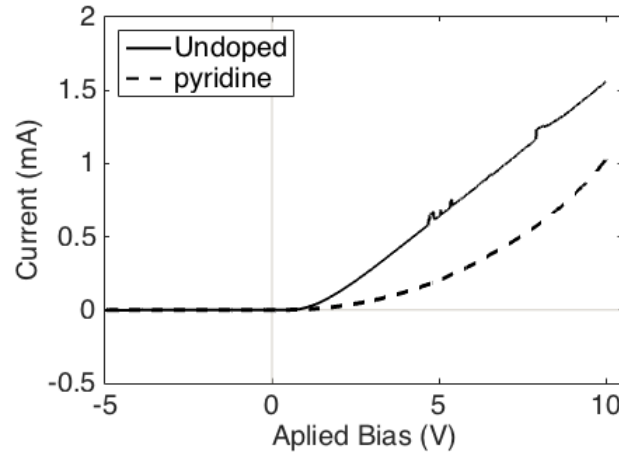


Fig. 4.1: The current versus voltage curves for PECVD synthesized *p-n* heterojunction diodes synthesized from ortho-carborane on silicon comparing the undoped ( $a\text{-B}_{10}\text{C}_{2+x}\text{H}_y/\text{Si}$ ) device to a pyridine/ortho-carborane composite (3:1 ratio) film ( $a\text{-B}_{10}\text{C}_{2+x}\text{H}_y\text{:Py}/\text{Si}$ ).

The series resistance  $R_s$  is related to the capacitance [18]:

Equation 4-1

$$R_s = \left( \frac{1}{\omega C_j} \right) \sqrt{\frac{C_j}{C_p} - 1}$$

where  $\omega$  is the angular frequency ( $\omega = 2\pi f$ ),  $f$  is the frequency of the small signal perturbation across the device under test,  $C_j$  is the junction capacitance,  $C_p$  is the parallel capacitance (measured capacitance in a parallel circuit). Therefore, although the data in Fig. 4.1 indicate a higher total resistance for the PECVD ortho-carborane boron carbide film diodes without pyridine, the lower  $R_s$  of the PECVD pyridine/ortho-carborane composite film on silicon diode is evident in Fig. 4.1 from the more pronounced exponential form, following the ideal diode equation (Equation 2-10) [19], and shown again below for convenience:

$$I = I_0 \left( e^{qV_A/kT} - 1 \right)$$

where  $I_0$  is the saturation current,  $q$  is the elemental charge,  $V_A$  is the applied voltage,  $k$  is the Boltzmann constant, and  $T$  is the temperature (in Kelvin). The PECVD

pyridine/ortho-carborane composite film sample also does not exhibit signs of breakdown within the measured voltage range.

Fig. 4.2 shows the typical  $I(V)$  curves for the p- and n-type  $a\text{-B}_{10}\text{C}_{2+x}\text{H}_y$  heterostructures with and without benzene doping (voltage sweeping from positive to negative). Just as with pyridine doping in Fig. 4.1, the p-n heterostructures retain their current rectification property in reverse bias with benzene doping, indicating that all devices (in both Fig. 4.1 and 4.2) remain p-n heterojunctions. It is also observed that the benzene doping does not significantly affect the turn-on voltage of the meta-carborane devices. We do note that the rectification is better with the n-type boron carbide heterojunction (meta-carborane) than the p-type boron carbide (ortho-carborane) heterojunction, but the turn-on voltage is far greater with the n-type boron carbide (Figs. 4.2(c) and 4.2(d)) than in the p-type boron carbide heterojunction. Neither benzene nor pyridine doping altered the general electronic structure of either the ortho-carborane or meta-carborane based device: current rectification properties are retained, and the turn-on voltage is not significantly altered.

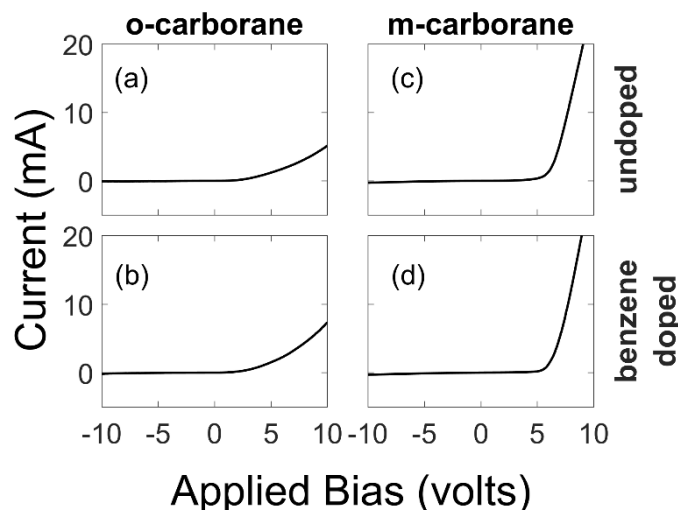


Fig. 4.2:  $I(V)$  curves comparing  $a\text{-B}_{10}\text{C}_{2+x}\text{H}_y/\text{Si}$  heterojunction devices based on (a) ortho-carborane (undoped), (b) ortho-carborane (doped with benzene), (c) meta-carborane (undoped), (d) meta-carborane (doped with benzene).

Of greater significance, the measurements shown in Fig. 4.1 and 4.2 are used in determining the low frequency conductance of the devices ( $G_0$ ) and in calculating the diffusion capacitance ( $C_D$ ), as outlined in Chapter 2.6 and prior work [1,20].

As noted in Chapters 2.6 and 3.2, by definition, the low frequency conductance is given by Equation 2-24 (shown below as a reminder).

$$G_0 = \frac{dI}{dV_a}$$

$G_0$  is the slope of the  $I(V)$  curve at the d.c. operating point (i.e.  $f \rightarrow 0$  Hz). The low frequency conductance ( $G_0$ ) is dependent on the carrier lifetimes, depletion width of the diode junction, built-in voltage, doping profile, and carrier concentration. It should be emphasized however, that regardless of the junction type or dominant current component,  $G_0 = dI/dV_a$  can always be applied to the measured  $I(V)$  data in order to determine  $G_0$  [19], and that has been done in this instance. The purpose of the examination of  $G_0$  becomes immediately apparent in the analysis of the capacitance data.

The low frequency conductance ( $G_0$ ) of both diodes from Fig. 4.1 have been plotted in Fig. 4.3. It is immediately evident that the measurement for the ortho-carborane film, without pyridine, is much noisier than the pyridine/ortho-carborane composite film on silicon device. There is also a much greater initial increase in the current for equivalent applied voltages in the ortho-carborane film (pyridine-free) on silicon diode. Near 2.5 applied volts, however, the change in current with increasing voltage flattens, and becomes linear for the ortho-carborane film (pyridine-free) on silicon diode. A linear  $G_0$  is what one would expect from a resistor. In contrast, the pyridine/ortho-carborane composite film on silicon diode exhibits an exponential increase in current when responding to increased

applied voltage. This is expected since the derivative of an exponential function (Eq. (4.1)) is still an exponential function.

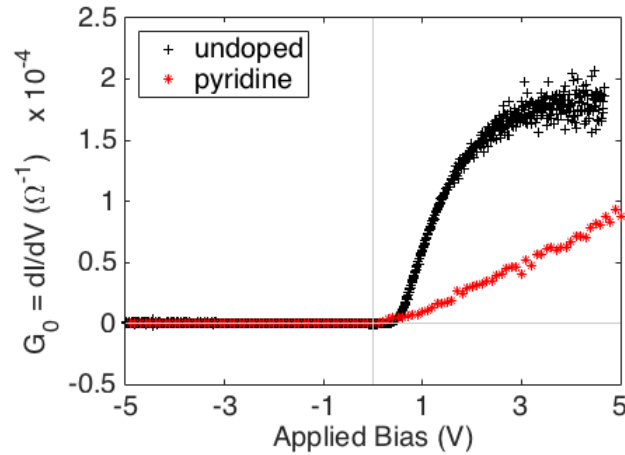


Fig. 4.3: Low frequency conductance of the PECVD synthesized pyridine/ortho-carborane composite film on silicon device (pyridine doped) and PECVD ortho-carborane film on silicon device (undoped) heterojunctions calculated from the  $I(V)$  data of Fig. 4.1.

Though not shown here, the low frequency conductance was also calculated for the data shown in Fig. 4.2 as it is required in the charge carrier lifetime modeling. Calculation of  $G_0$  shown in Fig. 4.3 is accomplished utilizing Equation 4-2. From Equation 4-2, we see that  $G_0$  may be directly calculated from the measured d.c.  $I(V)$  values of Fig. 4.1 and 4.2 by numeric differentiation.

The capacitance associated with oscillations in the depletion width due to small sinusoidal perturbations is referred to as the junction capacitance ( $C_J$ ). If there are no other charge oscillations, the device capacitance, independent of frequency, is equal to  $C_J$  in reverse bias (depletion conditions) [21]. Chapter 2.6 provides a good discussion on this topic, however, Equation 2-20 is the equation for a homojunction diode. This data examines a heterojunction diode, and therefore  $C_J$  is given by:

Equation 4-2

$$C_J = \left( \frac{qN_{D1}N_{A2}\epsilon_1\epsilon_2}{2(\epsilon_1N_{D1} + \epsilon_2N_{A2})(V_{bi} - V_A)} \right)^{\frac{1}{2}}$$

where  $q$  is the elemental charge,  $N_{D1}$  is the number of donor atoms/cm<sup>3</sup> in the n-type material,  $N_{A2}$  is the number of acceptor atoms/cm<sup>3</sup> in the p-type material,  $\epsilon_1$  is the dielectric constant of the n-type material,  $\epsilon_2$  is the dielectric constant of the p-type material,  $V_{bi}$  is the built in voltage due to both materials ( $V_{bi} = V_{bi1} + V_{bi2}$ ), and  $V_A$  is the applied voltage.

Since the junction capacitance is associated with reverse bias conditions, the minority carrier concentration near the edge of the depletion region is very small compared to that of the majority carriers, and thus can be neglected. Under forward bias conditions, this is not a valid assumption. There is a significant contribution by the minority carriers to the changes in charge due to the sinusoidal perturbation signal. This contribution to the device capacitance is referred to as the diode diffusion capacitance ( $C_D$ ), and is given by Equation 2-23 (shown below as a reminder):

$$C_D = \frac{G_0}{\omega\sqrt{2}} \left( \sqrt{1 + \omega^2\tau^2} - 1 \right)^{\frac{1}{2}}$$

where  $G_0$  is the low frequency conductance previously defined and shown in Fig. 4.3,  $\omega$  is again the angular frequency ( $2\pi f$ ), and  $\tau$  is the effective carrier lifetime. There are many and various contributions to the capacitances, and many types of defects, but if we restrict our modeling efforts to the diffusion component of transport, Equation 2-23 can be used to model the data relative to the baseline capacitance as in Fig. 4.4. The  $C(V)$  curves of the ortho-carborane boron carbide film, without pyridine, in a heterojunction diode on n-type silicon (i.e.  $B_{10}C_{2+x}H_y/Si$ ) (a) and pyridine/ortho-carborane composite films on n-type silicon ( $B_{10}C_{2+x}H_y:Py/Si$ ) (b), are compared in Fig. 4.4. The first distinction between the PECVD synthesized semiconducting partially dehydrogenated boron carbide without pyridine ( $B_{10}C_{2+x}H_y/Si$ ) and PECVD synthesized semiconducting partially dehydrogenated boron carbide composite films with pyridine moieties ( $B_{10}C_{2+x}H_y:Py/Si$ ) is the

difference in the reverse bias capacitance values. If the measured capacitance ( $C$ )  $\rightarrow C_j$  as discussed above, there should not be a frequency dependent component. The pyridine/ortho-carborane composite film on n-type silicon,  $B_{10}C_{2+x}H_y:Py/Si$ , heterojunction diode exhibits this behavior, but the data for  $B_{10}C_{2+x}H_y/Si$  diode does have a frequency-dependent component to it, meaning that there is another capacitive component present in reverse bias other than  $C_j$ . This could be an interfacial capacitance, or related to the defect density distribution of the film. The capacitance does decrease with increasing frequency, however, indicating that there is some type of charge carrier that can no longer respond to the perturbation signal as the frequency increases [20,22,23].

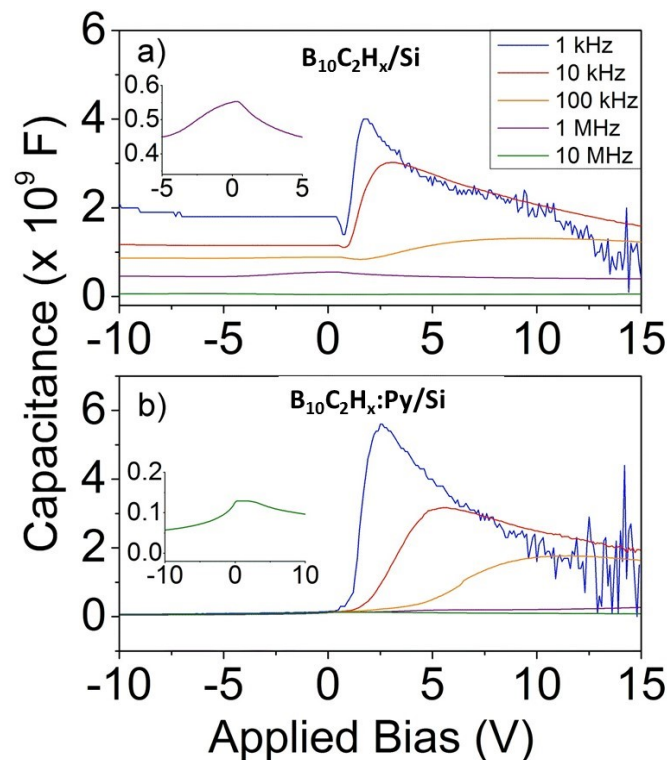


*Fig. 4.4: The capacitance versus voltage curves of (a) the ortho-carborane boron carbide films, without pyridine, on silicon ( $B_{10}C_{2+x}H_y/Si$ ) and (b) the co-deposited pyridine and ortho-carborane boron carbide films on silicon,  $B_{10}C_{2+x}H_y:Py/Si$ , as a function of frequency, are compared. The insets are of high frequency data on an expanded capacitance scale.*

The peak capacitance values of the co-deposited pyridine and ortho-carborane boron carbide films on silicon,  $B_{10}C_{2+x}H_y:Py/Si$ , diodes are slightly larger than those of the ortho-carborane boron carbide films on silicon,  $B_{10}C_{2+x}H_y/Si$ , heterojunction

diodes. There is also a shift of the peak capacitance toward positive bias in the PECVD co-deposited pyridine and ortho-carborane boron carbide films on silicon,  $B_{10}C_{2+x}H_y:Py/Si$ , diodes, which is attributed to a decrease in the  $R_s$  of the pyridine containing co-deposited pyridine and ortho-carborane boron carbide films on silicon. With the higher  $R_s$ , exhibited by the pyridine-free ortho-carborane boron carbide film, there is an associated voltage drop across the junction, which will reduce the applied voltage, as shown in Equation 2-12 (shown below as a reminder).

$$V_J = V_A - IR_s$$

(where  $V_J$  is the junction voltage,  $V_A$  is the applied voltage,  $I$  is the current, and  $R_s$  is the series resistance) shifting the signal toward zero, as observed.

The  $C(V)$  curves, at frequencies from 10 kHz to 10 MHz, of the n-type boron carbide heterojunction (from the PECVD of meta-carborane), and the p-type boron carbide heterojunction (from the PECVD of ortho-carborane), with benzene included as one of the source compounds for the semiconducting boron carbide, has been plotted in Fig. 4.5. Again, as with the discussion leading to Fig. 4.4, any deviation from the measured capacitance in reverse bias from a single constant value indicates that there is another frequency dependent capacitive component present. Fig. 4.5(a) shows that this frequency dependent capacitive component also disappears with benzene doping (i.e., the reverse bias capacitance is constant for all frequencies measured). The n-type semiconducting boron carbide heterojunction with p-type silicon, from the PECVD of meta-carborane doped with benzene, retains a frequency dependent capacitive component, as seen in Fig. 4.5(b) (i.e. reverse bias capacitance is not constant for all frequencies measured). While there is no experimental identification of this reverse bias frequency dependent  $C(V)$  component, possible contributions could come from interfacial capacitance, or related to the defect density

distribution of the film [9]. Regardless, the reduction of the reverse bias capacitance dependence, with frequency, indicates that there is some type of charge carrier that can no longer respond to the perturbation signal as the frequency increases [20,22,23].

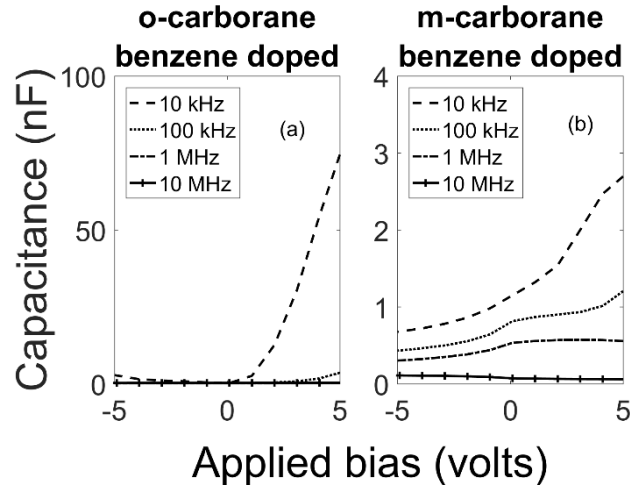


Fig. 4.5:  $C(V)$  curves comparing  $a\text{-}B_{10}C_{2+x}H_y/Si$  heterojunction devices as a function of applied perturbation frequency. The heterojunction device in (a) is based on ortho-carborane co-deposited with benzene and the device in (b) is based on meta-carborane co-deposited with benzene. (a) shows that benzene doping eliminates reverse bias capacitive components that are present in the ortho-carborane (undoped) based device shown in Fig. 4.4. (b) shows that a reverse bias frequency dependent capacitive component is still present (i.e. it is not constant with changing frequency).

## B. The Drift Carrier Lifetimes

While there are many and various contributions to capacitances, and many types of defects, we restrict our modeling efforts to the diffusion component of charge transport, Equation 2-23, relative to the baseline capacitance in Fig. 4.5. Modeling of diffusion capacitance in Fig. 4.6 and 4.7 were accomplished utilizing Equation 2-23 and 2-24. From Equation 2-24,  $G_0$  may be directly calculated from the measured d.c.  $I(V)$  values of Fig. 4.1 and 4.2 by numeric differentiation. We calculate values of the frequency dependent diffusion capacitance, for set values of frequency, and carrier lifetime  $\tau$  as a function of  $G_0$ , according to Equation 2-23. Exploiting the determination of  $G_0$ , and given that  $f$ , the driving frequency, is set by the experiment, this leaves  $\tau$  as the only unknown variable. An iterative process, with differing  $\tau$  values, is used to generate increasingly better fits to the data. This is then used to

generate diffusion capacitance values and finally plotted, with the experimental applied voltage(s) as the independent variable. The lifetime  $\tau$  controls the height and slope of the modeled  $C_D$ , so the fitting of Equation 2-23 to the measured  $C(V)$  data yields a drift carrier lifetime.

We find good agreement between the measured  $C(V)$  data and our model diffusion capacitance ( $\bullet$ ) in the region of small forward bias, i.e. the accumulation region, as expected, and as seen in Fig. 4.6 and 4.7. Curve fitting Equation 2-23 to the measured  $C(V)$  data in Fig 4.4 and 4.5, taken at 10 kHz yielding a best fit of the measured data, for the carrier lifetime was found to be 350  $\mu$ s in the pyridine/ortho-carborane boron carbide films on silicon,  $B_{10}C_{2+x}H_y:Py/Si$ , heterojunction diode, and 35  $\mu$ s in the ortho-carborane boron carbide film on silicon,  $B_{10}C_{2+x}H_y/Si$ , heterojunction diode.

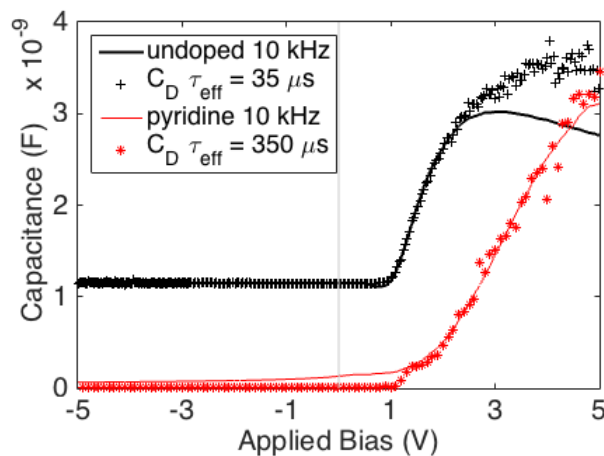


Fig. 4.6: Model of diffusion capacitance overlaid on  $C(V)$  data at 10 kHz: undoped data (solid black line) and pyridine doped data (solid red line). The undoped calculated  $C_D$  (+) indicates an effective carrier lifetime of 35  $\mu$ s. The pyridine doped calculated  $C_D$  (\*) indicates an effective carrier lifetime of 350  $\mu$ s.

The PECVD p-type semiconducting boron carbide heterojunctions, from ortho-carborane with benzene is found, to have a drift carrier lifetime of 2.5 msec, and is shown in Fig. 4.7(a). This is far larger than the drift carrier lifetime of roughly 35  $\mu$ sec found for the corresponding p-type boron carbide without benzene shown in Fig.

4.6. For the n-type semiconducting boron carbide heterojunctions from meta-carborane with benzene, the drift carrier lifetime, shown in Fig. 4.7(b), is found to be 300 nsec. This is considerably smaller than the values seen for the p-type boron carbides with and without benzene, but much larger than the drift carrier lifetime of 50 nsec seen for this n-type boron carbide without benzene inclusions [24]. While there appears to be more deviation from the measured capacitance in Fig. 4.7(b), the absolute magnitude of the deviation has a much narrower range in Fig. 4.7(b), than in Fig. 4.7(a), (approximately 1 nF versus 10 nF at 3 volts).

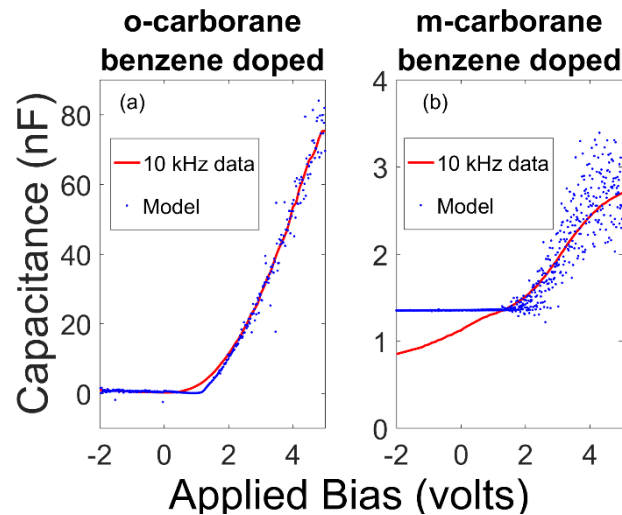


Fig. 4.7: Modeled diffusion capacitance ( $C_D$ ) ( $\bullet$ ) overlaid on  $C(V)$  data measured (solid lines) at 10 kHz for (a) ortho-carborane co-deposited with benzene, and (b) meta-carborane co-deposited with benzene. The calculated  $C_D$  indicates a drift carrier lifetime in (a) of approximately 2.5 msec, (b) of approximately 300 nsec. Please note the change in scale between the figures. Although the variation in  $C_D$  appears larger in (b), it is actually significantly narrower than (a).

As noted above, the pyridine/ortho-carborane boron carbide films on silicon,  $B_{10}C_{2+x}H_y:Py/Si$ , heterojunction diode has only has 1 frequency dependent capacitance component, the diffusion capacitance. The ortho-carborane boron carbide film on silicon,  $B_{10}C_{2+x}H_y/Si$ , heterojunction diode has two distinct frequency dependent capacitance components. The first is the diffusion capacitance, common to both types of heterojunction diode. The second component, however, indicates that the PECVD boron carbide films, without pyridine, also have defect states that respond to the small signal perturbation, consistent with the large Urbach tail discussed

elsewhere [25]. As the period of the perturbation approaches the lifetime of the carriers due to the defect state, the defects can no longer respond to the perturbation, and no longer contribute to the capacitance of the diode. Traps result in contributions to capacitor charging current, but since their time constants are relatively long, the effects of the traps are absent, or greatly reduced, with high frequency perturbations.

If there is a distribution of trap states inside of the band gap of the PECVD ortho-carborane film, without pyridine moieties, as the perturbation frequency is increased, there should be a corresponding decrease in the device capacitance. This is exactly what is observed in Fig. 4.4 and 4.5 and explains the leaky nature of the  $I(V)$  curve of Fig.4.1, for the ortho-carborane boron carbide films (without pyridine) on silicon,  $B_{10}C_{2+x}H_y/Si$ , heterojunction diode. This indicates that the addition of pyridine to the PECVD synthesized semiconducting partially dehydrogenated boron carbide is eliminating key trap states within the device.

Further evidence for this hypothesis is found in Fig. 4.6, with the increase in the effective carrier lifetime from 35  $\mu s$  for the ortho-carborane boron carbide film on silicon,  $B_{10}C_{2+x}H_y/Si$ , heterojunction diode to 350  $\mu s$  for the pyridine/ortho-carborane boron carbide films on silicon,  $B_{10}C_{2+x}H_y:Py/Si$ , heterojunction diode. One might expect that with the addition of pyridine-like moieties, there would be additional scattering centers, leading to a shorter lifetime. Just the opposite is observed. One possible explanation is the reduction in the trap concentration, as put forth above. A 350  $\mu s$  carrier lifetime is similar to that reported in diamond like carbon (DLC) films (0.3 ms surface, 0.11 ms bulk) [26], and much longer than the carrier lifetimes for a-Si:H films ( $\sim 0.1 \mu s$ ) [27]. Our carrier lifetimes for the pyridine/ortho-carborane boron carbide films, however, are in rough agreement with the findings of Bao *et al.* [28] for sputter-deposited boron carbide films quite different for those reported here,

indicating carrier lifetimes of 0.91 to 0.98 ms. A likely distinction between the Bao *et al.* boron carbide films [28] and the films of this study is the presence of hydrogen in the PECVD boron carbide films.

#### 4.4 Summary and Conclusions

The drift carrier lifetimes for semiconducting boron carbide, from PECVD synthesized semiconducting partially dehydrogenated boron carbide from 1,2 dicarbadodecaborane, 1,2-B<sub>10</sub>C<sub>2</sub>H<sub>12</sub> (ortho-carborane) and 1,7 dicarbadodecaborane, 1,7-B<sub>10</sub>C<sub>2</sub>H<sub>12</sub> (meta-carborane), with benzene or pyridine included are compared to drift carrier lifetimes in both the p-type PECVD synthesized partially dehydrogenated semiconducting boron carbide fabricated from ortho-carborane and the n-type semiconducting partially dehydrogenated boron carbide made from meta-carborane. The benzene doping of the p-type semiconducting partially dehydrogenated boron carbide (ortho-carborane) increases the drift carrier lifetime by 2 orders of magnitude (7043 % increase), while the benzene doping of the n-type semiconducting partially dehydrogenated boron carbide (meta-carborane) increases the drift carrier lifetime 6 fold (500 % increase). The addition of pyridine to the p-type (PECVD) semiconducting boron carbide (ortho-carborane) increases the drift carrier lifetime by an order of magnitude (900 % increase).

It has been shown that disordered systems, like the organic photovoltaics (OPV), have an inverse proportionality between mobility and charge carrier lifetime [29], contrary to traditional ordered semiconductor systems (i.e. Si, GaAs, Ge), where the mobility and charge carrier lifetimes are directly proportional [19]. The reason behind the inverse proportionality of disordered systems is due to bi-molecular recombination (direct radiative charge cancellation due to an electron encountering a hole). Such a scenario would limit the improvements to device performance but the

improved charge collection, reported with the addition of pyridine [9], suggest improvements are possible, and that aromatic additions seem to be promising. As the mobility increases, the probability of an electron encountering a hole increases, reducing the drift carrier lifetime. Though, to date, no studies on mobility have been conducted on pyridine or benzene doped  $a\text{-B}_{10}\text{C}_{2+x}\text{H}_y$  synthesized by PECVD. The disordered nature of  $a\text{-B}_{10}\text{C}_{2+x}\text{H}_y$  films allows for parallels to be drawn to the OPV research.

#### 4.5 References

- [1] A.N. Caruso, The physics of solid-state neutron detector materials and geometries, *J. Phys. Condens. Matter.* 22 (2010) 443201. doi:10.1088/0953-8984/22/44/443201.
- [2] M.M. Abdul-Gader, U.A. Al-Binni, A.A. Ahmad, M.A. Al-Basha, N.J. Ianno, Low-field current transport mechanisms in rf magnetron sputter deposited boron carbide (B<sub>5</sub>C)/p-type crystalline silicon junctions in the dark, *Int. J. Electron.* 88 (2001) 873–901.
- [3] B.J. Nordell, C.L. Keck, T.D. Nguyen, A.N. Caruso, S.S. Purohit, W.A. Lanford, D. Dutta, D. Gidley, P. Henry, S.W. King, M.M. Paquette, Tuning the properties of a complex disordered material: Full factorial investigation of PECVD-grown amorphous hydrogenated boron carbide, *Mater. Chem. Phys.* 173 (2016) 268–284. doi:10.1016/j.matchemphys.2016.02.013.
- [4] H. Werheit, A. Moldenhauer, On the Diffusion of Free Carriers in  $\beta$ -Rhombohedral Boron, *J. Solid State Chem.* 179 (2006). doi:10.1016/j.jssc.2005.11.039.
- [5] A.N. Caruso, R.B. Billa, S. Balaz, J.I. Brand, P.A. Dowben, The heteroisomeric diode, *J. Phys. Condens. Matter.* 16 (2004) L139–L146. doi:10.1088/0953-8984/16/10/L04.
- [6] A.N. Caruso, P.A. Dowben, S. Balkir, N. Schemm, K. Osberg, R.W. Fairchild, O.B. Flores, S. Balaz, A.D. Harken, B.W. Robertson, J.I. Brand, The all boron carbide diode neutron detector: Comparison with theory, *Mater. Sci. Eng. B.* 135 (2006) 129–133. doi:10.1016/j.mseb.2006.08.049.

- [7] A.N. Caruso, S. Balaz, B. Xu, P.A. Dowben, A.S. McMullen-Gunn, J.I. Brand, Y.B. Losovyj, D.N. McIlroy, Surface photovoltage effects on the isomeric semiconductors of boron-carbide, *Appl. Phys. Lett.* 84 (2004) 1302–1304. doi:10.1063/1.1648136.
- [8] E. Echeverria, B. Dong, G. Peterson, J.P. Silva, E.R. Wilson, M.S. Driver, Y.-S. Jun, G.D. Stucky, S. Knight, T. Hofmann, Z.-K. Han, N. Shao, Y. Gao, W.-N. Mei, M. Nastasi, P.A. Dowben, J.A. Kelber, Semiconducting boron carbides with better charge extraction through the addition of pyridine moieties, *J. Phys. Appl. Phys.* 49 (2016) 355302–355312. doi:10.1088/0022-3727/49/35/355302.
- [9] G.G. Peterson, E. Echeverria, B. Dong, J.P. Silva, E.R. Wilson, J.A. Kelber, M. Nastasi, P.A. Dowben, Increased drift carrier lifetime in semiconducting boron carbides deposited by plasma enhanced chemical vapor deposition from carboranes and benzene, *J. Vac. Sci. Technol. Vac. Surf. Films.* 35 (2016) 03E101. doi:10.1116/1.4973338.
- [10] E. Echeverría, R. James, F.L. Pasquale, J.A.C. Santana, M.S. Driver, A. Enders, J.A. Kelber, P.A. Dowben, Neutron Detection Signatures at Zero Bias in Novel Semiconducting Boron Carbide/Pyridine Polymers, *MRS Online Proc. Libr. Arch.* 1743 (2015). doi:10.1557/opl.2015.352.
- [11] B. Dong, R. James, J.A. Kelber, PECVD of boron carbide/aromatic composite films: Precursor stability and resonance stabilization energy, *Surf. Coat. Technol.* 290 (2016) 94–99. doi:10.1016/j.surfcoat.2015.09.042.
- [12] B.W. Robertson, S. Adenwalla, A. Harken, P. Welsch, J.I. Brand, P. Dowben, J.P. Claassen, A class of boron-rich solid-state neutron detectors, *Appl. Phys. Lett.* 80 (2002) 1344–3646.

- [13] B.W. Robertson, S. Adenwalla, A. Harken, P. Welsch, J.I. Brand, J.P. Claassen, N.M. Boag, P.A. Dowben, Semiconducting boron-rich neutron detectors, in: Proc SPIE, 2002: pp. 226–233. doi:10.1117/12.453923.
- [14] E. Day, M.J. Diaz, S. Adenwalla, Effect of bias on neutron detection in thin semiconducting boron carbide films, *J. Phys. Appl. Phys.* 39 (2006) 2920. doi:10.1088/0022-3727/39/14/007.
- [15] N. Hong, J. Mullins, K. Foreman, S. Adenwalla, Boron carbide based solid state neutron detectors: the effects of bias and time constant on detection efficiency, *J. Phys. Appl. Phys.* 43 (2010) 275101. doi:10.1088/0022-3727/43/27/275101.
- [16] N. Hong, L. Crow, S. Adenwalla, Time-of-flight neutron detection using PECVD grown boron carbide diode detector, *Nucl. Instrum. Methods Phys. Res. Sect. Accel. Spectrometers Detect. Assoc. Equip.* 708 (2013) 19–23. doi:10.1016/j.nima.2012.12.105.
- [17] E. Echeverría, R. James, U. Chaluwal, F.L. Pasquale, J.A.C. Santana, R. Gapfizi, J.-D. Tae, M.S. Driver, A. Enders, J.A. Kelber, P.A. Dowben, Novel semiconducting boron carbide/pyridine polymers for neutron detection at zero bias, *Appl. Phys. A.* 118 (2014) 113–118. doi:10.1007/s00339-014-8778-4.
- [18] D.K. Schroder, *Semiconductor Material and Device Characterization*, 3rd ed., John Wiley & Sons, Inc., Hoboken, New Jersey, 2006.
- [19] R.F. Pierret, *Semiconductor Device Fundamentals*, 2nd edition, Addison Wesley, Reading, Mass, 1996.
- [20] E.H. Nicollian, A. Goetzberger, The Si-SiO<sub>2</sub> Interface—Electrical Properties as Determined by the Metal-Insulator-Silicon Conductance Technique, *Bell Syst. Tech. J.* 46 (1967) 1055–1133.

- [21] S.S. Li, p-n Junction Diodes, in: S.S. Li (Ed.), *Semicond. Phys. Electron.*, Springer New York, 2006: pp. 334–380.  
[http://link.springer.com/chapter/10.1007/0-387-37766-2\\_11](http://link.springer.com/chapter/10.1007/0-387-37766-2_11) (accessed October 16, 2015).
- [22] E.H. Nicollian, J.R. Brews, *MOS (metal oxide semiconductor) physics and technology*, Wiley, 1982.
- [23] S.M. Sze, K.K. Ng, *Physics of semiconductor devices*, 3rd ed., John Wiley & Sons, Inc., 2006. <http://dx.doi.org/10.1002/9780470068328.ch2>.
- [24] E. Echeverría, B. Dong, A. Liu, E.R. Wilson, G. Peterson, M. Nastasi, P.A. Dowben, J.A. Kelber, Strong binding at the gold (Au) boron carbide interface, *Surf. Coat. Technol.* (2016). doi:10.1016/j.surfcoat.2016.08.081.
- [25] B.J. Nordell, S. Karki, T.D. Nguyen, P. Rulis, A.N. Caruso, S.S. Purohit, H. Li, S.W. King, D. Dutta, D. Gidley, W.A. Lanford, M.M. Paquette, The influence of hydrogen on the chemical, mechanical, optical/electronic, and electrical transport properties of amorphous hydrogenated boron carbide, *J. Appl. Phys.* 118 (2015) 35703. doi:10.1063/1.4927037.
- [26] M. Dłużniewski, S. Kania, Charge carrier lifetime in DLC films, *Diam. Relat. Mater.* 14 (2005) 74–77. doi:10.1016/j.diamond.2004.07.015.
- [27] T. Pisarkiewicz, S. Kuta, A measurement set-up for photoconductivity decay experiments, *Meas. Sci. Technol.* 9 (1998) 1007. doi:10.1088/0957-0233/9/6/018.
- [28] Ruqiang Bao, Zijie Yan, D.B. Chrisey, Charge carrier lifetime in boron carbide thin films, *Appl. Phys. Lett.* 98 (2011) 192106. doi:10.1063/1.3589816.

- [29] C. Vijila, S.P. Singh, E. Williams, P. Sonar, A. Pivrikas, B. Philippa, R. White, E.N. Kumar, S.G. Sandhya, S. Gorelik, J. Hobley, A. Furube, H. Matsuzaki, R. Katoh, Relation between charge carrier mobility and lifetime in organic photovoltaics, *J. Appl. Phys.* 114 (2013) 184503. doi:10.1063/1.4829456.

## Chapter 5 Conductance *versus* Frequency Measurements

### 5.1 Introduction

This chapter of my dissertation was published IEEE Transactions on Nuclear Science in November of 2016 (DOI: 10.1109/TNS.2016.2626268), and is reprinted with permission, (2016) IEEE. A device to be used as a neutron detector or neutron voltaic by generating a current pulse from a neutron impact must be capable of tolerating any damage caused by the impact without adverse effects to device efficiency. Chapter 3 [1] showed that heterojunction device performance improved with moderate amounts of He<sup>+</sup> ion irradiation, and was the first to study the effects of radiation on amorphous boron carbides as an electrical device. The ramifications of the physical changes on the electrical properties of semiconducting boron carbides have not been examined. The intrinsic properties of PECVD semiconducting partially dehydrogenated boron carbide on silicon p-n heterojunction diodes may be improved as degraded icosahedral structures (icosahedral carborane molecules, B<sub>10</sub>C<sub>2</sub>H<sub>12</sub>, missing B, C, or H atoms) heal under neutron, electron, and He<sup>+</sup> ion irradiation. If the defect concentration is reduced, and the charge carrier mobility is increased with irradiation, this could lead to a much more efficient device the longer the device is in service, even in extremely radiation harsh environments.

Boron based thermal neutron detectors and neutron voltaics are capable of operation due to a capture-fragmentation-emission process with daughter fragment particles <sup>7</sup>Li, and He<sup>+</sup> ( $\alpha$ ) with large translational energy. The energetic <sup>7</sup>Li and  $\alpha$  fragments deposit energy in the semiconducting partially dehydrogenated boron carbide and the silicon substrate. As discussed in Chapter 3, there are two main means of energy deposition: ionization/excitation [2] which can lead to bond breaking, and

elastic collisions (recoil) between the projectile ion and the atoms of the target material. This energy deposition can result in atomic displacements, ultimately leading to damage accumulation.

One of the more common ways to characterize a semiconductor device is through capacitance *versus* frequency and capacitance *versus* voltage measurements with a small ac perturbation signal imposed across the device under test in a 4-point parallel circuit utilizing an impedance analyzer. This works well for devices with efficient charge separation and negligible conductance. However, if the device is highly trapped, or has a high defect concentration, the contributions to the capacitor charging current are no longer negligible. These so-called “leaky diodes” are not always accurately characterized using the capacitance measurements mentioned above because their dissipation factor ( $D$ ) becomes excessive

*Equation 5-1*

$$D = G/(\omega C_p)$$

where  $G$  is conductance,  $\omega$  is angular frequency ( $\omega=2\pi f$ ),  $f$  is small signal perturbation frequency, and  $C_p$  is equivalent parallel circuit capacitance. In the case of a large dissipation factor ( $D > 10$ ), a more suitable measurement is conductance *versus* frequency or conductance *versus* voltage. This paper seeks to determine the conductance as a function of frequency, and compare the calculated values to experimental data to examine changes in the electrical properties of the semiconducting partially dehydrogenated boron carbide as a function of radiation. For reference, the dc current *versus* voltage  $I(V)$  curves as a function of irradiation are shown in Fig. 3.2 [1].

## 5.2 Experimental Details

Device synthesis for research in this set of experiments follows the same path as that outlined in Chapter 3.2 (1-10  $\Omega \times \text{cm}$  Si substrate). The process for PECVD synthesized  $a\text{-B}_{10}\text{C}_{2+x}\text{H}_y$  films on silicon wafers creating a p-n heterojunction have been described in Chapter 2.1 and previous work [3–6]. Metallization follows the procedures outlined in Chapter 2.2.

Following irradiation, the samples were returned for electrical characterization. Conductance *versus* frequency  $G(f)$  measurements were taken using an HP model 4192A impedance analyzer with an oscillation voltage set to 0.010 v in a 4 point parallel circuit. The analyzer has 4 parallel connections. From left to right, they are: low current, low potential, high potential, high current. By creating a metal housing for the diode under test and connecting the housing directly to the analyzer through un-insulated BNC connectors, the negative portion of the 4 connections are grounded to the analyzer creating an RF shield around the diode under test. The 4192A impedance analyzer has a conductance measurement range of  $1 \times 10^{-9} \Omega^{-1}$  to  $12.999 \Omega^{-1}$  with an accuracy of 0.1%, and a resolution of 4 ½ digits for both grounded and floated devices.

## 5.3 Results

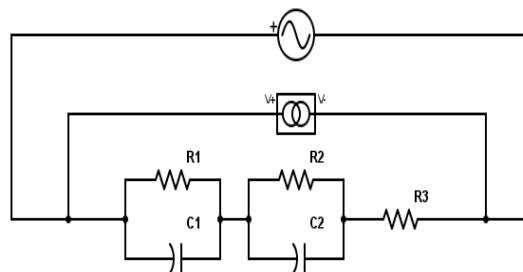


Fig. 5.1: Circuit model used in analysis.  $R1$  and  $C1$  represent the resistance and capacitance of the  $a\text{-B}_{10}\text{C}_{2+x}\text{H}_y$ ,  $R2$  and  $C2$  represent the resistance and capacitance of the silicon, and  $R3$  represents series resistance.

Fig. 5.1 is an illustration of the circuit used to model the device under test. The small signal equivalent circuit of a p-n junction may be modeled as three parallel components comprised of the junction capacitance, diffusion capacitance, and conductance, with the junction capacitance being frequency independent [7]. C1 is interpreted as the combination of the two parallel capacitance components above due to the depletion region of the a-B<sub>10</sub>C<sub>2+x</sub>H<sub>y</sub>/Si interface. R1 is interpreted as the parallel junction resistance at the a-B<sub>10</sub>C<sub>2+x</sub>H<sub>y</sub>/Si interface. The resistance of the quasi-neutral region in the silicon substrate, metal contacts, connecting wires, and internal resistance of the analyzer are represented as the equivalent series resistance (R3). The single parallel circuit along with the equivalent series resistance suitably modeled the virgin diode. Once irradiated, this was no longer sufficient and a second RC parallel component of the circuit was found to be required. It has been shown that bulk radiation damage has a significant effect on charge carrier concentration profiles in silicon [8–14], and that single crystal silicon type-inverts from n-type to p-type at a fluence of  $1.19 \times 10^{14}$  neutrons/cm<sup>2</sup> [15], and at  $1.5 \times 10^{13}$  protons/cm<sup>2</sup>. [16] shows that the fluence required to achieve an equivalent amount of He<sup>+</sup> ion damage to 1 MeV neutrons is of the same order of magnitude (i.e.  $4.4 \times 10^{11}$  neutrons/cm<sup>2</sup> =  $1 \times 10^{11}$  ions/cm<sup>2</sup>). The lowest fluence in this study was  $6.5 \times 10^{16}$  ions/cm<sup>2</sup>, 2 orders of magnitude greater than reported as required for type inversion. C2 is interpreted as the junction and diffusion capacitance of the depletion region between the type-inverted irradiated silicon and virgin silicon. R2 is interpreted as the parallel junction resistance between the p-n homojunction at the irradiated silicon to virgin silicon interface.

To develop an equation for conductance as a function of frequency, an equation for equivalent complex impedance (*Z*) of the circuit is required. This

equation plus a full derivation of the measured conductance equation is provided in Appendix A. It should be noted that while the impedance analyzer has an inductive component inherent to the machine, it was found that any inductive component was negligible in modeling the data, and is omitted from the equations. The equation describing the measured conductance  $G_m$  was found to be:

Equation 5-2

$$G_m = \frac{\omega^2((C1 R1 R2 + C2 R1 R2)(C1 R1 + C2 R2) + R3(C1 R1 + C2 R2)^2)}{\sigma_4} - \frac{(C1 C2 R1 R2 \omega^2 - 1)(-C1 C2 R1 R2 R3 \omega^2 + R1 + R2 + R3)}{\sigma_4}$$

where

$$\sigma_4 = (C1 R1 R3 \omega + C2 R2 R3 \omega + C1 R1 R2 \omega + C2 R1 R2 \omega)^2 + (-C1 C2 R1 R2 R3 \omega^2 + R1 + R2 + R3)^2$$

Table 5-1 shows the results obtained for the fitting parameters of Equation 5-2. As stated earlier, the virgin device was capable of being modeled with only the parameters of C1, R1, and R3. After moderate irradiation to 0.1 dpa, a second parallel resistive (R2) and capacitive (C2) component is required. Table 5-1 shows these values to be 40  $\Omega$  and  $1.166 \times 10^{-9}$  F. Additionally, the resistance of R1 is reduced by 55.2%. Irradiation to 0.2 dpa in the a-B<sub>10</sub>C<sub>2+x</sub>H<sub>y</sub> film, results in a dramatic increase in resistance R1 of 1341.8%.

TABLE 5-1

Fitting Parameter Values of Equation 5-2

Sample	C1 (nF)	R1 ( $\Omega$ )	R3 ( $\Omega$ )	C2 (nF)	R2 ( $\Omega$ )	$\chi^2$
Virgin	1.150	6082	90	0	0	0.0006360
0.1 dpa	0.8673	2782	70	1.166	40	0.0003835
0.2 dpa	0.8711	39000	70	1.617	50	0.0001278
0.3 dpa	0.7624	77440	133	0.8554	95	0.0004651
0.5 dpa	1.294	190000	65	1.752	38	0.0008379

C1 is interpreted as the capacitance due to the a-B<sub>10</sub>C<sub>2+x</sub>H<sub>y</sub> dielectric film. R2 is interpreted as the a-B<sub>10</sub>C<sub>2+x</sub>H<sub>y</sub>/Si junction resistance and a-B<sub>10</sub>C<sub>2+x</sub>H<sub>y</sub>/Cr contact resistance, C2 is interpreted as the Si(Irradiate)/Si(virgin) homojunction capacitance, R2 is interpreted as the junction resistance of the Si(Irradiate)/Si(virgin) homojunction, and R3 is interpreted as the equivalent series resistance of the device.  $\chi^2$  is the chi square goodness-of-fit-test statistic. A  $\chi^2$  value < 0.412 corresponds to a 99.5% confidence level.

Irradiation to 0.3 dpa in the a-B<sub>10</sub>C<sub>2+x</sub>H<sub>y</sub> film, results in another dramatic increase in resistance parameter R1 of 98.6%. Further irradiation to 0.5 dpa in the a-B<sub>10</sub>C<sub>2+x</sub>H<sub>y</sub> film, continues the trend of another dramatic increase in the resistance of parameter R1 of 145.4%. The parameter interpreted as the equivalent series resistance of the device (R3) remains within the expected range calculated for the quasi-neutral silicon substrate of 26 to 260  $\Omega$  based on the resistivity range provided by the manufacturer. The changes of R3 listed in Table 5-1 are not viewed as a significant deviation. Changes in the fitting parameters C1 and C2 of tenths of a nano-farad, are not viewed as significant deviations as the device is irradiated. Changes in the parallel resistance parameter R2 follow the general pattern of R3, and are interpreted as minor changes in the carrier concentration profile inherent to the substrate rather than a result of changes due to irradiation.

When the modeled conductance is overlaid on the measured data on a linear scale, the two are nearly indistinguishable. This is indicated by the chi square goodness-of-fit-test statistics with values 3 orders of magnitude less than the value corresponding to a 99.5% confidence interval. Fig. 5.2 shows the measured conductance *versus* frequency and overlaid modeled conductance *versus* frequency

curves on a Log-Log scale. Using the Log-Log scale, Fig. 5.2 shows that the low frequency conductance ( $G_0$ ), is unique for each level of irradiation. Examination of Fig. 5.2 also shows that the frequency at which charge carriers can no longer respond to the perturbation signal (indicated by an increase in conductance) decreases as the level of irradiation damage increases. For the virgin sample, this is just above  $10^4$  Hz, but for the 0.5 dpa sample, there are charge carriers that cannot respond to a 10 Hz signal. The slope of the curves between  $2 \times 10^4$  Hz and 1 MHz is unique to each level of irradiation. The upper limit of conductivity, as frequency approaches infinity ( $f \rightarrow \infty$ ), consolidates into a narrow band. A difference between the virgin and irradiated samples exists.

#### 5.4 Discussion

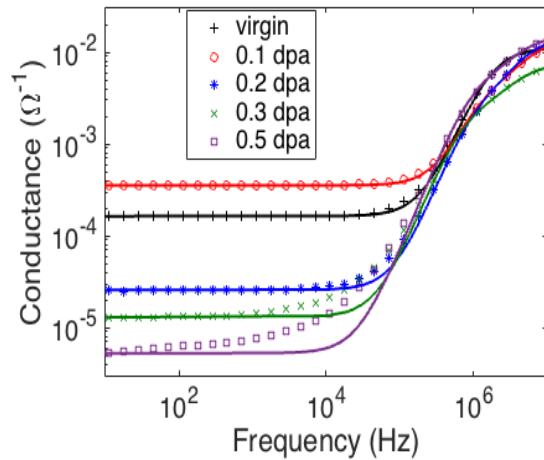


Fig. 5.2: Logarithmic Conductance vs. Frequency curve of  $a\text{-B}_{10}\text{C}_{2+x}\text{H}_y$  on Si heterojunctions. The black '+' represents the measured virgin data. The red 'o' represents the measured 0.1 dpa data. The blue '\*' represents the measured 0.2 dpa data. The green 'x' represents the measured 0.3 dpa data. The purple '□' represents the measured 0.5 dpa data. The colored solid lines are the corresponding calculated models.

The Mathworks® Matlab curve fitting toolbox was utilized to determine the best values for the independent parameters of Equation 5-2 ( $C_1$ ,  $R_1$ ,  $C_2$ ,  $R_2$ ,  $R_3$ ), as a function of the perturbation frequency utilizing bisquare weighting, which gives the strongest weighting to data points near the fit, and low weighting to outlying data points. In fitting the data to obtain the results of Table 5-1, parts of the model are very

sensitive to specific variables of Equation 5-2. In the low frequency range, below 10 kHz, although the limit of  $G_m$  as frequency approaches 0 ( $f \rightarrow 0$ ) is inversely proportional to  $R1 + R2 + R3$ , it is only sensitive to changes in  $R1$  (resistance of the original  $R1$ ,  $C1$  parallel component). In the high frequency range, the limit of  $G_m$  as frequency approaches infinity ( $f \rightarrow \infty$ ) is inversely proportional to  $R3$  (equivalent series resistance of the device). The initial upturn in conductance is dominated by  $C1$ . And the slope between the upper and lower limits of conductance is dominated by  $R2$  and  $C2$  (The resistance and capacitance of the second parallel  $RC$  component).

The model does not fit the low frequency conductance particularly well for the samples irradiated above 0.3 dpa. The TEM images of Chapter 3 [1] show a direct correlation between the SRIM calculated vacancy profile and the damage to the Si substrate as well as between He bubble formation and the SRIM calculated peak of the He distribution profile. The TEM images also provided visual evidence of point defect agglomeration. These structural changes in the Si substrate provide visual indications that di-vacancy states ( $V_2$ ), formed by the combination of vacancies created in close proximity to each other, and other vacancy complexes, allow us to infer that there should be an anisotropic distribution of trap energy states available, as well as a distribution in the concentration of those states. Fig. 5.2 lends electronic evidence to the inferences of the visual evidence of TEM [1]. For the 0.3 dpa and 0.5 dpa samples, it is no longer the junction capacitance (which is frequency independent and is not lifetime sensitive) that dominates in the silicon, but diffusion capacitance or charging due to traps, which are frequency dependent [3]. The junction capacitance is associated with oscillations in the depletion width due to small sinusoidal perturbations [17]. The diffusion capacitance is associated with minority carriers and changes in charge due to the sinusoidal perturbation signal. Because there is a

distribution of trap and acceptor states within the irradiated silicon, the diffusion capacitance will not be a constant, but will itself be a function of frequency, and change the relationship between the complex impedance and frequency.

The equivalent series resistance of the device is dominated by the bulk resistivity of the silicon substrate. The range of this value is easily calculated.

Resistance of a thin film is defined by the equation:

*Equation 5-3*

$$R = \frac{\rho L}{wt}$$

where  $\rho$  is the film resistivity,  $L$  is the length of the surface,  $w$  is the width of the surface (consider  $L$  the longer of the two values), and  $t$  is the film thickness perpendicular to the surface. Though dimensionless, the ratio  $L/W$  is taken as the number of squares through which charge carriers must traverse. A 380  $\mu\text{m}$  thick substrate, with a 2 mm diameter contact (approximating  $L/W = 1$  square) and resistivity between 1 and 10  $\Omega \times \text{cm}$  results in a resistance between 26 and 260  $\Omega$ . As previously stated, the equivalent series resistance parameter  $R_3$  does not deviate from this range, and changes in  $R_3$  are not considered to be a result of irradiation, but rather small changes in carrier concentration within the silicon substrate, or small changes in device preparation.

$R_1$  is the variable that undergoes the most drastic change. According to Nordell *et. al.* [18], the resistivity of  $a\text{-B}_{10}\text{C}_{2+x}\text{H}_y$  films ranges from  $10^{10}$  to  $10^{15}$   $\Omega \times \text{cm}$ . A 200 nm thick film with a 2 mm diameter metal contact (approximating  $L/W = 1$  square) would result in a resistance on the magnitude of  $10^{16}$   $\Omega$ , 11 orders of magnitude greater than any resistance values obtained in Table 1. However, if the film is completely depleted of charge carriers, and only acting as a dielectric between 2 parallel plate contacts with a significant barrier at the silicon interface due to the

heterojunction band misalignment, the values of R1 for the virgin and 0.1 dpa measurements can be explained.

First, it has yet to be shown what metals makes an ohmic contact with a- $B_{10}C_{2+x}H_y$  films. It is possible a metal with a higher work function than chromium is required. This suggests that there could be a contact resistance at the device cathode in the form of a Schottky barrier. However, since the Schottky barrier is a majority carrier process, the barrier is frequency independent, and will only change as a result of chemical or structural changes in the film. The band misalignment between the a- $B_{10}C_{2+x}H_y$  film and the silicon provides a frequency dependent junction resistance that will change as a result of changes in the charge carrier concentrations of either the film or the silicon.

Examining the virgin measurement, we first make the approximation from the indicated parallel resistance of 6082  $\Omega$ , that the a- $B_{10}C_{2+x}H_y$  film is fully depleted. Were this not the case, our calculation above shows that this value or the equivalent series resistance (R3) would be many orders of magnitude larger. This leads to the interpretation of this value as the junction resistance due to barriers within the band structure.

Examining the 0.1 dpa measurement, the second parallel R2 C2 component has an indicated junction resistance of 40  $\Omega$  [19]. Type inverted silicon as a result of neutron radiation reaches an upper limit asymptote of resistivity at approximately  $2.4 \times 10^5 \Omega \times \text{cm}$  [15]. This is a direct result of the damage to the crystalline Si substrate. In order for the Si dopant to contribute to the conductivity of the Si, the substitutional atom (i.e. P) must sit on a Si lattice site. If the dopant is disturbed, and becomes an interstitial defect as a result of radiation damage, it is no longer active, and will not contribute to the conductivity. Prior to the damage clusters created near

the ion end of range, the irradiating ion is creating point defects in the Si all along its ion track. These point defects reduce the average carrier relaxation time and deactivate the dopants, both of which increase the resistivity of the Si.

From Equation 5-3, an ion range of 1400 nm and a contact area again of 2 mm diameter (approximating  $L/W = 1$ ) would result in a resistance in the irradiated silicon of approximately  $1.71 \times 10^9 \Omega$ . However, as before this calculation assumes no depletion region, which is inaccurate. There will be a depletion region at the p-p<sup>+</sup> junction with the a-B<sub>10</sub>C<sub>2+x</sub>H<sub>y</sub>/Si(irradiated), and at the p<sup>+</sup>-n homojunction between the Si(irradiated)/Si(virgin). Since neither the exact carrier concentration or change in band structure is known for the a-B<sub>10</sub>C<sub>2+x</sub>H<sub>y</sub> film, the depletion widths at this junction are not accurately calculable. However, a rough estimate of the depletion width resulting from the p<sup>+</sup>-n homojunction shows the irradiated silicon and a-B<sub>10</sub>C<sub>2+x</sub>H<sub>y</sub> film being fully depleted. Just as with the examination of the a-B<sub>10</sub>C<sub>2+x</sub>H<sub>y</sub> film, a resistance on this order of magnitude is not found in the 0.1 dpa model, and lends support to the full depletion approximation.

Croitoru *et. al.* [15] provide resistivity and mobility measurements of irradiated silicon, allowing for the calculation of the hole carrier concentration for the case  $N_A \gg N_D$  through:

Equation 5-4

$$\rho = \frac{1}{q\mu_p N_A}$$

where  $\rho$  is resistivity,  $q$  is the elementary charge,  $\mu_p$  is the hole hall mobility, and  $N_A$  is the acceptor concentration. Taking the values from Croitoru's highest measured fluences ( $10^{16}$  n/cm<sup>2</sup>) of  $\rho = 234280 \Omega \times \text{cm}$  and  $\mu_p = 70 \text{ cm}^2/\text{Vs}$ , we calculate  $N_A = 3.8 \times 10^{11} \text{ 1/cm}^3$ . The carrier concentration of the virgin silicon substrate is estimated at

$N_D = 1 \times 10^{15} \text{ 1/cm}^3$  (based on the manufacturer's specifications). This leads to an estimate of the silicon homojunction depletion width ( $w$ ) of  $36 \mu\text{m}$ :

Equation 5-5

$$w = \left( \frac{2\varepsilon_1\varepsilon_0}{q} \left( \frac{N_A + N_D}{N_A N_D} \right) V_{bi} \right)^{1/2}$$

Equation 5-6

$$V_{bi} = \frac{kT}{q} \ln \left( \frac{N_A N_D}{n_i^2} \right)$$

where  $\varepsilon_1$  is the dielectric constant,  $\varepsilon_0$  is the permeability of free space,  $N_A$  is the number of acceptors,  $N_D$  is the number of donors,  $V_{bi}$  is the built in voltage,  $n_i$  is the intrinsic carrier concentration,  $k$  is the Boltzmann constant,  $T$  is temperature.

Considering that the ion range is only  $1.4 \mu\text{m}$ , and the a-B<sub>10</sub>C<sub>2+x</sub>H<sub>y</sub> film is only 225 nm thick, we can safely assume that the type-inverted silicon and a-B<sub>10</sub>C<sub>2+x</sub>H<sub>y</sub> film are fully depleted.

Of much more import in the 0.1 dpa data, is the decrease of R1 from 6028 to 2782  $\Omega$ . Using the approximation that the film is fully depleted of charge carriers, and the band alignment of the a-B<sub>10</sub>C<sub>2+x</sub>H<sub>y</sub> film to type inverted silicon is considered, the barrier of a p-p<sup>+</sup> heterojunction will be much smaller than that of a p-n heterojunction even if the constituent band gaps are altered as a result of the irradiation. As an example to prove this point, let us assume the HOMO – LUMO gap of a-B<sub>10</sub>C<sub>2+x</sub>H<sub>y</sub> is 2.0 eV (values of 0.7 to 3.8 eV have been reported [3]). It has been shown that the acceptor and trap energy levels of type-inverted silicon are mid-band gap [20], so let us further assume that the band gap of the silicon is not significantly altered from 1.12 eV. The conduction band barrier of the a-B<sub>10</sub>C<sub>2+x</sub>H<sub>y</sub>/virgin silicon p-n heterojunction is roughly  $2.0 \text{ eV} - (E_f + E_{cN}) - (E_{vp} + E_f) \text{ eV} \approx 2.0 \text{ eV}$ . Through band realignment

of a type-inverted silicon region, the p-p<sup>+</sup> conduction band barrier will be roughly 2.0 eV – 1.12 eV ≈ 0.88 eV. Such a reduction in the barrier height would be reflected in the parallel junction resistance component of our equivalent circuit model. Our example shows a reduction of roughly ½ in barrier height, which compares to our R1 results in Table 5-1.

Examination of the 0.2, 0.3, and 0.5 dpa measurements shows a dramatic increase in the resistance parameter R1 from 2782 to 190000 Ω. Maintaining the assumption that this remains a combination of the junction and contact resistances, one explanation for the dramatic increase of parameter R1 is further heterojunction band modification and/or Schottky barrier modification. This modification could be additional band realignment due to defect passivation resulting in a decrease in N<sub>A</sub> and a shift from a p-type to an intrinsic semiconductor and simultaneously reducing the concentration of recombination/generation centers within the HOMO – LUMO gap. Another possibly is a direct change in the a-B<sub>10</sub>C<sub>2+x</sub>H<sub>y</sub> toward a larger HOMO – LUMO gap.

Chapter 3 [1] showed improved diode rectification for 0.1 and 0.2 dpa irradiated samples through current *versus* voltage  $I(V)$  measurements (Fig. 3.2). Explanations thus far introduced do not account for these findings, meaning an additional mechanism must be at work. Supposition within Chapter 3 [1] was that initial radiation passivated defects of discrete energy levels within the a-B<sub>10</sub>C<sub>2+x</sub>H<sub>y</sub> film. Defect passivation could result from electronic energy deposition, bond breaking and re-formation of the local bonds with a lower total free energy, possibly resolving distorted icosahedron anion states. The low frequency conductance ( $G_0 = dI/dV$ ), taken as  $f < 100$  Hz, has a decreasing trend above 0.1 dpa. This would be reflected in a decrease in recombination/generation centers within the diode. The most likely

place to look for this is within the  $a\text{-B}_{10}\text{C}_{2+x}\text{H}_y$  film, as it has been shown that new mid-band gap vacancy complexes are forming in the silicon [8–14].

## 5.5 Conclusions

In conclusion,  $a\text{-B}_{10}\text{C}_{2+x}\text{H}_y$  on Si p-n heterojunctions were synthesized utilizing PECVD. Following irradiation with 200 keV  $\text{He}^+$  ions, the heterojunction properties were explored through electrical characterization. A model has been presented for calculating conductance as a function of frequency for semiconductors under irradiation. This model was then used to interpret measured data and infer physical and chemical changes in the device.

For low doses of irradiation, the resistance of the R1 component decreased. This is most likely due to band realignment of the  $a\text{-B}_{10}\text{C}_{2+x}\text{H}_y/\text{Si}$  heterojunction as the irradiated silicon type-inverts creating a  $p\text{-}p^+$  heterojunction and reducing the barrier height. Simultaneously, the crystalline Si substrate is being damaged. Point defects are decreasing the average carrier relaxation time, and dopants are being de-activated, resulting in an increase in the resistivity of the Si. For moderate doses of irradiation, it is believed that the electronic energy deposition from the irradiating ions may be perturbing the atoms within the  $a\text{-B}_{10}\text{C}_{2+x}\text{H}_y$  film allowing for the elimination of defects, and decreasing the hole concentration ( $N_A$ ). Even though the  $a\text{-B}_{10}\text{C}_{2+x}\text{H}_y$  film is fully depleted of charge carriers, changes to the defect concentration (i.e. concentration of generation/recombination centers), and hole concentration ( $N_A$ ) will change the Fermi energy ( $E_F$ ) location within the HOMO-LUMO gap. This in turn causes band re-alignment, and would change the energy barrier at the  $a\text{-B}_{10}\text{C}_{2+x}\text{H}_y/\text{Si}$  junction. Therefore, if the  $a\text{-B}_{10}\text{C}_{2+x}\text{H}_y$  film has been altered to have less recombination/generation centers and/or smaller  $N_A$  the  $a\text{-B}_{10}\text{C}_{2+x}\text{H}_y/\text{Si}$  junction resistance will increase, explaining the results of R1 in Table 5-1.

While this paper presents a possible explanation for the initial increase in heterojunction device performance under irradiation, it is still not entirely clear to what extent the  $a\text{-B}_{10}\text{C}_{2+x}\text{H}_y$  film is chemically or structurally modified by the irradiating ions. A more direct means of investigating the  $a\text{-B}_{10}\text{C}_{2+x}\text{H}_y$  film is required. Future experiments seek to examine  $a\text{-B}_{10}\text{C}_{2+x}\text{H}_y$  films as a lossy capacitor in a metal oxide semiconductor system (C-MOS). This will allow for the elimination of the issues created by the changing silicon substrate and exclusively examine the charge carriers of the  $a\text{-B}_{10}\text{C}_{2+x}\text{H}_y$  film.

## 5.6 References

- [1] G. Peterson, Q. Su, Y. Wang, P.A. Dowben, M. Nastasi, Improved p–n heterojunction device performance induced by irradiation in amorphous boron carbide films, *Mater. Sci. Eng. B.* 202 (2015) 25–30.  
doi:10.1016/j.mseb.2015.09.002.
- [2] M. Nastasi, J.W. Mayer, *Ion Implantation and Synthesis of Materials*, Springer, 2006.  
<http://www.springer.com/physics/particle+and+nuclear+physics/book/978-3-540-23674-0> (accessed February 5, 2015).
- [3] E. Echeverria, B. Dong, G. Peterson, J.P. Silva, E.R. Wilson, M.S. Driver, Y.-S. Jun, G.D. Stucky, S. Knight, T. Hofmann, Z.-K. Han, N. Shao, Y. Gao, W.-N. Mei, M. Nastasi, P.A. Dowben, J.A. Kelber, Semiconducting boron carbides with better charge extraction through the addition of pyridine moieties, *J. Phys. Appl. Phys.* 49 (2016) 355302–355312. doi:10.1088/0022-3727/49/35/355302.
- [4] G.G. Peterson, E. Echeverria, B. Dong, J.P. Silva, E.R. Wilson, J.A. Kelber, M. Nastasi, P.A. Dowben, Increased drift carrier lifetime in semiconducting boron carbides deposited by plasma enhanced chemical vapor deposition from carboranes and benzene, *J. Vac. Sci. Technol. Vac. Surf. Films.* 35 (2016) 03E101. doi:10.1116/1.4973338.
- [5] E. Echeverría, R. James, F.L. Pasquale, J.A.C. Santana, M.S. Driver, A. Enders, J.A. Kelber, P.A. Dowben, Neutron Detection Signatures at Zero Bias in Novel Semiconducting Boron Carbide/Pyridine Polymers, *MRS Online Proc. Libr. Arch.* 1743 (2015). doi:10.1557/opl.2015.352.
- [6] B. Dong, R. James, J.A. Kelber, PECVD of boron carbide/aromatic composite films: Precursor stability and resonance stabilization energy, *Surf. Coat. Technol.* 290 (2016) 94–99. doi:10.1016/j.surfcoat.2015.09.042.

- [7] R.F. Pierret, *Semiconductor Device Fundamentals*, 2nd edition, Addison Wesley, Reading, Mass, 1996.
- [8] K. Gill, G. Hall, B. MacEvoy, Bulk damage effects in irradiated silicon detectors due to clustered divacancies, *J. Appl. Phys.* 82 (1997) 126–136. doi:10.1063/1.365790.
- [9] K. Gill, G. Hall, S. Roe, S. Sotthibandhu, R. Wheadon, P. Giubellino, L. Ramello, Radiation damage by neutrons and protons to silicon detectors, *Nucl. Instrum. Methods Phys. Res. Sect. Accel. Spectrometers Detect. Assoc. Equip.* 322 (1992) 177–188. doi:10.1016/0168-9002(92)90027-2.
- [10] E. Fretwurst, H. Feick, M. Glaser, C. Gößling, E.H.M. Jeijne, A. Hess, Reverse annealing of the effective impurity concentration and long-term operational scenario for silicon detectors in future collider experiments, *Nucl. Instrum. Methods Phys. Res. Sect. Accel. Spectrometers Detect. Assoc. Equip.* (1994). doi:10.1016/0168-9002(94)91417-6.
- [11] D. Pitzl, N. Cartiglia, B. Hubbard, D. Hutchinson, J. Leslie, K. O’Shaughnessy, W. Rowe, H.F.-W. Sadrozinski, A. Seiden, E. Spencer, H.J. Ziock, P. Ferguson, K. Holzscheiter, W.F. Sommer, Type inversion in silicon detectors, *Nucl. Instrum. Methods Phys. Res. Sect. Accel. Spectrometers Detect. Assoc. Equip.* 311 (1992) 98–104. doi:10.1016/0168-9002(92)90854-W.
- [12] P.A. Aarnio, M. Huhtinen, M. Pimiä, K. Kaita, M. Laakso, A. Numminen, P. Ryytty, Damage observed in silicon diodes after low energy pion irradiation, *Nucl. Instrum. Methods Phys. Res. Sect. Accel. Spectrometers Detect. Assoc. Equip.* 360 (1995) 521–531. doi:10.1016/0168-9002(95)00008-9.

- [13] S.J. Bates, C. Furetta, M. Glaser, F. Lemeilleur, E. León-Florián, C. Gößling, B. Kaiser, A. Rolf, R. Wunstorf, H. Feick, E. Fretwurst, G. Lindström, M. Moll, G. Taylor, A. Chilingarov, Pion-induced damage in silicon detectors, *Nucl. Instrum. Methods Phys. Res. Sect. Accel. Spectrometers Detect. Assoc. Equip.* 379 (1996) 116–123. doi:10.1016/0168-9002(96)00538-4.
- [14] K. Riechmann, K.T. Knöpfle, V.M. Pugatch, Pion and proton induced radiation damage to silicon detectors, *Nucl. Instrum. Methods Phys. Res. Sect. Accel. Spectrometers Detect. Assoc. Equip.* 377 (1996) 276–283. doi:10.1016/0168-9002(95)01408-X.
- [15] N. Croitoru, R. Dahan, P.G. Rancoita, M. Tattaggi, G. Rossi, A. Seidman, Study of resistivity and majority carrier concentration of silicon detectors damaged by neutron irradiation up to 1016 n/cm<sup>2</sup>, *Nucl. Instrum. Methods Phys. Res. Sect. B Beam Interact. Mater. At.* 124 (1997) 542–548. doi:10.1016/S0168-583X(97)00055-4.
- [16] E. Borchi, M. Bruzzi, Radiation damage in silicon detectors, *Riv. Nuovo Cimento* 1978-1999. 17 (2007) 1–63. doi:10.1007/BF02724516.
- [17] S.S. Li, p-n Junction Diodes, in: S.S. Li (Ed.), *Semicond. Phys. Electron.*, Springer New York, 2006: pp. 334–380.  
[http://link.springer.com/chapter/10.1007/0-387-37766-2\\_11](http://link.springer.com/chapter/10.1007/0-387-37766-2_11) (accessed October 16, 2015).
- [18] B.J. Nordell, S. Karki, T.D. Nguyen, P. Rulis, A.N. Caruso, S.S. Purohit, H. Li, S.W. King, D. Dutta, D. Gidley, W.A. Lanford, M.M. Paquette, The influence of hydrogen on the chemical, mechanical, optical/electronic, and electrical transport properties of amorphous hydrogenated boron carbide, *J. Appl. Phys.* 118 (2015) 35703. doi:10.1063/1.4927037.

- [19] Kim, J.M. Beebe, Y. Jun, X.-Y. Zhu, C.D. Frisbie, Correlation between HOMO Alignment and Contact Resistance in Molecular Junctions: Aromatic Thiols versus Aromatic Isocyanides, *J. Am. Chem. Soc.* 128 (2006) 4970–4971. doi:10.1021/ja0607990.
- [20] B.C. MacEvoy, G. Hall, K. Gill, Defect evolution in irradiated silicon detector material, *Nucl. Instrum. Methods Phys. Res. Sect. Accel. Spectrometers Detect. Assoc. Equip.* 374 (1996) 12–26. doi:10.1016/0168-9002(96)37410-X.

## Chapter 6 Improved p-n Heterojunction Performance After Neutron Irradiation

### 6.1 Introduction

This chapter is an expanded version of a manuscript being developed for publication as a follow up to the publication that represents Chapter 3 of this dissertation. The target journal is the Journal of Applied Physics. All TEM sample preparation and images are the work of Qing Su of the Nebraska Center for Energy Sciences Research at the University of Nebraska – Lincoln. The calculations and figures for carrier concentration and built-in potential were a collaborative effort with Michael Nastasi, Director of the Nebraska Center for Energy Sciences Research at the University of Nebraska – Lincoln.

Boron rich semiconducting icosahedral based materials have been investigated for application in solid-state neutron detection [1–12] and as a potential neutron voltaic [13,14] for some time [15]. Recent work suggests that boron carbide [16,17] and boron phosphide [18,19] based devices improve with some He<sup>+</sup> ion radiation exposure, and are robust against radiation induced device degradation and failure. These results suggest, but do not conclusively show that such devices are robust against neutron irradiation that results in neutron capture by <sup>10</sup>B and then fragmentation into energetic <sup>7</sup>Li/He<sup>+</sup> ion pairs.

Prior studies indicated that device failure, under He<sup>+</sup> ion irradiation, is the result of damage in the crystalline silicon (c-Si) substrate [16]. It was suggested [16] that the damage to the silicon was mostly due to elastic collisions of the incident ion with the c-Si atoms near the ion end of range where Frenkel pairs, ion implantation, and extended defects form, although mechanisms have been put forward [20–22].

Here is an effort to provide additional insight into the changes of the device as a result of irradiation induced changes in the amorphous partially dehydrogenated semiconducting boron carbide film.

The back contact of the device was formed by a metal-semiconductor Schottky barrier, which has its own capacitance. The capacitance of the Schottky barrier and the capacitance of the p-n heterojunction then combine as capacitors in series. Electrical RC circuits that connect capacitors in series combine as:

*Equation 6-1*

$$C_{eq} = \frac{1}{1/C_1 + 1/C_2 + 1/C_3 + \dots + 1/C_n}$$

limiting the charge build up across all capacitors in the circuit to the maximum charge capacity of the smallest capacitor. By placing a metal-semiconductor Schottky barrier on the backside of our device with a smaller capacitive component than the p-n heterojunction component, we limit the charge build up across the p-n metallurgical junction limiting the depletion region of the device, and allowing for electrical measurement and characterization of the diode according to the equations of state as traditionally derived. This element of our device structure and the relationships described by Equation 6-1 become an important factor in understanding the capacitance versus voltage data presented in Fig 6.4.

## 6.2 Experimental Details

Device synthesis begins with an n-type silicon (P doped) substrate (001) of resistivity  $65 - 110 \Omega \times cm$  (purchased from Silicon Inc). The PECVD parameters, substrate preparation, and metallization are all as described in Chapter 2 and have been previously reported [2–5,8–14,16,24]. The only deviation from what is described in Chapter 2 is the size of the contacts deposited on the top and bottom of the devices.

The top shadow masks were changed to a 6 mm×8 mm rectangular shadow mask was utilized to deposit Au on the  $a\text{-}B_{10}C_{2+x}H_y$  thin film, and Cr/Au was deposited over the entire backside of the wafer prior to  $a\text{-}B_{10}C_{2+x}H_y$  thin film synthesis.

Neutron irradiation was achieved using a deuterium-tritium (DT) neutron source (Thermo Scientific MP 320 neutron generator) [25]. This DT source produces 14 MeV neutrons, and was combined with a 10 cm beryllium (Be) cube neutron multiplier. These neutrons were moderated by 1 inch of paraffin, providing approximately 7500 neutrons/cm<sup>2</sup>/s. Flux calibration, neutron moderation, and generator to sample geometry is outlined elsewhere [24]. The generator produced neutrons using the following settings: duty cycle of 10%, beam current of 30  $\mu\text{A}$ , and an accelerator voltage of 80 kV. Because of the paraffin wax enclosure, neutrons are scattered at the inside of the enclosure resulting in a slightly anisotropic  $4\pi$  neutron environment (opposed to a directional irradiation beam emanating from the generator) for the irradiated samples with neutrons of varying energies centered about 0.025 eV [24]. Air cooling was applied to ensure that the environmental temperature remained below 55 °C to prevent melting of the paraffin wax.

Current *versus* voltage measurements and capacitance *versus* voltage measurements are outlined in Chapters 2.6 and 2.7. (HR)TEM measurements are outlined in Chapter 2.3. Ellipsometric measurements were obtained using a J. A. Woollam Company M-2000VI spectroscopic rotating compensator ellipsometer.

### 6.3 Results

The creation of  ${}^7\text{Li}$  (0.84 MeV) and alpha particle ( $\text{He}^+$ ) (1.47 MeV), the fragments (ions), following neutron capture by a  ${}^{10}\text{B}$  atom, leads to the production of an excess of  $10^6$  electron – hole pairs. From *Monte Carlo* SRIM (stopping range of ions in matter code) simulations [26], the  ${}^7\text{Li}$  ion has a range of approximately 2.5

$\mu\text{m}$ , and the  $\text{He}^+$  has a range of approximately  $5.2 \mu\text{m}$  in Si. Upon fragmentation and translation away from the capture site, the direction of translation is completely random with equal chances of translating into the Si substrate, out of the top of the film, parallel to the interface plane, and all angles in between (with the  $^7\text{Li}$  and  $\text{He}^+$  translating in opposite directions), as shown in Fig. 6:1.

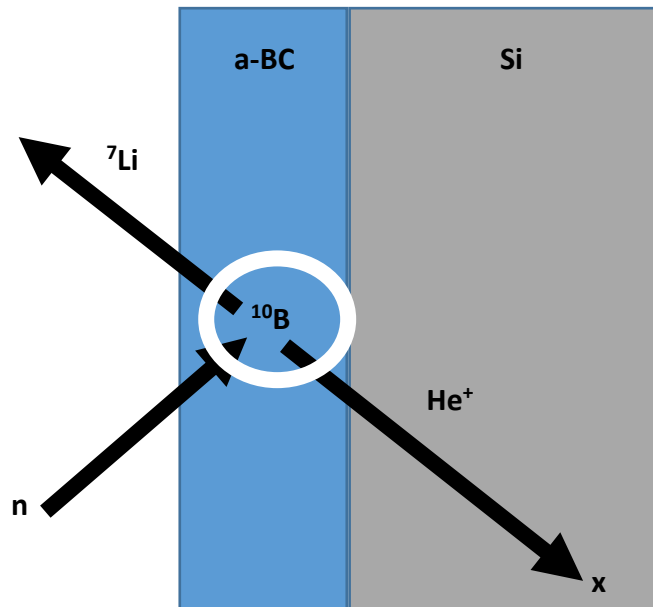


Fig. 6.1: Cartoon of neutron capture by a  $^{10}\text{B}$  isotope resulting in fragmentation into a  $^7\text{Li}$  and  $\text{He}^+$  ions with kinetic energy resulting in translation away from the capture site (not to scale). Unless ion translation is parallel to the interface, one ion will exit the  $\text{a-B}_{10}\text{C}_{2+x}\text{H}_y$  film, and one will implant within the Si substrate, as represented by the "x".

There are two types of energy deposition from an irradiating ion: electronic stopping (ionization energy) and elastic collisions (recoil energy) [27]. Ionization energy deposition represents a sudden perturbation to the system by the transfer of energy from the irradiating ion to the electrons of the target atoms. This results in the breaking of bonds if the energy deposition rate per atom is larger than the bonding energy. Recoil energy deposition is due to collisions between the irradiating ion and the target atom nuclei, causing cascades of displacement damage in the form of Frenkel pairs and extended defects. TEM and SRIM analysis, reported elsewhere [16], showed that initial energy deposition by an incident ion (200 keV  $\text{He}^+$ ) will be

dominated by ionization energy and only near ion end of range (where ion implantation occurs) will the recoil energy deposition become dominant. The rate of ionization energy deposition between the Si substrate and  $a\text{-B}_{10}\text{C}_{2+x}\text{H}_y$  film is very similar indicating that the ion range is going to be similar in magnitude for both materials. Ellipsometry measurements indicate a virgin film thickness of 192 nm, meaning that only if the translational direction is parallel to the interface plane will the ion range terminate inside of the  $a\text{-B}_{10}\text{C}_{2+x}\text{H}_y$  film, allowing for the assumption that the vast majority of energy deposition within the  $a\text{-B}_{10}\text{C}_{2+x}\text{H}_y$  film is ionization energy.

While the neutron flux is approximately 7500 neutrons/cm<sup>2</sup>/s, it is important to know how sensitive the  $a\text{-B}_{10}\text{C}_{2+x}\text{H}_y$  film is to the neutrons. The following is a calculation for number of neutrons captured by the  $a\text{-B}_{10}\text{C}_{2+x}\text{H}_y$  film [28]. The number of transmitted neutrons ( $N_T$ ) is given by:

Equation 6-2

$$N_T = N_n e^{-n\sigma d} \left( \frac{n}{\text{cm}^2} \right)$$

Where  $N_n$  is the fluence of neutrons on a sample ( $3000 \frac{n}{\text{cm}^2 \text{ s}}$ ) [24],  $n$  is the atomic density of <sup>10</sup>B,  $\sigma$  is the neutron absorption cross section ( $3.835 \times 10^{-21} \text{ cm}^2$  [28]), and  $d$  is the film thickness ( $5 \times 10^{-5} \text{ cm}$  according to ellipsometry measurements).  $n$  is determined by:

Equation 6-3

$$n = m \times N = \frac{m N_A \rho}{M}$$

Where  $m$  is the atomic fraction abundance of <sup>10</sup>B,  $N_A$  is Avogadro's Number,  $\rho$  is the molar mass of the film in g/cm<sup>3</sup> ( $1.7 \text{ g/cm}^3$  according to XRR measurements), and  $M$  is the molar mass in g/mol.  $m$  was determined from ERD measurements, which showed a film stoichiometry of roughly B<sub>5</sub>C<sub>1</sub>H<sub>2</sub>. Thus the % B in the film is 5/8 =

63%.  $^{10}\text{B}$  has a natural abundance of 20%. Therefore the %  $^{10}\text{B}$  in the film is  $0.20 \times 0.63 = 12.5\%$ . According to Nastasi [27],  $M$  is the total mass divided by the number of molecular units:

$$B = (10.81 \text{ g/mol}) \times 5 = 54.05$$

$$C = (12.01 \text{ g/mol}) \times 1 = 12.01$$

$$H = (1.01 \text{ g/mol}) \times 2 = 2.02$$

$$\text{Total Mass} = 68.08 \text{ g}$$

$$M = \frac{68.08}{5 + 1 + 2} = 8.5 \frac{\text{g}}{\text{mol}}$$

The film atomic density ( $N$ ) is given by:

Equation 6-4

$$N = \frac{N_A \rho}{M} = \frac{6.022 \times 10^{23} (\text{mol}^{-1}) \times 1.7 \left( \frac{\text{g}}{\text{cm}^3} \right)}{8.5 \left( \frac{\text{g}}{\text{mol}} \right)} = 12.04 \times 10^{22} \left( \frac{\text{atoms}}{\text{cm}^3} \right)$$

The atomic density of  $^{10}\text{B}$  is then: ( $n = m \times N = 0.125 \times 12.04 \times 10^{22} \left( \frac{\text{atoms}}{\text{cm}^3} \right) = 1.50 \times 10^{22} \frac{^{10}\text{B}}{\text{cm}^3}$ ).

From Equation 6-2, we see that the fraction of transmitted neutrons is:

$$\frac{N_T}{N_n} = e^{-n\sigma d} = e^{-(1.5 \times 10^{22} \times 3.835 \times 10^{-21} \times 5 \times 10^{-5})} = 0.99700$$

Multiplying by  $N_n$  shows that the number of transmitted neutrons is  $0.99700 \times$

$3000 \frac{n}{\text{cm}^2\text{s}} = 2991 \frac{n}{\text{cm}^2\text{s}}$ . The number of absorbed neutrons is then the flux minus the number of neutrons transmitted

Equation 6-5

$$N_{ABS} = N_n - N_T = 3000 - 2991 = 9 \frac{n}{\text{cm}^2\text{s}}$$

Our samples are roughly  $1\text{cm} \times 1\text{cm}$ , so in 1 hour,  $9 \frac{n}{\text{cm}^2\text{s}} \times 1\text{cm}^2 \times 3600\text{s} =$

$32400 \frac{\text{Li-}\alpha \text{ pairs}}{\text{hr}}$  are generated within the film.

From the diode  $I(V)$  curves of Fig. 6.2, for an  $a\text{-}B_{10}C_{2+x}H_y/Si$  heterojunction diode after 0, 10, 20, and 40 hours of exposure to neutron irradiation, it is evident that the  $I(V)$  curve shows that the device performance *improves* with small amounts of neutron irradiation. For the following discussion, the turn-on voltage was determined by extrapolating a linear fit of the data in the large forward bias region (i.e. 2 V to 1 V for the 40 hour irradiated sample) to a current density of zero. In comparing the diode current in Fig. 6.2, the value at 1.55 V was chosen because that applied bias is slightly greater than the highest turn-on voltage. In the forward bias region, it is immediately evident that after 10 hours of irradiation (red), corresponding to roughly  $2.7 \times 10^8$  neutrons/cm<sup>2</sup>, the diode current increases by 325.9%, and the device turn-on voltage decreases from 1.52 V to 1.25 V. After 20 hours of irradiation (purple), the diode current is 188.8% greater than the virgin (black) device, and the turn-on voltage is 1.42 V. After 40 hours of irradiation (blue), corresponding to roughly  $1.08 \times 10^9$  neutrons/cm<sup>2</sup>, the diode current is 618.0% greater than the virgin device, and the turn on voltage is 1.16 V, a decrease of 23.7% from the virgin device. In the reverse bias region, though not visible in Fig. 6.2, after 10 hours of irradiation, there is a decrease in the reverse bias current (i.e. increased current rectification) of 13.2% at an applied bias of -10 V. After 20 hours of irradiation, this trend reverses, and the reverse bias current has increased 374% at an applied bias of -5 volts over the virgin reverse bias current. After 40 hours of irradiation, the reverse bias current has increased by 605.3% over the virgin reverse bias current at an applied bias of -5 volts.

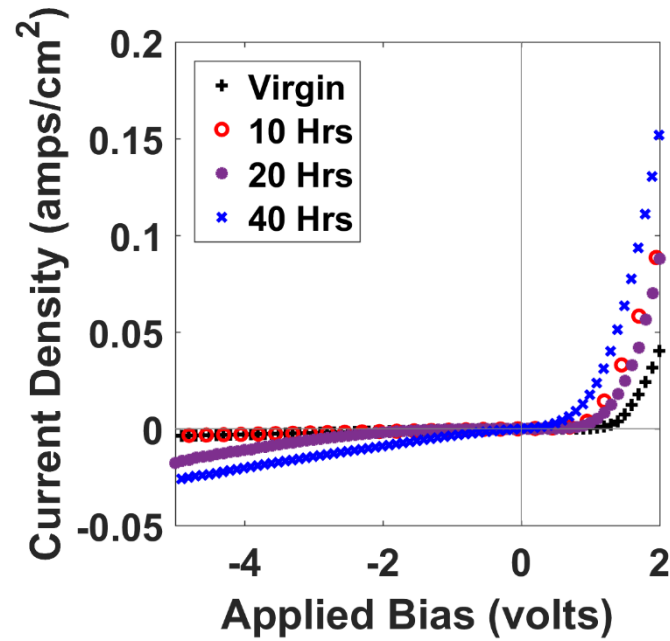


Fig. 6.2: The current versus voltage curves of a boron carbide to silicon heterojunction diode following neutron irradiation times of 0, 10, 20, and 40 hours of exposure.

The p-n junction device current density *versus* voltage  $I(V)$  curves shown in Fig. 6.2 were used as a “Figure of Merit”. Previous work [16] sought to better quantify the improvement of the overall device performance, as well as device degradation and established a second Figure of Merit. This Figure of Merit was the ratio of the differential diode conductance, a ratio of the low frequency diode conductance ( $G_0 = dI/dV$ ) under forward bias to the low frequency diode conductance under reverse bias.  $G_0$  for both forward and reverse bias conditions were taken from the  $I(V)$  data in the range  $\pm 0.75$  to 1.00 applied volts. The higher the ratio, the better the heterojunction diode performance (Figure of Merit), as in previous work [16,29–31]. This is plotted in Fig. 6.3 with the error bars representing the standard deviation for the range. After 10 hours of irradiation, the increase in device current and slight increase in current rectification results in a better performing device with an increase in the ratio from 0.8 to 26.1. After 20 hours of irradiation, a slight decrease in the ratio is observed to 20.5 representing the onset of device degradation (i.e. current rectification decreases). After 40 hours of irradiation, the ratio has further decreased

to 1.9. The differential diode conductance Figure of Merit (Fig. 6.3) displays that the change in device performance with neutron irradiation has a very similar response pattern to that of  $\text{He}^+$  ion irradiation reported in our previous work [16].

While the Schottky barrier diode limits the charging across the p-n heterojunction structure, it does not change the carrier lifetimes of the p-n heterojunction structure or our ability to examine those lifetimes according to the technique outlined in previous publications [29,30]. Those publications showed significant changes in charge carrier lifetimes (orders of magnitude) as a result of changes to the  $a\text{-B}_{10}\text{C}_{2+x}\text{H}_y$  film, while the back contact remained unchanged. If the charge carrier lifetime calculated was that of the charges in the depletion region of the Schottky barrier diode, the lifetime would have remained a constant value regardless of film dopant or level of irradiation as the irradiating ion penetration depth was far short (hundreds of microns) of the Schottky barrier diode depletion region.

The technique for calculating the charge carrier lifetime was presented previously [29,30]. This lifetime technique has been performed for each irradiation period of 0, 10, 20, and 40 hours of neutron irradiation, or no neutrons above background, roughly  $2.7 \times 10^8$ ,  $5.4 \times 10^8$ ,  $1.08 \times 10^9$  neutrons/cm<sup>2</sup> above background respectively. The results are shown in Fig. 6.3 as the right hand vertical axis in **red**. The indicated charge carrier lifetime for the un-irradiated sample is 0.95  $\mu\text{s}$ , after 10 hours of irradiation this increases to 1.20  $\mu\text{s}$ , after 20 hours of irradiation this is further increased to 3.00  $\mu\text{s}$ , and after 40 hours of irradiation this trend reverses and is decreased to 1.30  $\mu\text{s}$ .

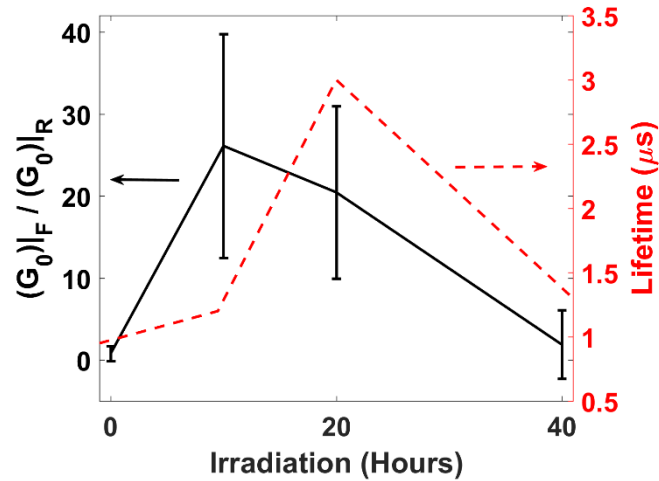


Fig. 6.3: (Left axis) The ratio of the derivative of forward bias current with respect to voltage by the derivative of reverse bias current with respect to voltage derived from  $I(V)$  data taken between 0.75 and 1.00 applied volts. The higher the ratio, the better the heterojunction diode performance (figure-of-merit). (Right axis) The effective carrier lifetime as a function of neutron irradiation as indicated by  $C_D$  modeling.

The capacitance associated with oscillations in the depletion width due to small sinusoidal perturbations is referred to as the junction capacitance ( $C_J$ ). In the case of a heterojunction device,  $C_J$  is described by [32]:

Equation 6-6

$$C_J = \left( \frac{qN_1N_2\varepsilon_1\varepsilon_2\varepsilon_0}{2(\varepsilon_1N_1 + \varepsilon_2N_2)(\varphi_{bi} - V_A)} \right)^{\frac{1}{2}}$$

where  $q$  is the elemental charge,  $\varepsilon_0$  is the permittivity of free space,  $N_1$  is the number of donor atoms/ $m^3$  in the n-type material,  $N_2$  is the number of acceptor atoms/ $m^3$  in the p-type material,  $\varepsilon_1$  is the dielectric constant of the n-type material,  $\varepsilon_2$  is the dielectric constant of the p-type material,  $\varphi_{bi}$  is the device built-in voltage, and  $V_A$  is the applied voltage. If there are no other charge oscillations, the device capacitance, independent of frequency, is equal to  $C_J$  in reverse bias (depletion conditions) [33].

Fig. 6.4 plots the Capacitance *versus* Voltage  $C(V)$  curves of a  $a\text{-}B_{10}C_{2+x}H_y/Si$  p-n heterojunction device after 0, 10, 20, and 40 hours of neutron irradiation at 100 kHz.

Though not shown here, the capacitance for all irradiation exposure times and

frequencies of 10, 100, and 1000 kHz all remain between 0.17 and 0.38 nF (i.e. very frequency independent).

In reverse bias, the device capacitance is dominated by the junction capacitance even after 40 hours of neutron irradiation (estimated fluence  $1.08 \times 10^9 \frac{\text{neutrons}}{\text{cm}^2}$ ). Because it is reverse biased and there is not an additional frequency dependent capacitive component, the minority carrier concentration near the edge of the depletion region is very small compared to that of the majority carriers, and thus can be neglected in calculating  $C_j$  [30].

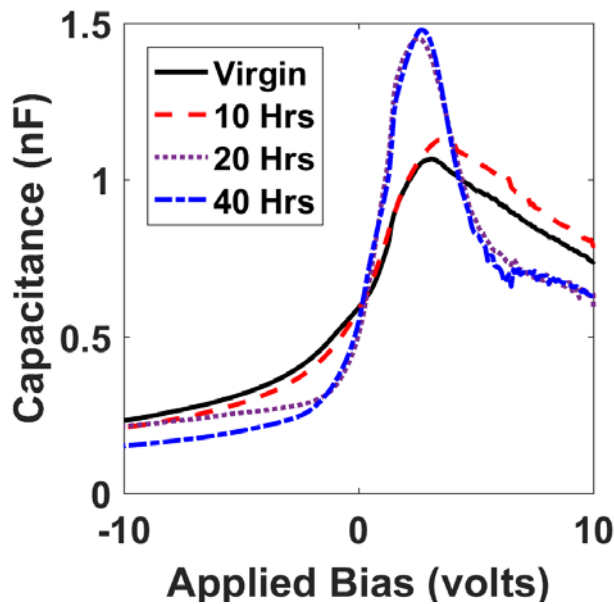


Fig. 6.4: Capacitance versus Voltage  $C(V)$  curves taken at 100 kHz of  $\alpha\text{-B}_{10}\text{C}_{2+x}\text{H}_y/\text{Si}$  p-n heterojunction device after 0, 10, 20, and 40 hours of neutron irradiation.

Due to the sinusoidal perturbation signal in forward bias, there is a significant contribution by the minority carriers to the changes in charge concentration. This contribution to the device capacitance is referred to as the diode diffusion capacitance ( $C_D$ ), and is given by the equation [23]:

Equation 6-7

$$C_D = \frac{G_0}{\omega\sqrt{2}} \left( \sqrt{1 + \omega^2\tau^2} - 1 \right)^{\frac{1}{2}}$$

where  $G_0$  is the low frequency conductance previously defined and shown as a ratio in Fig. 6.3,  $\omega$  is the angular frequency ( $2\pi f$ ), and  $\tau$  is the effective carrier lifetime.

There are many and various contributions to the capacitances, and many types of defects, but if we restrict our modeling efforts to the diffusion component of transport, Equation 6-7 can be used to model the data relative to the baseline capacitance of Fig. 6.4.

The peak capacitance shown in Fig. 6.4, for all irradiation times, is slightly shifted to the positive bias region (2.6 – 3.7 v) because of the voltage drop across the Schottky barrier contact on the back side of the Si substrate. In this experiment, there is a 0.45 eV Schottky barrier from the Si/Cr/Au Metal-to-Semiconductor (MS) interface. Remembering that Equation 6-1 means that all capacitor charging will be limited by the capacitor with the smallest charge capabilities, in this circuit this is expected to be the Schottky diode. To test this, we calculated the expected capacitance of the Si-Cr Schottky diode. The charge carrier concentration of the Si substrate was calculated from the manufacturer resistivity specifications. For 98  $\Omega \times \text{cm}$  resistivity silicon (matching our 4-point probe measurement) a carrier concentration of  $4.5 \times 10^{19} \text{ m}^{-3}$  was calculated from [34]. The widely accepted dielectric constant of Si is 11.68, and the area of the contact is  $2.4 \times 10^{-5} \text{ m}^2$ . The depletion width ( $W$ ) is calculated to be  $1.7799 \times 10^{-6} \text{ m}$  from [35]. The capacitance of a Schottky diode is given by the relation [23]:

*Equation 6-8*

$$C = \frac{\epsilon_1 \epsilon_0 A}{W}$$

Where  $\epsilon_1$  is the semiconductor dielectric constant,  $\epsilon_0$  is the permittivity of free space,  $A$  is the cross sectional area of the diode, and  $W$  is the depletion width. The calculated capacitance for the Schottky diode is then 1.39 nF, matching the peak capacitance of

our device, and showing that charging across the p-n heterojunction structure is limited by the charging capabilities of the Schottky barrier diode.

#### 6.4 Discussion

Thermal neutron irradiation of the c-Si atoms has a significant cross-section for scattering events, but not for capture or displacement events ( $m_{neutron} \ll m_{Si}$ ). As a result, the c-Si lattice structure should only be perturbed by the energetic  ${}^7\text{Li}$  (0.84 MeV) and alpha particle ( $\text{He}^+$ ) (1.47 MeV) pairs created by  ${}^{10}\text{B}$  neutron capture events, in the boron carbide layer of the heterojunction. The neutron fluence and capture probability (outlined in the experimental section) should be such that the damage within the c-Si substrate of this experiment is minimal. We anticipate that for this experiment any changes in electrical or structural characteristics should be isolated to the amorphous partially dehydrogenated semiconducting boron carbide film, not due to the large amounts of damage in the c-Si substrate observed previously.

In an effort to identify changes in the device as a function of irradiation, high resolution transmission electron microscopy (HRTEM) images and selected area electron diffraction (SAED) patterns were obtained both of the  $a\text{-}B_{10}C_{2+x}H_y/Si$  interface, and in the bulk Si far from the interface (800 nm), but still within the  ${}^7\text{Li}$  and  $\text{He}^+$  ion range. These images are shown in Fig. 6.5, with the SAED of the  $a\text{-}B_{10}C_{2+x}H_y$  film shown as the inset of Fig. 6.5(a), and the SAED of the Si shown as an inset in Fig. 6.5(b). Both the HRTEM image and the SAED of the  $a\text{-}B_{10}C_{2+x}H_y$  film show it remains amorphous. While there appears to be a narrow region (less than 1 nm) of strained Si, the interface remains abrupt. Finally, no discernable damage is apparent in either the  $a\text{-}B_{10}C_{2+x}H_y$  or the Si substrate, in either HTREM image or the SAED pattern, however point defects in Si are undetectable with this technique until

they occur in concentrations high enough that point defect agglomeration begins to occur [16]. This is in agreement with our previous findings that device improvement as a result of irradiation is not due to changes in the interface, changes in structure of the amorphous material, or changes in structure of the crystalline material. Instead, our supposition remains that the improvement is due to defect passivation of the amorphous material.

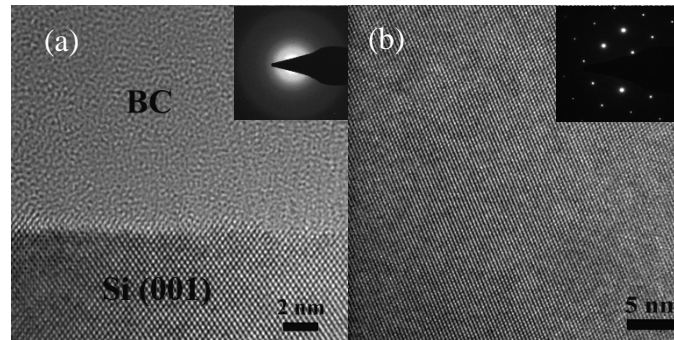


*Fig. 6.5: The HRTEM image and SAED pattern of (a) the  $a\text{-B}_{10}\text{C}_{2+x}\text{H}_y$  film – Si (001) interface after 40 hours of neutron irradiation and shows that the Si substrate remains crystalline near the interface and the  $a\text{-B}_{10}\text{C}_{2+x}\text{H}_y$  film – Si (001) junction interface remains abrupt and the  $a\text{-B}_{10}\text{C}_{2+x}\text{H}_y$  film remains amorphous. And (b) is taken 800 nm away from the interface showing that the Si remains crystalline with no point defect agglomeration as witnessed in [16].*

If defect passivation is the driving force behind device improvement, that will change the carrier concentration of the  $a\text{-B}_{10}\text{C}_{2+x}\text{H}_y$  film (toward a more intrinsic material), if some of the passivated defects had contributed to the carrier concentration. Such changes should be evident in the built-in potential of each constituent semiconducting material comprising the heterojunction structure. The device built-in potential ( $\varphi_{bi}$ ) is the sum of the built-in potential within each constituent semiconducting material (i.e. the narrow band-gap material and the wide band-gap material):

*Equation 6-9*

$$\varphi_{bi} = \varphi_{b1} + \varphi_{b2}$$

Where  $\varphi_{b1}$  is the built-in potential of the Si, and  $\varphi_{b2}$  is the built-in potential of the  $a\text{-B}_{10}\text{C}_{2+x}\text{H}_y$  film, and are given by:

Equation 6-10

$$V_{bi1} = \frac{\varepsilon_2 N_2 (\varphi_{bi} - V)}{\varepsilon_1 N_1 + \varepsilon_2 N_2}$$

$$V_{bi2} = \frac{\varepsilon_1 N_1 (\varphi_{bi} - V)}{\varepsilon_1 N_1 + \varepsilon_2 N_2}$$

Where  $\varepsilon_1 N_1$  are the dielectric constant and doping concentration of semiconductor 1 (i.e. the silicon substrate), and  $\varepsilon_2 N_2$  are the dielectric constant and doping concentration of semiconductor 2 (i.e.  $\alpha$ -B<sub>10</sub>C<sub>2+x</sub>H<sub>y</sub>), and  $\varphi_{bi}$  is the total built-in potential, or the device built-in potential. ( $\varphi_{bi}$ ), and the acceptor carrier concentration was extrapolated from the  $C(V)$  measurement at 100 kHz and is shown in Fig. 6.6.

Remembering that Fig. 6.4 demonstrates that the reverse bias capacitance is dominated by the junction capacitance component, and starting with Equation 6-6, by taking the derivative of Equation 6-6 with respect to applied voltage and solving for  $N_2$  it can be shown that:

Equation 6-11

$$N_2 = \frac{-2N_2\varepsilon_2}{A^2 q \varepsilon_1 \varepsilon_2 \varepsilon_0 N_2 \left( \frac{d(1/C^2)}{dV_a} \right) + 2\varepsilon_1}$$

Where  $\frac{d(1/C^2)}{dV_a}$  is numerically determined from the small reverse bias region of a  $1/C^2$

*versus* Voltage plot as shown in Fig. 6.6, and  $A$  is the device cross sectional area.

According to the relationships of Equation 6-11, as the slope in Fig. 6.6  $\left( \frac{d(1/C^2)}{dV_a} \right)$

increases, the carrier concentration decreases.

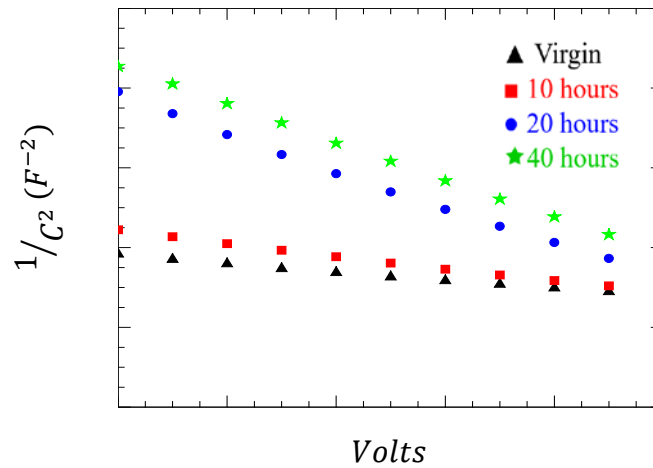


Fig. 6.6:  $1/C^2$  versus voltage relationship is plotted to allow for the extrapolation of the device built-in potential ( $V_{bi}$ ) and acceptor carrier concentration ( $N_A$ ).

While it is well understood that radiation damage significantly reduces charge carrier lifetimes in silicon [18,36], and that bulk radiation damage has a significant effect on charge carrier concentration profiles [37–43], the damage due to  ${}^7\text{Li}/\text{He}^+$  pairs following thermal neutron capture are expected to be well below the thresholds for such results. Calculations above (as outlined by Hoglund *et al.* [28]) estimated approximately  $3.2 \times 10^4$   ${}^7\text{Li}/\text{He}^+$  pairs are generated per hour of irradiation. It has been reported that  $10^{14}$  particles/cm<sup>2</sup> ( $\sim 1$  MeV neutrons) do not cause fundamental problems in Si based radiation detectors [37], however, Gill *et al.* showed that there are changes within the bulk Si. After a sufficient particle fluence, the bulk n-type silicon, is observed to type invert and behave as p-type material after a flux of  $\sim 2 \times 10^{13}$  particles/cm<sup>2</sup> ( $\sim 1$  MeV neutrons). Ionized particles such as the  ${}^7\text{Li}/\text{He}^+$  pairs will also effect the effective doping concentration of the bulk silicon, but it has been reported that fluences greater than  $10^{10}$  alpha particles are required to impact the “diode blocking voltage” (also known as the break down voltage) [36], a good measure of changes in the electrical characteristic of the device. These reported changes in the silicon are many orders of magnitude greater than the radiation exposure our samples experienced after 40 hours of irradiation. It is expected that

there will be some local changes in Si carrier concentration, due to ion tracks, but that the carrier concentration of the bulk silicon substrate ( $N_1$ ) may be treated as a constant.

Using the assumption that the silicon carrier concentration is constant, and Equation 6-11, the carrier concentration of the  $a\text{-}B_{10}C_{2+x}H_y$  film decreases with neutron irradiation, as shown in Fig. 6.8. The dielectric response and device value  $\epsilon_1=11.68$ ,  $\epsilon_2=3.5$  (see Appendix C for modeling and formulation),  $A=5.1\times 10^{-5} \text{ m}^2$ ,  $N_1=4.5\times 10^{19} \text{ m}^{-3}$  (as calculated by [34]) were used to estimate the carrier concentration (Fig. 6.7). Please note that the low frequency (d.c.) relative dielectric constant ( $\epsilon_2$ ) of  $a\text{-}B_{10}C_{2+x}H_y$  is unknown, and we are not asserting in this manuscript that  $\epsilon_2 = 3.5$  for this material, but represents a best guess from ellipsometric measurement and modeling. While quantitatively, any deviation in  $\epsilon_2$  will change  $N_2$ , qualitatively, the trends will remain the same. In addition to the calculation outlined above, the capacitance *versus* voltage  $C(V)$  data of Fig. 6.6 was experimentally fit by Equation 6-6 allowing the carrier concentration and built-in voltage, to be fitting parameters. We found excellent agreement between the two methods: numeric calculation of  $N_2$  and experimental fitting of  $N_2$ . The results are shown below in Fig. 6.7. It was found that for the virgin sample, the carrier concentration was  $1.50 \times 10^{20} \text{ 1/m}^3$ . That drops slightly after 10 hours of irradiation to  $7.10 \times 10^{19} \text{ 1/m}^3$ . There is a further drop to  $1.68 \times 10^{19} \text{ 1/m}^3$  after 20 hours of irradiation. This is followed by another slight drop to  $1.25 \times 10^{19} \text{ 1/m}^3$  after 40 hours of irradiation. As pointed out in prior work [16] and reinforced in Fig. 6.6 (the increase in slope indicating a decrease in carrier concentration), the amorphous material seems the most likely candidate for changes as a result of initial irradiation through defect passivation.

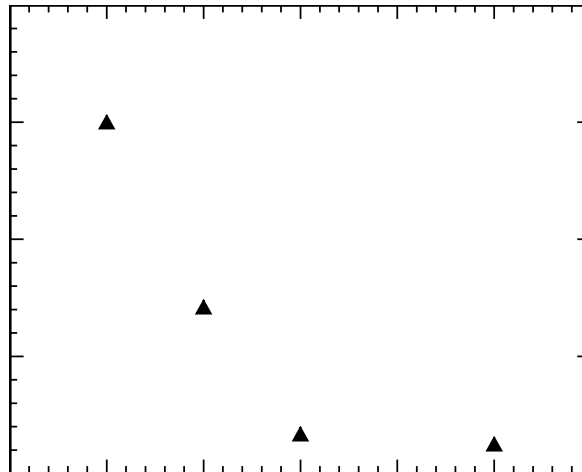


Fig. 6.7:  $a-B_{10}C_{2+x}H_y$  film carrier concentration as a function of neutron exposure as calculated by Equation 6-11 and fitted to the data in Fig. 6.6.

If there is indeed a decrease in the charge carrier concentration of the  $a-B_{10}C_{2+x}H_y$  film as shown in Fig. 6.7, this will result in a shift of the Fermi Energy Level ( $E_F$ ) away from the valence band ( $E_V$ ) as the material becomes more intrinsic in nature. Because the conduction band and valence band discontinuities ( $\Delta E_C$  and  $\Delta E_V$ ) are not a function of carrier concentration, but are resultant from the interface of two semiconductor materials with differing  $E_g$  values, the band re-alignment requires a change in the built-in potential within each semiconductor. Fig. 6.8 shows the band diagram of a p-n heterojunction with the n-type narrow band-gap material on the left (Si substrate), and the p-type wide band-gap material on the right ( $a-B_{10}C_{2+x}H_y$  film). Equations 6-9 & 6-10 show that the barrier to charge translation of the constituent materials are dependent on the relative di-electric constant and carrier concentration of the other constituent material (i.e.  $\phi_{b1}$  is dependent on  $\epsilon_2 N_2$ ).

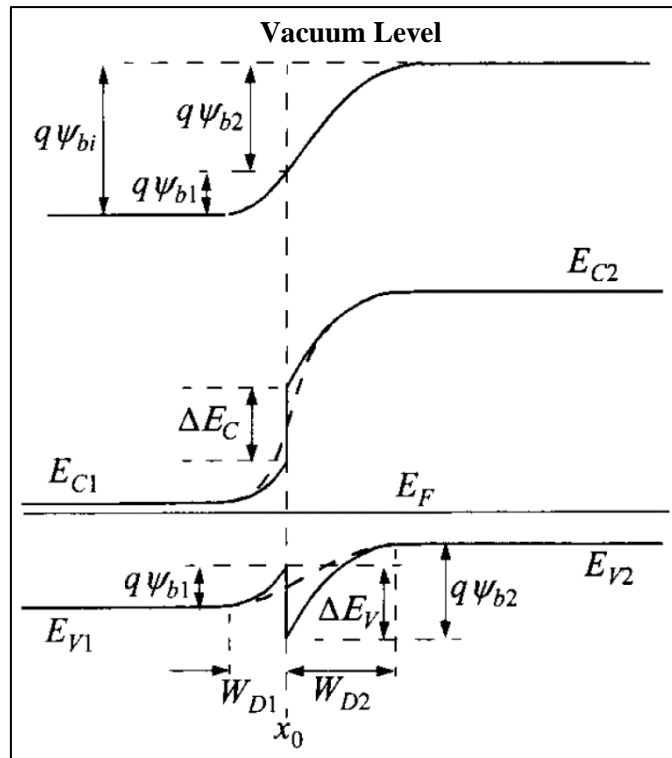


Fig. 6.8: The thermal equilibrium energy-band diagram of two semiconductors of opposite type and different energy band gaps ( $E_g$ ), i.e. a p-n heterojunction, after [44].  $\phi_{b1}$  and  $\phi_{b2}$  represent the built-in potential in semiconductor 1 and 2 respectively.

As shown in Fig. 6.8, as  $E_F$  of the p-type material shifts toward mid bandgap,  $\phi_{b1}$  and  $\phi_{b2}$  must change. The relation below shows that  $\phi_{b2}$  must be increased and  $\phi_{b1}$  must be decreased as  $N_2$  is decreased.

Equation 6-12

$$\frac{\phi_{b1}}{\phi_{b2}} = \frac{\epsilon_1 N_1}{\epsilon_2 N_2}$$

Combining the data of Fig. 6.7 with Equations 6-9 & 6-10 we can plot the device built-in potential as well as the barriers to charge translation within each constituent material. This is shown in Fig. 6.9.

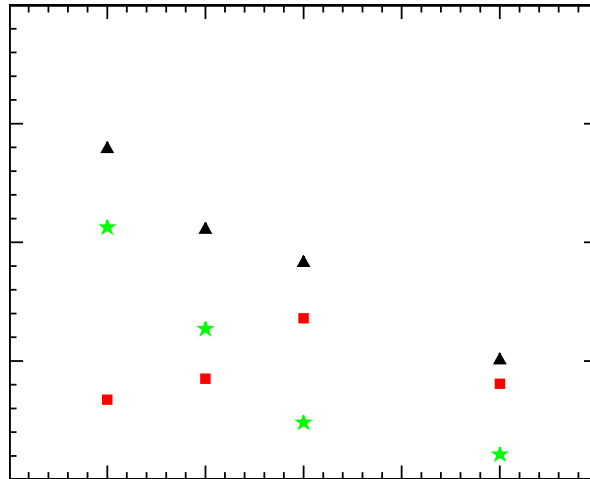


Fig. 6.9: The extrapolated device built-in potential of the p-n heterojunction as a function of neutron exposure taken from Fig. 6.6 and shown as black triangles ( $\blacktriangle$ ). The calculated barrier to charge translation of the  $a\text{-}B_{10}C_{2+x}H_y$  and Si substrate are shown as red squares ( $\blacksquare$ ), and green triangles ( $\blackstar$ ) respectively.

The trends of Fig. 6.9 matches expectations. A reduction in the charge carrier concentration means less band bending and a smaller device built-in potential. This would also account for the dramatic increase in the forward bias diode current of Fig. 6.2. As the built-in potential within the  $a\text{-}B_{10}C_{2+x}H_y$  film increases (from 0 to 20 hours of irradiation), so does the charge carrier lifetime as seen in Figs. 6.9 and 6.3 respectively. From 20 to 40 hours of irradiation, even though the majority of the barrier to charge translation is located within the  $a\text{-}B_{10}C_{2+x}H_y$  film, the overall device built-in potential continues to drop, dictating a drop in the built-in potential of the  $a\text{-}B_{10}C_{2+x}H_y$  film, and again the charge carrier lifetime in Fig. 6.3 follows that trend.

## 6.5 Conclusions

In conclusion, amorphous partially dehydrogenated semiconducting boron carbide was synthesized via PECVD on n-type single crystal silicon. A Cr-Si Schottky barrier was created on the backside of the silicon to create a series capacitance limiting the charge buildup on the p-n heterojunction. By placing a

Schottky barrier on the back side of the Si substrate, and limiting the charge build up (dominated by the smaller capacitance) at the p-n metallurgical interface (the physical interface between the  $a\text{-}B_{10}C_{2+x}H_y$  film and Si substrate – not to be confused with the metal contact) the electric field of the interface is limited, and the depletion width is decreased. This allows for the probing of the p-n heterojunction device that would otherwise have the properties of a narrow-base device (a device with a quasi-neutral region on the order of a charge carrier diffusion length or smaller) or a device that suffers from punch-through (a device with no quasi-neutral region). This device was irradiated with thermal neutrons having energies around 0.02 eV. The device electrical properties were measured and characterized at several irradiation intervals. This research provides evidence that the electrical properties of amorphous partially dehydrogenated semiconducting boron carbide on silicon p-n heterojunction diodes initially improve with neutron irradiation, contrary to nearly all traditional electronic devices. The cause for the device improvement is most likely a result of a reduction in the carrier concentration within the  $a\text{-}B_{10}C_{2+x}H_y$  film, which has an effect on the barrier to charge translation in the Si substrate. The reduction in barrier height allows for a greater number of charges to contribute to the current density as shown in Fig. 6.2 and quantified in Fig. 6.3. Further, there is a direct correlation between the trends of the built-in potential of the  $a\text{-}B_{10}C_{2+x}H_y$  film and the charge carrier lifetime.

This research indicates that some disorder within the amorphous semiconductor film (in the form of defects) allows for healing with initial irradiation. This increases the operational lifetime of the device. Perhaps more importantly, this research provides further evidence that future devices should be based on field effect devices. For a truly radiation hard device, it may not be sufficient to remove the crystalline silicon component and replace it with an n-type amorphous film.

## 6.6 References

- [1] A.N. Caruso, The physics of solid-state neutron detector materials and geometries, *J. Phys. Condens. Matter.* 22 (2010) 443201. doi:10.1088/0953-8984/22/44/443201.
- [2] A.N. Caruso, R.B. Billa, S. Balaz, J.I. Brand, P.A. Dowben, The heteroisomeric diode, *J. Phys. Condens. Matter.* 16 (2004) L139–L146. doi:10.1088/0953-8984/16/10/L04.
- [3] B.W. Robertson, S. Adenwalla, A. Harken, P. Welsch, J.I. Brand, P. Dowben, J.P. Claassen, A class of boron-rich solid-state neutron detectors, *Appl. Phys. Lett.* 80 (2002) 1344–3646.
- [4] S. Adenwalla, R. Billa, J.I. Brand, E. Day, M.J. Diaz, A. Harken, A. McMullen-Gunn, R. Padmanabhan, B.W. Robertson, Semiconducting boron-rich neutron detectors, in: *Proc SPIE*, 2004: pp. 70–74. doi:10.1117/12.506646.
- [5] B.W. Robertson, S. Adenwalla, A. Harken, P. Welsch, J.I. Brand, J.P. Claassen, N.M. Boag, P.A. Dowben, Semiconducting boron-rich neutron detectors, in: *Proc SPIE*, 2002: pp. 226–233. doi:10.1117/12.453923.
- [6] K. Osberg, N. Schemm, S. Balkir, J.I. Brand, S. Hallbeck, P.A. Dowben, A hand-held neutron detection sensor system, in: *Peter Dowben Publ.*, 2006: p. 4 pp. doi:10.1109/ISCAS.2006.1692801.
- [7] K. Osberg, N. Schemm, S. Balkir, J.I. Brand, M.S. Hallbeck, P.A. Dowben, M.W. Hoffman, A Handheld Neutron-Detection Sensor System Utilizing a New Class of Boron Carbide Diode, *IEEE Sens. J.* 6 (2006) 1531–1538. doi:10.1109/JSEN.2006.883905.

- [8] A.N. Caruso, P.A. Dowben, S. Balkir, N. Schemm, K. Osberg, R.W. Fairchild, O.B. Flores, S. Balaz, A.D. Harken, B.W. Robertson, J.I. Brand, The all boron carbide diode neutron detector: Comparison with theory, *Mater. Sci. Eng. B.* 135 (2006) 129–133. doi:10.1016/j.mseb.2006.08.049.
- [9] E. Day, M.J. Diaz, S. Adenwalla, Effect of bias on neutron detection in thin semiconducting boron carbide films, *J. Phys. Appl. Phys.* 39 (2006) 2920. doi:10.1088/0022-3727/39/14/007.
- [10] N. Hong, J. Mullins, K. Foreman, S. Adenwalla, Boron carbide based solid state neutron detectors: the effects of bias and time constant on detection efficiency, *J. Phys. Appl. Phys.* 43 (2010) 275101. doi:10.1088/0022-3727/43/27/275101.
- [11] N. Hong, L. Crow, S. Adenwalla, Time-of-flight neutron detection using PECVD grown boron carbide diode detector, *Nucl. Instrum. Methods Phys. Res. Sect. Accel. Spectrometers Detect. Assoc. Equip.* 708 (2013) 19–23. doi:10.1016/j.nima.2012.12.105.
- [12] E. Echeverría, R. James, U. Chilawal, F.L. Pasquale, J.A.C. Santana, R. Gapfizi, J.-D. Tae, M.S. Driver, A. Enders, J.A. Kelber, P.A. Dowben, Novel semiconducting boron carbide/pyridine polymers for neutron detection at zero bias, *Appl. Phys. A.* 118 (2014) 113–118. doi:10.1007/s00339-014-8778-4.
- [13] Ruqiang Bao, Zijie Yan, D.B. Chrisey, Charge carrier lifetime in boron carbide thin films, *Appl. Phys. Lett.* 98 (2011) 192106. doi:10.1063/1.3589816.
- [14] E. Echeverría, R. James, F.L. Pasquale, J.A. Colón Santana, M.S. Driver, A. Enders, J.A. Kelber, P.A. Dowben, Neutron Detection Signatures at Zero Bias in Novel Semiconducting Boron Carbide/Pyridine Polymers, in: *Symp. DDWW – Mater. Radiat. Eff. Adv. Nucl. Technol.*, 2015. doi:10.1557/opl.2015.352.

- [15] H.E. Robson, Vapor pressure and thermodynamic properties of boron carbide, Ph.D., University of Kansas, 1959.
- [16] G. Peterson, Q. Su, Y. Wang, P.A. Dowben, M. Nastasi, Improved p–n heterojunction device performance induced by irradiation in amorphous boron carbide films, *Mater. Sci. Eng. B.* 202 (2015) 25–30.  
doi:10.1016/j.mseb.2015.09.002.
- [17] G.G. Peterson, Y. Wang, N.J. Ianno, M. Nastasi, Modeling Changes in Measured Conductance of Semiconductors Under Irradiation, (n.d.).
- [18] D. Emin, Unusual properties of icosahedral boron-rich solids, *J. Solid State Chem.* 179 (2006) 2791–2798. doi:10.1016/j.jssc.2006.01.014.
- [19] M. Carrard, D. Emin, L. Zuppiroli, Defect clustering and self-healing of electron-irradiated boron-rich solids, *Phys. Rev. B.* 51 (1995) 11270–11274.  
doi:10.1103/PhysRevB.51.11270.
- [20] J.E. Bevins, K.R. Dahl, J.W. McClory, J.C. Petrosky, A.N. Caruso, Bulk Radiation Damage Effects of a p-type B<sub>5</sub>C:H<sub>x</sub> Thin Film on n-Si Heterojunction Diode, *J. Radiat. Eff. Res. Eng.* 30 (2012) 33–38.
- [21] T. Stoto, N. Housseau, L. Zuppiroli, B. Kryger, Swelling and microcracking of boron carbide subjected to fast neutron irradiations, *J. Appl. Phys.* 68 (1990) 3198–3206. doi:10.1063/1.346370.
- [22] D. Simeone, C. Mallet, P. Dubuisson, G. Baldinozzi, C. Gervais, J. Maquet, Study of boron carbide evolution under neutron irradiation by Raman spectroscopy, *J. Nucl. Mater.* 277 (2000) 1–10. doi:10.1016/S0022-3115(99)00149-X.
- [23] R.F. Pierret, *Semiconductor Device Fundamentals*, 2nd edition, Addison Wesley, Reading, Mass, 1996.

- [24] N. Hong, *An Exploration of Neutron Detection in Semiconducting Boron Carbide*, University of Nebraska - Lincoln, 2012.  
<http://digitalcommons.unl.edu/physicsdiss/20>.
- [25] Thermo Fisher, (n.d.). <https://www.thermofisher.com/us/en/home.html> (accessed February 22, 2017).
- [26] J.P. Biersack, L.G. Hagmark, A Monte Carlo computer program for the transport of energetic ions in amorphous targets, *Nucl. Instrum. Methods.* 174 (1980) 257–269. doi:10.1016/0029-554X(80)90440-1.
- [27] M. Nastasi, J.W. Mayer, *Ion Implantation and Synthesis of Materials*, Springer, 2006.  
<http://www.springer.com/physics/particle+and+nuclear+physics/book/978-3-540-23674-0> (accessed February 5, 2015).
- [28] C. Höglund, K. Zeitelhack, P. Kudejova, J. Jensen, G. Greczynski, J. Lu, L. Hultman, J. Birch, R. Hall-Wilton, Stability of 10B4C thin films under neutron radiation, *Radiat. Phys. Chem.* 113 (2015) 14–19.  
doi:10.1016/j.radphyschem.2015.04.006.
- [29] G.G. Peterson, E. Echeverria, B. Dong, J.P. Silva, E.R. Wilson, J.A. Kelber, M. Nastasi, P.A. Dowben, Increased drift carrier lifetime in semiconducting boron carbides deposited by plasma enhanced chemical vapor deposition from carboranes and benzene, *J. Vac. Sci. Technol. Vac. Surf. Films.* 35 (2016) 03E101. doi:10.1116/1.4973338.

- [30] E. Echeverria, B. Dong, G. Peterson, J.P. Silva, E.R. Wilson, M.S. Driver, Y.-S. Jun, G.D. Stucky, S. Knight, T. Hofmann, Z.-K. Han, N. Shao, Y. Gao, W.-N. Mei, M. Nastasi, P.A. Dowben, J.A. Kelber, Semiconducting boron carbides with better charge extraction through the addition of pyridine moieties, *J. Phys. Appl. Phys.* 49 (2016) 355302–355312. doi:10.1088/0022-3727/49/35/355302.
- [31] E. Echeverría, B. Dong, A. Liu, E.R. Wilson, G. Peterson, M. Nastasi, P.A. Dowben, J.A. Kelber, Strong binding at the gold (Au) boron carbide interface, *Surf. Coat. Technol.* (2016). doi:10.1016/j.surfcoat.2016.08.081.
- [32] R.L. Anderson, Experiments on Ge-GaAs heterojunctions, *Solid-State Electron.* 5 (1962) 341–351. doi:10.1016/0038-1101(62)90115-6.
- [33] S.S. Li, p-n Junction Diodes, in: S.S. Li (Ed.), *Semicond. Phys. Electron.*, Springer New York, 2006: pp. 334–380.  
[http://link.springer.com/chapter/10.1007/0-387-37766-2\\_11](http://link.springer.com/chapter/10.1007/0-387-37766-2_11) (accessed October 16, 2015).
- [34] Resistivity & Mobility Calculator for Various Doping Concentrations in Silicon, (n.d.). <http://www.cleanroom.byu.edu/ResistivityCal.phtml> (accessed February 28, 2017).
- [35] Metal-Semiconductor Ohmic & Schottky Contacts / Barrier Height and Depletion Width Calculators, (n.d.). <http://www.cleanroom.byu.edu/ohmic-schottky.phtml> (accessed April 13, 2016).
- [36] P. Hazdra, V. Komarnitsky, Local lifetime control in silicon power diode by ion irradiation: introduction and stability of shallow donors, *IET Circuits Devices Syst.* 1 (2007) 321. doi:10.1049/iet-cds:20070013.

- [37] K. Gill, G. Hall, B. MacEvoy, Bulk damage effects in irradiated silicon detectors due to clustered divacancies, *J. Appl. Phys.* 82 (1997) 126–136.  
doi:10.1063/1.365790.
- [38] K. Gill, G. Hall, S. Roe, S. Sotthibandhu, R. Wheadon, P. Giubellino, L. Ramello, Radiation damage by neutrons and protons to silicon detectors, *Nucl. Instrum. Methods Phys. Res. Sect. Accel. Spectrometers Detect. Assoc. Equip.* 322 (1992) 177–188. doi:10.1016/0168-9002(92)90027-2.
- [39] E. Fretwurst, H. Feick, M. Glaser, C. Gößling, E.H.M. Jeijne, A. Hess, Reverse annealing of the effective impurity concentration and long-term operational scenario for silicon detectors in future collider experiments, *Nucl. Instrum. Methods Phys. Res. Sect. Accel. Spectrometers Detect. Assoc. Equip.* (1994).  
doi:10.1016/0168-9002(94)91417-6.
- [40] D. Pitzl, N. Cartiglia, B. Hubbard, D. Hutchinson, J. Leslie, K. O’Shaughnessy, W. Rowe, H.F.-W. Sadrozinski, A. Seiden, E. Spencer, H.J. Ziock, P. Ferguson, K. Holzscheiter, W.F. Sommer, Type inversion in silicon detectors, *Nucl. Instrum. Methods Phys. Res. Sect. Accel. Spectrometers Detect. Assoc. Equip.* 311 (1992) 98–104. doi:10.1016/0168-9002(92)90854-W.
- [41] P.A. Aarnio, M. Huhtinen, M. Pimiä, K. Kaita, M. Laakso, A. Numminen, P. Ryytty, Damage observed in silicon diodes after low energy pion irradiation, *Nucl. Instrum. Methods Phys. Res. Sect. Accel. Spectrometers Detect. Assoc. Equip.* 360 (1995) 521–531. doi:10.1016/0168-9002(95)00008-9.

- [42] S.J. Bates, C. Furetta, M. Glaser, F. Lemeilleur, E. León-Florián, C. Gößling, B. Kaiser, A. Rolf, R. Wunstorf, H. Feick, E. Fretwurst, G. Lindström, M. Moll, G. Taylor, A. Chilingarov, Pion-induced damage in silicon detectors, *Nucl. Instrum. Methods Phys. Res. Sect. Accel. Spectrometers Detect. Assoc. Equip.* 379 (1996) 116–123. doi:10.1016/0168-9002(96)00538-4.
- [43] K. Riechmann, K.T. Knöpfle, V.M. Pugatch, Pion and proton induced radiation damage to silicon detectors, *Nucl. Instrum. Methods Phys. Res. Sect. Accel. Spectrometers Detect. Assoc. Equip.* 377 (1996) 276–283. doi:10.1016/0168-9002(95)01408-X.
- [44] S.M. Sze, K.K. Ng, *Physics of semiconductor devices*, 3rd ed., John Wiley & Sons, Inc., 2006. <http://dx.doi.org/10.1002/9780470068328.ch2>.

## Chapter 7 Summary and Conclusions

The projects involved in this dissertation focus on the transport properties of semiconducting partially dehydrogenated amorphous boron carbide synthesized via plasma enhanced chemical vapor deposition (PECVD) on silicon substrates forming p-n heterojunction diodes with irradiation. It has been demonstrated through current *versus* voltage measurements that such p-n heterojunctions exhibit an improvement in their electrical characteristics with moderate amounts of He<sup>+</sup> irradiation. While it is believed that such improvements are due to bond defect passivation leading to changes in the effective carrier concentrations, and resulting in band realignment, this work cannot definitively prove that. It does however provide a body of evidence that the durability of the device is limited by the fragility of the silicon substrate to the irradiation. Device degradation is not associated with any interaction of the irradiating ions with the  $a\text{-}B_{10}C_{2+x}H_y$  film in these studies.

Drift carrier lifetime was examined with and without the inclusion of linker molecules such as benzene and pyridine. It was found that the benzene doping of the p-type semiconducting partially dehydrogenated boron carbide (ortho-carborane) increases the drift carrier lifetime by 2 orders of magnitude (7043 % increase), while the benzene doping of the n-type semiconducting partially dehydrogenated boron carbide (meta-carborane) increases the drift carrier lifetime 6 fold (500 % increase). The addition of pyridine to the p-type (PECVD) semiconducting boron carbide (ortho-carborane) increases the drift carrier lifetime by an order of magnitude (900 % increase).

A model was presented for calculating conductance as a function of frequency for semiconductors under irradiation. This model was then used to interpret measured

data and infer physical and chemical changes in the device. For low doses of irradiation, there was a change in a resistive component of the model. This was most likely due to band realignment of the  $a\text{-}B_{10}C_{2+x}H_y/Si$  heterojunction as the irradiated silicon type-inverts creating a p-p<sup>+</sup> heterojunction and reducing the barrier height. Simultaneously, the crystalline Si substrate is being damaged. Point defects are decreasing the average carrier relaxation time, and dopants are being de-activated, resulting in an increase in the resistivity of the Si. For moderate doses of irradiation, it is believed that the electronic energy deposition from the irradiating ions may be perturbing the atoms within the  $a\text{-}B_{10}C_{2+x}H_y$  film allowing for the elimination of defects, and decreasing the hole concentration ( $N_A$ ). Even though the  $a\text{-}B_{10}C_{2+x}H_y$  film is fully depleted of charge carriers, changes to the defect concentration (i.e. concentration of generation/recombination centers), and hole concentration ( $N_A$ ) will change the Fermi energy ( $E_F$ ) location within the HOMO-LUMO gap. This in turn causes band re-alignment, and would change the energy barrier at the  $a\text{-}B_{10}C_{2+x}H_y/Si$  junction. Therefore, if the  $a\text{-}B_{10}C_{2+x}H_y$  film has been altered to have less recombination/generation centers and/or smaller  $N_A$  the  $a\text{-}B_{10}C_{2+x}H_y/Si$  junction resistance will increase.

Lastly, this research demonstrates that similar to ions, neutron irradiation also causes an initial increase in the device electrical performance. The cause for the device improvement is most likely a result of a reduction in the carrier concentration within the  $a\text{-}B_{10}C_{2+x}H_y$  film causing a band re-alignment between the  $a\text{-}B_{10}C_{2+x}H_y$  and silicon. The band re-alignment causes a reduction in the charge carrier barrier-height as it relates to the built-in potential of the silicon. The reduction in barrier height allows for a greater number of charges to contribute to the current density as shown in Fig. 6.2 and quantified in Fig. 6.3. Further, there is a direct correlation

between the trends of the built-in potential of the  $a\text{-}B_{10}C_{2+x}H_y$  film and the charge carrier lifetime. As the electric field in that material strengthens, charge separation efficiency is increased, and the lifetime increases. When the electric field is then reduced, so too is charge separation efficiency, and the lifetime is decreased.

This research indicates that some disorder within the amorphous semiconductor film (in the form of defects) allows for healing with initial irradiation. This increases the operational lifetime of the device. Perhaps more importantly, this research provides further evidence that future devices should be based on field effect devices. For a truly radiation hard device, it may not be sufficient to remove the crystalline silicon component and replace it with an n-type amorphous film. The changes in charge carrier concentration of the p-type material with irradiation could still result in band re-alignment within any p-n junction based device resulting in reduced charge collection efficiency.

In conclusion, one of the main challenges in this research has been the fact that we have been working with and studying a device that suffers from punch through, a device that does not have a quasi-neutral region in the p-type material. As a result, the governing equations that are typically available for modeling and analysis are not valid, and do not apply. Isolating the  $a\text{-}B_{10}C_{2+x}H_y$  film, or growing a sufficiently thick film with known ohmic device contacts must be the next step in the research. Uncoupling and examining the single component of a complex system will allow for the definitive results of transport properties in amorphous boron carbide films. Only then will we truly know the potential of how efficient such devices will be at detecting neutrons. And, only after removing the crystalline substrate, and replacing it with an n-type  $a\text{-}B_{10}C_{2+x}H_y$  layer will we determine the amount of irradiation such a device is capable of operating in before degradation sets in.

## 7.1 Appendix A

Recognizing that the complex impedance of a resistor and capacitor in parallel is

Equation 7-1

$$Z_{R1C1} = \frac{R1(j\omega C1)^{-1}}{R1 + (j\omega C1)^{-1}}$$

The equivalent complex impedance of the circuit in Fig. 5.1 is

Equation 7-2

$$Z_{eq} = -\frac{R1 j}{C1 \omega \left(R1 - \frac{j}{C1 \omega}\right)} - \frac{R2 j}{C2 \omega \left(R2 - \frac{j}{C2 \omega}\right)} + R3$$

The complex admittance ( $Y$ ) is the reciprocal of the complex impedance

Equation 7-3

$$Y = \frac{1}{Z_{eq}} = \left( \frac{-1}{\frac{R1 j}{C1 R1 \omega - j} + \frac{R2 j}{C2 R2 \omega - j} - R3} \right)$$

The conductance of a device is the real part of the complex admittance. To obtain the real component of  $Y$ , normalize the equation

Equation 7-4

$$Y = -(C1 R1 \omega - j)(C2 R2 \omega - j) / [(R1 + R2 + R3 + (C2 R2 R3 \omega j) + (C2 R1 R2 \omega j) - (C1 C2 R1 R2 R3 \omega^2) + (C1 R1 R2 \omega j) + (C1 R1 R3 \omega j)]$$

Multiply by the complex conjugate

Equation 7-5

$$\begin{aligned} & Y \\ &= -\frac{(C1 C2 R1 R2 \omega^2 - 1)\sigma_3}{\sigma_1} + \frac{(C1 R1 \omega + C2 R2 \omega)\sigma_2}{\sigma_1} \\ &+ \left( \frac{(C1 R1 \omega + C2 R2 \omega)\sigma_3}{\sigma_1} + \frac{(C1 C2 R1 R2 \omega^2 - 1)\sigma_2}{\sigma_1} \right) j \end{aligned}$$

where

$$\sigma_1 = \sigma_2^2 + \sigma_3^2$$

$$\sigma_2 = C1 R1 R3 \omega + C2 R2 R3 \omega + C1 R1 R2 \omega + R1 R2 C2 \omega$$

$$\sigma_3 = R1 + R2 + R3 - C1 R1 C2 R2 R3 \omega^2$$

Taking the real part of Equation 7-5 gives the equation modeling the measured conductance

Equation 7-6

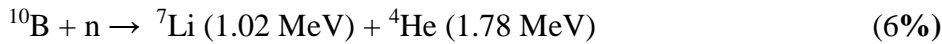
$$G_m = \frac{\omega^2((C1 R1 R2 + C2 R1 R2)(C1 R1 + C2 R2) + R3(C1 R1 + C2 R2)^2)}{\sigma_4} - \frac{(C1 C2 R1 R2 \omega^2 - 1)(-C1 C2 R1 R2 R3 \omega^2 + R1 + R2 + R3)}{\sigma_4}$$

where

$$\sigma_4 = (C1 R1 R3 \omega + C2 R2 R3 \omega + C1 R1 R2 \omega + C2 R1 R2 \omega)^2 + (-C1 C2 R1 R2 R3 \omega^2 + R1 + R2 + R3)^2$$

## 7.2 Appendix B

When a  $^{10}\text{B}$  atom captures a neutron, a  $^{11}\text{B}$  compound nucleus forms which fragments into  $^7\text{Li}$  and an alpha particle with large translational energy, and 94% of the time, gamma radiation. This is represented below:



## 7.3 Appendix C

The value of the  $a\text{-}B_{10}C_{2+x}H_y$  dielectric constant ( $\varepsilon_2$ ) is modeled through variable angle spectroscopic ellipsometry measurements using a Cody-Lorentz Model [1] and converting the  $a\text{-}B_{10}C_{2+x}H_y$  pseudo optical layer constants  $\varepsilon_1$  (volume polarization) and  $\varepsilon_2$  (volume absorption) [2] to the complex dielectric function [3]:

Equation 7-7

$$\varepsilon_1(\omega) = 1 + \frac{2}{\pi} P \int_0^\infty \frac{\omega' \varepsilon_2(\omega')}{\omega'^2 - \omega^2} d\omega'$$

Equation 7-8

$$\varepsilon_2(\omega) = -\frac{2\omega}{\pi} P \int_0^\infty \frac{\varepsilon_1(\omega') - 1}{\omega'^2 - \omega^2} d\omega'$$

Equation 7-9

$$P = \int_0^\infty d\omega' = \lim_{\delta \rightarrow 0} \left( \int_0^{\omega-\delta} d\omega' \int_{\omega+\delta}^\infty d\omega' \right)$$

Where  $P$  is “principal part of the integral”,  $\omega = 2\pi f$ , and  $\omega'$  is the complex angular frequency. Equations 7-7 & 7-8 show that the integral of  $\varepsilon_2$  is tied to the shape and magnitude of  $\varepsilon_1$ . The complex dielectric function as a function of wavelength ( $\varepsilon(\omega)$ ) is then:

*Equation 7-10*

$$\varepsilon(\omega) = \varepsilon_1(\omega) + i\varepsilon_2(\omega)$$

Fig. 7.1 plots  $\varepsilon(\omega)$  versus wavelength energy (eV) of a  $a\text{-}B_{10}C_{2+x}H_y/Si$  p-n heterojunction structure. Fig. 7.1 shows that probing wavelengths less than 2.0 eV are dominated by volume polarization effects such as atomic polarization (i.e. NaCl ionic bonding), electronic polarization (i.e. depletion region electric field), and/or dipole moments. Only for probing wavelength energies greater than 2.0 eV do absorption effects begin to contribute to the complex dielectric function as Urbach tail excitation occurs. The relative dielectric constant is taken as the value of the complex dielectric function when the incident wavelength energy approaches zero. This is shown in Fig. 7.1 to be 3.5, and is the value utilized for the calculations of charge carrier concentration using Equation 6-11 and plotted in Fig. 6.7.

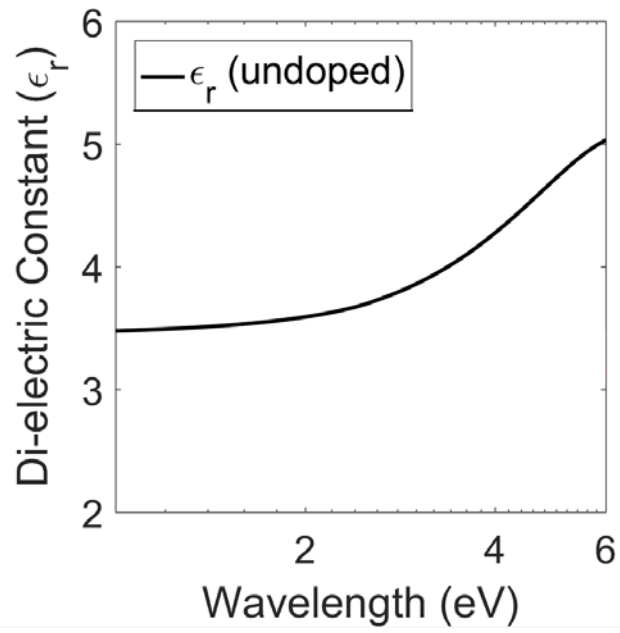


Fig. 7.1: Semi-log plot of the relative dielectric function versus wavelength. A semiconducting materials relative dielectric constant is taken as the value when the incident wavelength energy approaches zero. For  $\alpha\text{-B}_{10}\text{C}_{2+x}\text{H}_y$  the value approaches 3.5.

## 7.4 References

- [1] A.S. Ferlauto, G.M. Ferreira, J.M. Pearce, C.R. Wronski, R.W. Collins,  
Analytical model for the optical functions of amorphous semiconductors from  
the near-infrared to ultraviolet: Applications in thin film photovoltaics, *J. Appl.  
Phys.* 92 (2002) 2424–2436.
- [2] CompleteEASE Data Analysis Manual, (2011). [www.jawoollam.com](http://www.jawoollam.com).
- [3] H. Fujiwara, *Spectroscopic Ellipsometry: Principles and Applications*, John  
Wiley & Sons, Ltd, Tokyo, Japan, 2007.  
<http://onlinelibrary.wiley.com/doi/10.1002/9780470060193.fmatter/summary>.